ABSTRACT

Title of Dissertation:	MULTISCALE MEASUREMENTS OF ELECTRICAL & MECHANICAL CELLULAR DYNAMICS
	Phillip Alvarez, Doctor of Philosophy, 2023
Dissertation directed by:	Wolfgang Losert, Professor, Institute for Physical Science and Technology

This dissertation focuses on the study and measurement of coupled electrical and mechanical responses in mammalian cells, tissues, and organs. Cellular biophysics often studies forces and their impact on biochemical pathways. These forces can be electrical, resulting in neuronal action potentials or cardiac cell contractions, or mechanical, driving e.g., a cell's ability to recognize physical probing or surface texture. These forces and their responses, though, are frequently coupled through interlinked cellular mechanisms which result in emergent responses that take both electrical and mechanical signals into account. One challenge in capturing these emergent responses is that they occur on multiple scales, from the intracellular scale to the organ scale, limiting the ability of commercial microscopes to image these responses simultaneously. In this work I use surface texture, optical imaging, and multiscale-capable image analysis algorithms across these scales to elicit and measure electrical and mechanical responses. To

image emergent responses from electrical and mechanical coupling, I developed two custom microscopes that can image at multiple length scales and timescales simultaneously. The Multiscale Microscope can capture slow intracellular mechanical dynamics concurrently with fast tissue scale electrical dynamics, while the BEAMM microscope links fast tissue scale electrical dynamics with both intracellular mechanical dynamics and slower organ-scale mechanical and electrical responses. Finally, I describe ongoing and future studies which exploit these new capabilities for multiscale measurements of electrical and mechanical dynamics.

MULTISCALE MEASUREMENTS OF ELECTRICAL & MECHANICAL CELLULAR DYNAMICS

by

Phillip Henry Alvarez

Dissertation submitted to the Faculty of the Graduate School of the
University of Maryland, College Park, in partial fulfillment
of the requirements for the degree of
Doctor of Philosophy
2023

Advisory Committee:
Professor Wolfgang Losert, Chair
Professor Rajarshi Roy
Associate Professor Kimberly Stroka
Adjunct Associate Professor Hari Shroff
Associate Professor Behtash Babadi, Dean's Representative

Table of Contents

List of Figures

List of Abbreviations

ABP	Actin-Binding Protein
AD	Alzheimer's disease
AFM	atomic force microscopy
AMPA	α-amino-3-hydroxy-5-methyl-4-isoxazolepropionic acid
ATPase	Adenosine Triphosphate
BNS	Boulder Nonlinear Systems, Inc.
CICR	Calcium-Induced Calcium Release
CNS	Central Nervous System
DAQ	Data Acquisition
DIC	Differential Interference Contrast
DIV	Days In-Vitro
DMD	Digital Micromirror Devices
DMSO	Dimethyl Sulfoxide
DV	Dorsal-Ventral
ECM	Extracellular Matrix
ENS	Enteric Nervous System
FAK	Focal Adhesion Kinase
FDA	Food and Drug Administration
FFT	Fast Fourier Transform
FRAP	Fluorescence Recovery After Photobleaching

FWHM	Full-Width at Half-Maximum
FoV	Field of View
GI	Gastrointestinal
HEK	Human Embryonic Kidney
hNPC	human Neural Progenitor Cells
IACUC	Institutional Animal Care and Use Committee
IBS	Irritable Bowel Syndrome
ICC	Interstitial Cells of Cajal
LoG	Laplacian of Gaussian
MEA	Micro-Electrode Array
MSM	Multiscale Microscope
NA	Numerical Aperture
NMDA	N-Methyl-D-Aspartate
PA	Posterior-Anterior
PBS	Phosphate-Buffered Solution
PCL	Polycaprolactone
PDL	Poly-D-lysine
PDMS	Polydimethyl Siloxane
PIV	Particle Image Velocimetry
PLA	Polylactic Acid
PSD	Power Spectral Density
PSD-95	Postsynaptic Density Protein 95

RCM	Rescan Confocal Module
ROI	Region of Interest
RyR	Ryanodine Receptor
SLM	Spatial Light Modulator
SNR	Signal-to-Noise Ratio
ST	Spatio-Temporal
STDP	Spike-Timing-Dependent Plasticity
STED	Stimulated Emission Depletion
STEN-CEN	Signal-Transduction Excitable Network and Cytoskeletal Excitable Network
TINd	Tau-Induced Neurodegeneration
TIRF	Total Internal Reflection Fluorescence

Chapter 1: Introduction

Information flow in the brain involves processes operating on a wide range of timescales: The timescale of a long-term memory, for example, is distinct from the timescale of an action or a reaction. While it is possible to achieve a wide range of timescales simply by using separate electro-chemical pathways, brain operations on different timescales are coupled and hence the pathways must be connected.

Electro-chemical pathways yield excitability with oscillations and waves, which allow the brain to process information. Such electrochemical waves and oscillations occur throughout all excitable cells but may not be the only basis for information transfer in the brain. Recent research has shown that the proteins responsible for mechanical response also exhibit excitability. The cytoskeleton, the continuously reorganizing polymer skeleton of the cell, is the primary biochemical mechanism underpinning cellular mechanical structure and response. It has been shown to have waves and oscillations of polymerization and depolymerization, which can be modulated by excitatory and inhibitory inputs and stimuli. These waves of cytoskeletal activity occur throughout excitable cells and are a key component of the brain's plasticity. Like the aforementioned excitable electro-chemical pathways, excitable biomechanical pathways operate on their own timescale as well, but must couple to other pathways to allow the brain to function as intended.

The functional consequences of mechanical excitability and its coupling to electro-chemical excitability, however, are not well understood. This is primarily due to electrical and mechanical dynamics occurring at very different spatial and temporal scales. This mismatch in spatiotemporal scales, with mechanical waves occurring at the scale of seconds and hundreds of nanometers and electrical waves occurring at the scale of milliseconds and millimeters, prevents current commercial microscopes from visualizing the coupling between these two systems.

This dissertation highlights this need for multiscale imaging systems with investigations into electrical, mechanical, and coupled electrical-mechanical signals across scales. It also addresses this challenge through the development of multiscale-capable analysis algorithms and the creation of two custom optical systems built to image cellular and subcellular mechanical activity on the nanometer/second scale, electrical activity on the millimeter/millisecond scale, and coupled electrical-mechanical responses on the tissue and whole organ scale simultaneously.

A thorough review of background information surrounding electrical and mechanical signaling is given in Chapter 2. Bio-electrical signal transmission has been studied for hundreds of years and is well understood both inside and outside the cell. I cover these intracellular, transcellular, and intercellular mechanisms of electrical signal propagation, while also highlighting pathways that could interact with mechanical response proteins. Current methods of imaging this activity are also covered. The study of mechanical signal transmission is, however, still nascent, having only had appropriate tools to investigate it since the end of the 20th century. A similar overview

of the cytoskeleton and its intracellular, transcellular, and intercellular mechanisms is given, along with methods of imaging. Finally, I discuss mechanisms by which the cytoskeleton and electrical responses can influence each other, the implications these interactions may have on known methods of information transmission, and current challenges in imaging and analyzing such interactions.

In Chapter 3, I image directly the spatial and functional effects of continuous mechanical stimulation. I investigate the ability of ridged polymer scaffolds to align processes in-vitro, and the consequences of this alignment on a functional network of primary rat neurons. I find that the polymer scaffolds robustly align processes, with variations in strength of alignment corresponding to ridge pitch and cell plating density. I also analyze this alignment in 3D using super-resolution microscopy, showing that alignment decreases rapidly away from the coverslip so that processes on ridged scaffolds may form 3D networks. Counterintuitively, I also show that the functional network created by the neurons displays no spatial asymmetry in connection strength, indicating an important decoupling between the spatial and functional neuronal networks.

Chapter 4 introduces a multiscale capable mechanical signal analysis algorithm used in two collaborative studies of cytoskeletal dynamics in individual cells and electro-chemical responses in whole organs, respectively. In the first study, focused on the cytoskeletal response to ridged scaffolds as used in Chapter 3, we pioneer a new optical flow-based method for detecting and tracking actin dynamics and show that

actin polymerization waves in multiple cell types are robustly guided by ridged scaffolds. In the second study, we use the same method to analyze the response of a whole crayfish gut to nerve disruption and neurotransmitter perfusion, demonstrating its ability to function across scales. Optical flow analysis reveals that lateral motion and contraction power in crayfish guts are regulated by the N7 nerve cord and can be partially recovered after N7 neurectomy through bath application of serotonin. This analysis method is a primary example of a multiscale analysis which can be used to track intracellular, intercellular, and even whole organ waves and oscillations in electrical and mechanical activity and is key to our future studies of electrical and mechanical coupling.

After describing experimental and analytical platforms I have used to investigate electrical and mechanical signals, I provide an overview of two dedicated optical systems I designed and built for simultaneous imaging of these signals and their functional consequences. The first is a custom inverted microscope, known as the Multiscale Microscope, which contains both a high magnification, super-resolution rescan confocal path and a low magnification, high speed epifluorescence path imaged through the same objective at a standard petri dish or multiwell plate. I show the optical path and outline current experiments being done on this system. The second microscope is a hybrid system containing two separate microscopes working together. Each microscope has its own objective, one of which is upright, and the other inverted. The inverted microscope is a standard epifluorescence microscope able to image cell sheets, the surface of tissue slices, and whole organs at frame rates

up to 1 kHz. The upright microscope is a multiphoton microscope coupled with a fast spatial light modulator able to image cytoskeletal dynamics and stimulate neuronal activity in individual cells and in 3D tissues. These two independent microscopes image the same sample at the same time to provide a closed feedback loop of observing, analyzing, and driving network activity in dynamic excitable systems at the single cell, tissue, and organ scale. As before, I outline the optical path, including a novel implementation of our spatial light modulator to reduce holographic artifacts, and ongoing experiments.

Finally, in Chapter 6, I provide a perspective on how these developments may impact biophysics & neuroscience and what additional questions and avenues of research may be driven by my work. Specifically, I give an overview of how the ability to train networks and elicit specific patterns of activity may allow researchers to not just observe electrical and mechanical coupling, but drive it, creating spatially biased networks which can successfully recapitulate network morphologies seen in living brains. These training methods work in conjunction with the new optical systems that I have created, and network inputs can be generated through real-time feedback loops. I also cover how multiscale simultaneous imaging can be used to improve our knowledge of the functional consequences of actin-synaptic coupling. Finally, I outline how dramatically different spatial scales allow for the imaging of network activity of neuronal networks grown on multiple patterned scaffolds simultaneously while imaging the distinct actin responses in each of them independently. Additional

hypotheses regarding mechanical methods of information flow in the brain, and their clinical consequences, are also discussed.

Chapter 2: Background

Outline

Information flow in many cell networks is well known to occur electrically. This chapter starts with a review of cellular electrical transmission and describes methods for recording electrical activity in excitable cell networks, including optical imaging approaches that allow us to measure electrical activity at the network scale yet with subcellular resolution. The second section of the chapter introduces the often-overlooked mechanical aspects of signaling. The final section describes what is known about the coupling between electrical and mechanical signaling, including the main challenges in optical imaging of the mechanisms and functional effects of this coupling, and contextualizes the aims of this dissertation.

Intra- and Extracellular Electrical Signals

Intracellular Ion Trafficking

The study of electrical information flow in neural networks is well established. Indeed, studies of biological electricity preceded the creation of the voltaic pile, the first battery, by Alessandro Volta in 1799. The development of the battery inspired an entire field of electronics and materials science dedicated to portable electrical devices. Volta, in turn, was inspired by the observed responses to direct electrical stimulation in the nervous system of animals [1]. Scientists of the 1800s built on these studies, discovering that electricity flows through animals in discrete nerve bundles made of cells [2]. These cells, neurons, were found to have innate voltages (membrane potentials) of their own which could be stimulated to rise

and fall transiently with external excitation [3]. This transient voltage fluctuation, lasting between 1-2ms, gained a name, the action potential. Neurons were also found to have projections which acted as inputs, called dendrites, and one output projection, called an axon. In the early 1900s, bioelectricity pioneer Kenneth Cole confirmed that this action potential involved a distinct change in conductance [4]. As ions in solution were already known to be the main carriers of extracellular charge, this narrowed the mechanistic search for the action potential to ion fluxes, specifically sodium and potassium. This search culminated in the pioneering work by Hodgkin and Huxley, modeling the action potential via coupled differential equations and quantitatively describing the action potential and its sodium and potassium dependence through voltage clamp of a giant squid axon [5]. Electrical transmission along axons and dendrites was also found to obey cable theory, a foundational model in electrostatics regarding electrical signal propagation along insulated coaxial cables [6].

Voltage-gated sodium and potassium pumps, as described by Hodgkin and Huxley and further works, serve as fundamental regulators of neuronal membrane potential and underlie the multi-stage dynamics of the action potential [7]. The action potential has four distinct phases.

The first phase is typically known as the rising phase, where neurons rise from their resting potential of approximately -70 mV upwards towards positive voltages. This phase occurs because of voltage-gated sodium channels allowing in high concentrations of Na^+ from extracellular fluid to the cytoplasm [8]. Meanwhile K^+, existing in higher concentrations in intracellular fluid than the extracellular fluid, leaks out through voltage gated potassium channels [7].

The second phase is the peak phase, where the neuron reaches approximately the equilibrium potential of sodium at approximately +50 mV. However, as the membrane potential reaches its maximum, the sodium channels close and potassium channels open, pumping K+ ions back into the cell [7].

The third phase is known as hyperpolarization, where K+ ion influx drops the membrane potential back down towards resting potential. Calcium ions also rush into the cell during this phase, triggering more potassium channels to open, flooding the cell with K+ and pushing the cell past the resting potential and very close to the equilibrium potential of potassium, approximately -90mV [7]. This calcium influx also synchronizes the mitochondrial metabolism, of which calcium is a key regulator, to neuronal electrical activity [9]. The calcium influx typically lasts much longer than the action potential, by at least a time factor of ten [10]. This time-delayed signal is useful to researchers as a slower measure of neuronal activity for applications in which the millisecond timescale of sodium and potassium activity is too fast for detection. The calcium signaling also synchronizes the trafficking and release of neurotransmitters (such as serotonin and glutamate) from synapses (junction points between neurons) bundled within lipid shells known as synaptic vesicles [11]. This phase ends as potassium channels close and K+ leakage brings the cell back to the resting potential [7].

The fourth and final phase is the refractory period, where the channels undergo a conformational change to block the channel to further transmission of ions temporarily. This period sees the neuron transition fully back to resting state for some period [7].

Transmembrane Response to External Electric Fields

This entire cycle can be triggered through changes in extracellular or intracellular ion concentration, through the release of neurotransmitters into the neuron from a neighboring one through a connected channel, and through changes in external electric field [7]. This last effect is often exploited for targeted stimulation of neurons via electrodes, which temporarily expose neurons to electric fields to drive open sodium and potassium channels [12].

Other electrically excitable cells can have unique responses to these external electric fields. For example, cardiomyocytes, which are also electrically excitable just as neurons are, are also stimulated by external electric fields such as in defibrillation. Notably, cardiomyocytes also have biochemical pathways to release calcium from sarcoplasmic reticulum during calcium influx, a process called calcium-induced calcium-release (CICR). CICR is thought to serve as a basis for a coupling mechanism between cellular excitation and muscle contraction, driven by the sarcoplasmic reticulum (further discussed in section 2.3) [13]. Astrocytes, another type of neural cell involved in homeostasis and thought to play a part in synaptic transmission and regulation, lack sodium and potassium channels but can be stimulated to produce calcium currents. These astrocytic calcium currents are thought to act as a mechanism for integrating signals from synapses [14]. Their behavior is also similarly regulated by changes in external ion concentration [15].

Transcellular Junctions and Intercellular Electrical Communications

Cells have many mechanisms by which they transfer these electrical signals to other cells in a population. In cardiomyocytes, this mechanism takes the form of gap junctions [16]. Gap junctions are direct cytoplasmic connections between neighboring cardiomyocytes which form at broadside connections between cells and allow various intercellular signaling molecules to flow through. Astrocytes, on the other hand, have tight junctions, which are like gap junctions but watertight [17].

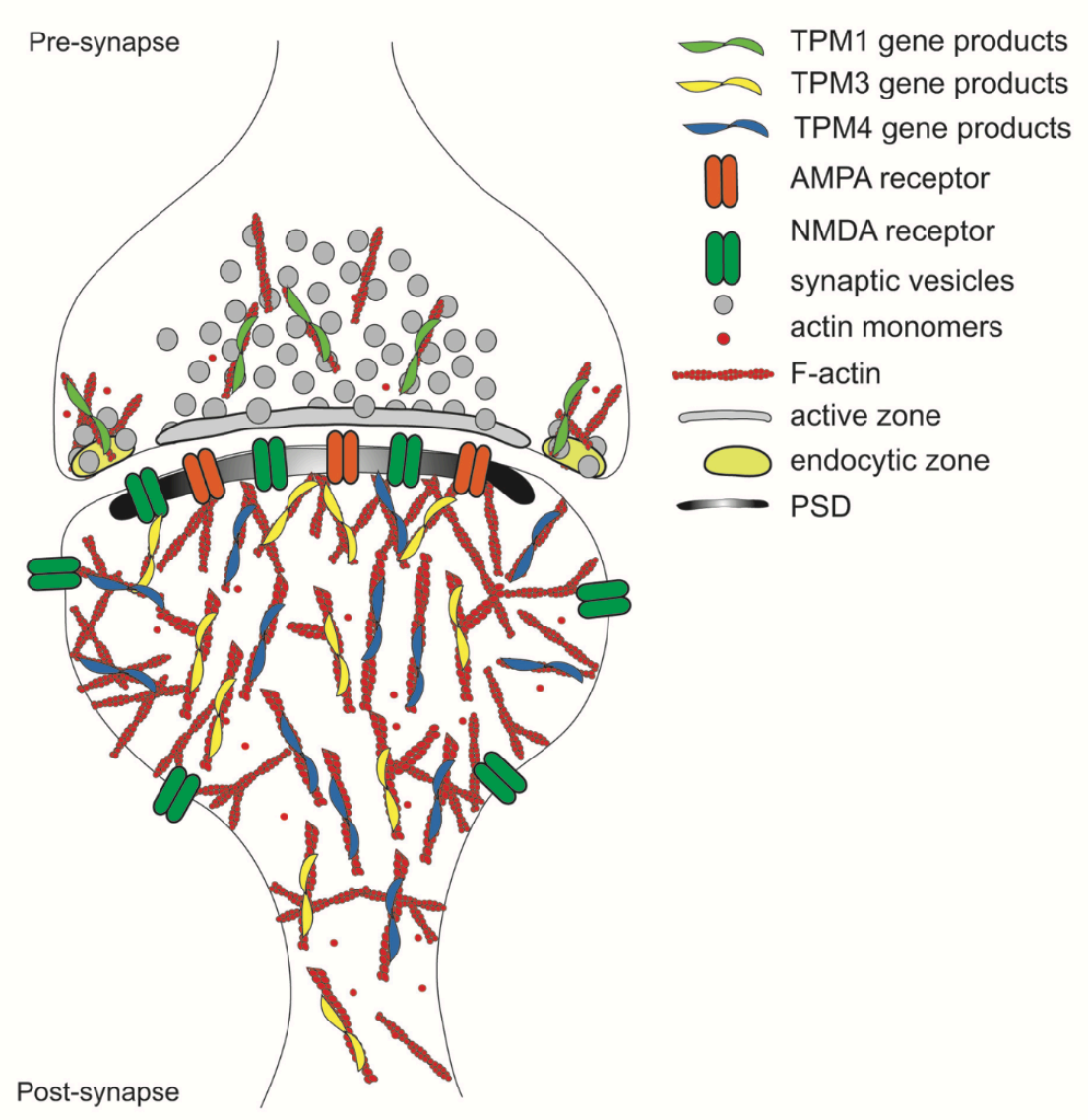

Figure 1: Diagram of a synapse showing major proteins and channels, as well as the supporting structure of the cytoskeleton. [TPM3 and TPM4 gene products segregate to the postsynaptic region of central nervous system synapses, Guven, et. al, BioArchecture, © 2011, reprinted by permission of Informa UK Limited]

Neurons, instead of having broadside connections, are linked by discrete junction points along processes, the previously mentioned synapses. These synapses are formed at small projections along dendrites called dendritic spines. Each neuron has, on average, thousands of synapses through which it connects to and communicates with other neurons [18, 19]. These synapses vary in "strength", or efficiency at delivering biochemical signals between neurons to trigger action potentials. Neuronal networks can strength or weaken synapses in real-time, a process known as plasticity [20]. A primary regulator of synaptic strength is firing synchronicity, or the relative timing of an action potential in a pre-synaptic neuron with an action potential in a post-synaptic neuron, a process known as Hebbian plasticity [21]. Hebbian plasticity is often summed up in the axiom "neurons that fire together wire together". The mechanism by which Hebbian plasticity occurs is known as STDP, or spike-timing-dependent plasticity (spike being synonymous with action potentials). STDP occurs via an increase in dendritic spine size, ion channel count and density, and dynamic remodeling of the cytoskeleton inside the dendritic spine after a period of synchronized neuronal activity [22]. Also increased are neurotransmitter channels like AMPA and NMDA (glutamate-based fast synaptic transmitters), and a series of actin binding proteins such as tropomyosin which act as a link between actin activity and calcium influx in the synapse (discussed in more detail in 2.3) [23]. A detailed graphic of this process can be seen in Fig. 2, where a dendritic spine is either growing or shrinking due to changes in long-term potentiation

(synaptic strength) driven by STDP. After STDP, these spines have a larger size with internal features reflecting stronger and more efficient transmission of signals [22]. Experiments in STDP have shown that neurons are recruited via STDP when their pre-synaptic spike occurs within approximately 10ms of a post-synaptic spike [24]. This process of STDP is one of the foundations of hippocampal learning and short-

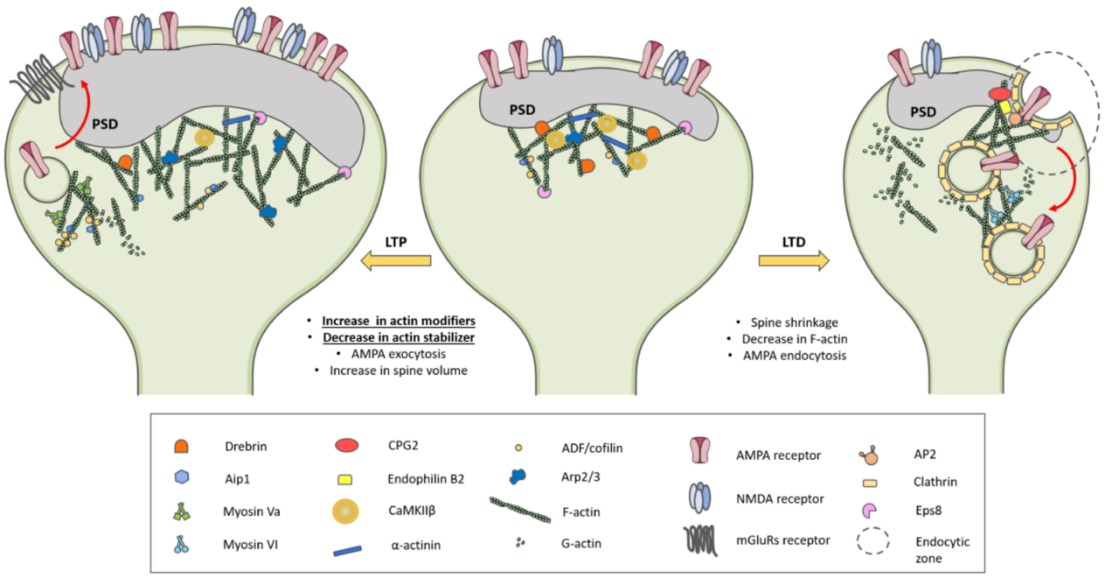

Figure 2: Diagram showing the relative increase in dendritic spine size, channel count, actin-binding proteins, and remodeled cytoskeleton due to long term potentiation driven by STDP, and decrease in these same parameters due to long term depression driven by uncorrelated activity. Also shown are a series of actin-binding proteins that help mediate this growing and shrinking and can modify F-actin through several process, such as severing (cofilin), branching (Arp2/3), or capping (Aip1). [Dendritic Spines in Alzheimer's Disease: How the Actin Cytoskeleton Contributes to Synaptic Failure, Pelucchi et. al, 2020, reprinted by permission of Int. J. Mol. Sci.]

term memory.

Other non-direct forms of intercellular communication also exist in excitable cells. Neurons and other neural cells can release neuronal transmitters directly to the extracellular fluid during action potentials [7]. This serves as a mechanism by which neurons can find other neurons during neuronal network development and as a regulator of network-wide activity [25].

The network of electrically excitable cells created by these intracellular contacts forms the basis for information processing, especially in neurons [26]. Neurons will typically connect and form networks specific to particular tasks. In the cortex, columns of high-connectivity networks, called cortical columns, contain layered structures through which information is processed and passed between layers, as in a software analysis pipeline where data is passed from routine to routine [27]. Notably, however, the spatial arrangement of a particular neuronal network is related to, but not solely deterministic of, its function. Researchers more recently have established that information itself is not simply encoded in individual synaptic connections, but in the dynamic firing patterns of groups of neurons in established networks [28]. To investigate these firing patterns, neuroscientists typically examine the "functional networks" of neurons, or networks of neuronal connections weighted by synaptic strength. These functional networks represent static maps that show how information is flowing through a network by showing which groups of neurons are most likely to fire together and which neurons are key drivers of network activity. Because synaptic strength is difficult to visualize, downstream metrics such as firing correlations, which rely on the previously established Hebbian assumption to infer synaptic strength, are used [29]. Probing these networks to understand their function and architecture is the basis for large portions of research modern-day neuroscience, and the goal of many newly developed experimental techniques.

Imaging Electrical Responses

To interrogate these electrical responses in cells and bulk tissue electrical responses, researchers first used electrodes inserted into neurons in large mammals, or extracellular electrodes placed in neural tissue. However, imaging intracellular electrical dynamics in most mammalian cells requires significantly more complex techniques. There are several methods used, each with their own strengths and limitations. These most popular of these techniques include patch clamp electrophysiology, micro-electrode arrays, calcium dyes, and voltage-sensitive dyes.

Patch clamp electrophysiology is among the oldest techniques for studying the electrical dynamics of mammalian cells. It involves aspirating a small portion of a cell via a micropipette filled with an electrode and electrolyte. This aspiration typically breaks the cell membrane, coupling the intracellular fluid to the electrode in the micropipette. Patch clamp electrophysiology is extremely sensitive to real-time changes in membrane potential, synaptic currents, and can be used to precisely control the opening and closing of neuronal channels through changes in applied electrode voltage [30]. Patch clamp electrophysiology, though, has a few notable shortcomings, including its steep requirement for expertise on behalf of the user and difficulty in recording activity from multiple neurons [31].

Another technique in electrophysiology which allows for recording of activity of many neurons simultaneously is the use of MEAs (Micro-Electrode Arrays). MEAs are composed of series of electrodes typically separated by tens or hundreds of microns. These electrodes are sensitive to bulk changes in potential of the neurons between them. MEAs are popular for investigating network-scale dynamics both in-

vitro and in-vivo [32]. MEAs come with their own downsides, however, including an opposing scale issue to patch clamps. Many neurons can be recorded from at once, but MEAs have great difficulty recording activity from individual neurons. Additionally, the signal-to-noise ratio is much lower than patch clamps due to the monitoring of changes in the extracellular electric field rather than the membrane potential or intracellular ion flows [33].

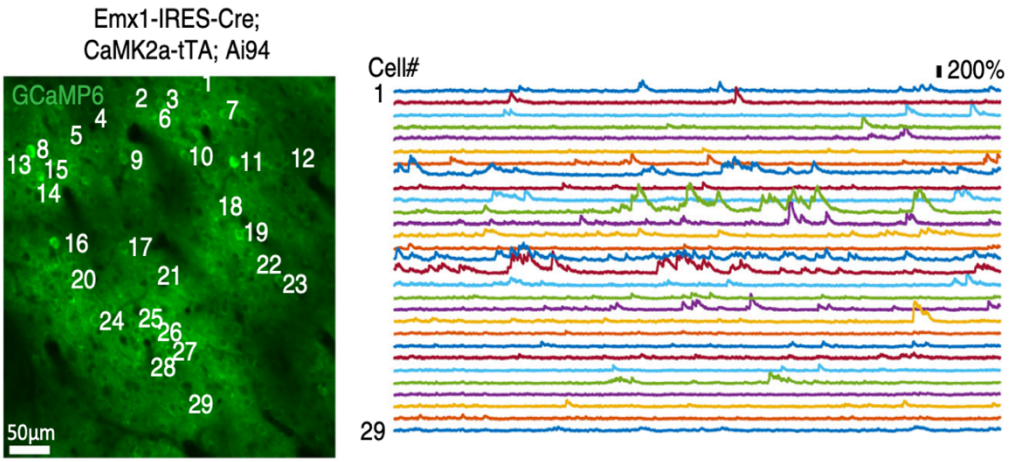

Figure 3: Left: Image of neurons in mouse visual cortex labeled with genetically encoded fluorescent calcium indicator. Right: Corresponding activity traces of each labeled cell, recorded over 250 seconds. [Neuronal cell-subtype specificity of neural synchronization in mouse primary visual cortex, Knoblich et. al, 2019, reprinted by permission of Nat. Comm.]

A more recent advancement in neuroscience has been the development of all-optical electrophysiology using light microscopy. Light microscopy has many advantages as a method to monitor neuronal dynamics compared to patch clamps or MEAs. Light microscopy can collect data from multiple scales very easily. Single neurons can be monitored from the same system as whole neuronal tissues by changing objective lenses [34]. Proteins inside cells can be monitored through fluorescent dyes and genetically encoded fluorescent tags. By shining light of a

particular wavelength on cells, these pre-labeled proteins and their movements can be visualized in the absence of all others, a technique known as fluorescence microscopy. Fluorescence microscopy, and light microscopy broadly, has traditionally been used by neuroscientists to visualize the morphology or configuration of neural cells as well as protein and molecule trafficking [35].

Calcium-binding fluorescent molecules with fluorescence properties enabling widespread use were first developed in the 1980s [36]. These dyes are now typically either cell-permeable or genetically encoded and can visualize intracellular changes in calcium with high spatial and temporal resolution [37]. As previously noted, calcium flux is an adjunct response to neuronal action potentials but occurs at a significantly slower rate. This slower rate is advantageous for light microscopy, as recording action potential dynamics at the rate at which they occur typically involves the use of expensive high-speed cameras and requires high intensity excitation light, due to short exposure times, which can induce photodamage. Because light microscopy can visualize single neurons in large FoVs (Fields of View), calcium imaging can investigate both intra- and intercellular signaling in large groups of neurons simultaneously. An example in-vivo image of an active neuronal network is seen in Fig. 3. Individual neurons can be segmented, and their electrical dynamics tracked over time.

Beyond calcium dyes, newer voltage-sensitive fluorescent molecules have been developed which can allow for optical imaging of the cellular membrane potential directly [38]. The kinetics of these molecules differ, but all respond to changes in membrane potential by a real-time change in fluorescence. Because this

real-time change in fluorescence occurs at the timescale of the action potential, voltage-sensitive dyes require the previously mentioned high-speed cameras and higher intensity excitation light, but can provide extremely precise, high temporal resolution recordings of neuronal activity at the single cell and tissue scale.

Both calcium and voltage-sensitive dyes can be used in-vitro or in-vivo [39, 40]. The former is typically accomplished with traditional epifluorescence microscopes, composed of a wavelength specific light source, detector, or both coupled to a compound microscope. Confocal microscopes, which employ pinholes in the detection path to provide a focal-plane-specific view of the sample (also called optical sectioning) are also used. In-vivo use typically requires multiphoton microscopes, which exploit the multiphoton effect (where extremely high peak intensity laser light is used to excite fluorophores at the focal spot of an objective) and femtosecond infrared lasers to image with optical sectioning at depths up to 400 microns in the brain [35, 41-43]. Multiphoton microscopy is discussed in more detail in Chapter 5.2. Importantly, any sort of optical imaging of electrical activity places emphasis on high speeds, to better resolve calcium or voltage dynamics, and large FoVs, which allows for imaging of the electrical activity of exponentially more neurons as the FoV grows (and therefore larger population dynamics) [44, 45].

Intra- and Extracellular Mechanical Signals

Unlike the mechanisms and pathways underpinning electrical signal propagation in cells which has been studied for over 200 years, the study of mechanical signal propagation is comparatively nascent. Neurons and other electrically excitable cells typically experience an extracellular environment rich with

mechanical cues, such as collagen fibers, perineuronal nets, and structured aggregates of other cell types [46-49]. The cytoskeleton, literally meaning “cellular skeleton”, is a set of polymer proteins with varying stiffness, polymerization speeds, and specific functions, and is a main component of the response system for mechanical cues.

The Cytoskeleton as a Mechanical Response System

The cytoskeleton is composed of three major constituents. The first are microtubules, which are very stiff, long polymers of tubulin approximately 25nm in diameter that give the cell its overall shape and act as a backbone through which nutrients are trafficked around the cell. The second are intermediate filaments, the least studied of the three constituent proteins, composed of mid-sized polymer chains, approximately 10nm in diameter, like keratin, that help support cell-cell adhesion. The final component is actin, a highly responsive polymer network composed of much smaller polymer chains (7nm or less in diameter) that underpin fast morphological dynamics such as membrane ruffling, lamellipodial protrusion, and filopodial protrusion. Polymerization and de-polymerization of these proteins is triggered by an array of intracellular and transcellular signaling cues, though not all these pathways are well-understood [50, 51].

The cytoskeleton serves a crucial array of roles in electrically excitable cells. Microtubules move neurotransmitters and excitatory or inhibitory proteins in vesicles toward and away from cell-cell junctions [50]. On a smaller scale, changes in synaptic size and strength are accompanied by remodeling events in the actin cytoskeleton at dendritic spines, described in 2.1.3 as the sites at which synapses form along dendrites [23]. These changes in synaptic strength typically take place during

plasticity events such as STDP [24]. This synapse-actin link, along with actin's other known roles in supporting other types of cell-cell junctions (i.e., gap junctions and tight junctions), implies an important biomechanical role for actin in the formation of functional neuronal networks.

Spurred by advances in live-cell fluorescence microscopy, researchers at the turn of the 21st century directly visualized actin waves propagating in migrating Dictyostelium Discoidium cells [52]. These waveforms were thought to be a driver of migration, with waves pushing the cell front outwards towards biochemical cues. Prior to that discovery, though, researchers had already studied fairly extensively the phenomenon of wave-like lamellipodia in neurites [53]. These wave-like lamellopodia were found to be actin-dependent, though neurite outgrowth itself conversely is microtubule dependent [53].

As faster, optically sectioned confocal microscopy became widely used in cell biology, researchers were able to fully sample these mechanical responses in real time. Actin and microtubules were shown to continuously remodel over the scale of seconds and minutes, growing, shrinking, and exchanging subunits in a process called treadmilling [54]. To probe these dynamics, mechanical stimulation became common. Instead of rheology, one of the earliest forms of mechanical testing of cellular tissues, researchers began using instruments such as optical tweezers, which stretch and compress cells using lasers, atomic force microscopes, which use nanoscopic cantilevers to probe cells, and patterned growth scaffolds, which provide continuous mechanical cues through rigid or semi-rigid patterns imprinted on coverslips [55].

This latter method, patterned scaffolds, has been shown to reliably induce both simple and complex waveforms in a variety of cell lines. Ridged scaffolds produce linear polymerization waves in actin [56]. Dots or nanopillars act as nucleation points [56]. Sawteeth act as unidirectional guidance cues [57]. These waveforms also drive changes in migration, though different cell lines can act differently when exposed to different patterns, such as tumorigenic and non-tumorigenic breast epithelial cells preferring opposite directions to migrate with respect to sawteeth (with the teeth vs against the teeth) [58].

Cytoskeletal Dynamics as an Excitable System

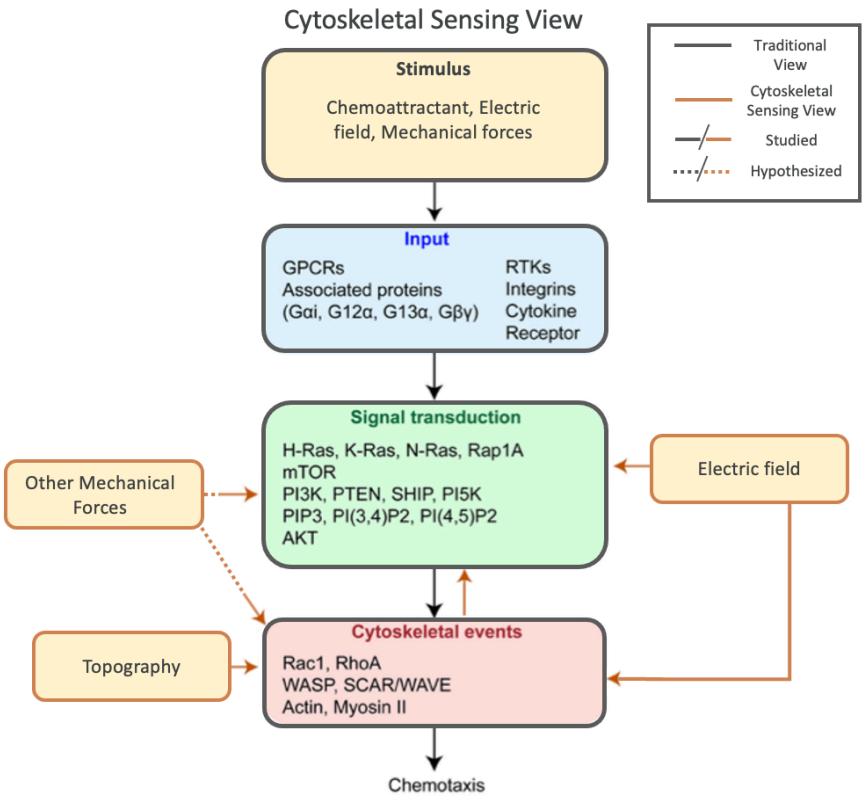

Figure 4: Simplified overview of the biochemical signaling pathway of the cytoskeleton incorporating studied and hypothesized physical cue sensing elements and cytoskeletal feedback loop. [The excitable signal transduction networks: movers and shapers of eukaryotic cell migration, Pal et. al, 2019, reprinted and modified with "cytoskeletal sensing" components by permission of Int. J. Dev. Biol.]

Cellular biologists typically think of the cytoskeleton as an array of mechanical response proteins activated and regulated by upstream signaling molecules such as PIP3, PTEN, and K-Ras [51]. Transduction of physical cues into cytoskeletal polymerization waves is not very well understood, but typically it involves the up- or down-regulation of transmembrane regulatory proteins, which in turn cause the activation or inhibition of signal transduction factors, which eventually

trigger actin polymerization. A simplified view of this mechanism is shown above in Fig. 4 outlined in black. This view has been challenged by recent work, however, which has shown that actin is an excitable system in itself [59]. Excitable systems are defined by the ability to have critical thresholds for activity, transmit waves, and the existence of a refractory period. Many in-vitro experiments, and some in-vivo experiments, have demonstrated the ability of actin to have an activation threshold for polymerization, form waves (actin waves and retrograde flow are well established, especially in adherent cells), and have refractory periods, similar to electrical activity [60-62]. Recent work has described the excitable characteristics of actin and its associated proteins as a coupled signal-transduction excitable network and cytoskeletal excitable network (STEN-CEN). Tuning key components in the STEN-CEN pathway has been shown to change wave patterns, and activator/inhibitor, reaction/diffusion models successfully recapitulate its behavior [63]. These excitable dynamics of actin go beyond being another link in a signaling pathway and suggest interesting emergent phenomena. It also underpins the hypothesis that the cytoskeleton may act as another form of information transmission within and between cells. This is most apparent in wound healing, where coordinated waves of actin and myosin (a molecular motor which pulls on polymerized actin to generate force) direct cell migration towards the site of the wound [64].

The excitable system of actin may also not be as “downstream” as previous work suggests. More recent work, particularly that done in our lab, has shown that actin inhibition results in quiescence of many other signaling factors typically thought to be “upstream” of actin [62]. This suggests the existence of a feedback mechanism,

that actin polymerization may in turn result in upregulation or downregulation of actin-related signal transduction proteins. The cytoskeleton may also be a missing sensor of surface texture. Stress, strain, and disruptions in polymerization waves by membrane deformations are all known to alter polymerization dynamics, and therefore feed back into the array of signaling molecules [51]. This modified view is also shown in Fig. 4 outlined in orange. This could further indicate the cytoskeleton's role as an information processing mechanism, translating environmental cues into factors which, when upregulated and downregulated, not only result in changes in intracellular behavior but also modify electrical and chemical signaling to neighboring cells through cell-cell junctions.

Imaging the Biomechanical Excitable System

As previously mentioned, the study of the cytoskeleton has been heavily driven by advances in imaging. Early microscopy was unable to visualize cytoskeletal proteins without disrupting or destroying the cell membrane as the cytoskeleton exists in a biochemically rich environment, and more basic techniques such as brightfield microscopy or differential interference contrast (DIC) struggle to separate actin, tubulin or intermediate filaments from other cytosolic proteins [65].

The advent of fluorescence microscopy, however, has allowed researchers to directly label and visualize specific components of the cytoskeleton, such as individual actin filaments and tubulin, and their associated signaling factors such as PIP3 or PI3 kinase [66, 67]. Confocal fluorescence microscopy in particular is heavily used in in-vitro studies of the cytoskeleton due to its ability to view the cell slice-by-

slice [67]. This ability is key when investigating cytoskeletal dynamics. Many polymerization-promoting complexes such as focal adhesions are formed at the cell-surface interface, and therefore polymerization dynamics close to the coverslip are very different than those occurring towards the top of the cell [62]. Other, similar techniques such as TIRF (total internal reflection fluorescence) or light sheet microscopy which also illuminate only thin layers of the cell with excitation light are also utilized [68, 69].

FRAP (fluorescence recovery after photobleaching), a technique that analyzes the temporal dynamics of fluorescence in addition to the spatial localization of the fluorescence, has also allowed researchers to study the movement and exchange of individual monomers and dimers, providing insight into the molecular mechanisms that drive cytoskeletal remodeling [70].

Major advances are now being made into super-resolution microscopy, an array of techniques which allow for visualizing structures with a level of detail below the diffraction limit. Techniques such as STED (Stimulated Emission Depletion) and Airyscan microscopy have demonstrated the ability to visualize cytoskeletal filaments at high resolution in live cells, providing a detailed view of the molecular organization of the cytoskeleton [66]. However, this disparate set of imaging methods and tools has also caused a lack of standardization in analysis toolsets. Unlike optical electrophysiology where calcium imaging and correlation networks are very common, mechanical imaging often relies on analysis tools developed ad-hoc and tailored to specific experimental workflows, such as the use of particle image velocimetry to study actin wave morphologies, simple displacement tracking to study migration or

wave velocities, or Fourier-domain analysis to study bulk alignments of filamentous actin [71-74]. This lack of standardization has led to a lack of algorithms proven to work across multiple imaging scales, so cytoskeletal responses in one cell type might prove difficult to image reliably in a different cell type, or even in larger fields of view such as on the tissue scale or organism scale, to measure bulk responses.

Common among the outlined imaging schemes is that for cytoskeletal imaging, emphasis is placed on spatial resolution, rather than temporal resolution as in electrical imaging. Cytoskeletal dynamics take place over seconds to minutes, rather than milliseconds, and involve the trafficking and assembly of proteins and protein assemblies much less than a micron in size [67]. This diametrically opposed set of needs for cytoskeletal imaging, slow, high-resolution rather than the electrical system's need for fast, large FoV imaging, has proven challenging for researchers seeking to visualize both response systems at once.

Electrical & Mechanical Coupling

As previously discussed, the relationship between the cytoskeleton and ion channels also has implications for synaptic transmission and plasticity. The localization and clustering of ion channels at synapses is critical for the proper functioning of these sites of signal transmission. Changes in the mechanical properties of the actin cytoskeleton can alter the distribution and localization of ion channels, influencing synaptic transmission, plasticity, and can modulate ion fluxes directly [75-77]. This can lead to changes in the strength of synaptic connections, changes in the timing and pattern of neurotransmitter release, and modifications in the structure and function of synapses. In other words, it may alter the nature of Hebbian

plasticity itself. Understanding the mechanisms and functional consequences of this coupling between electrical and mechanical signaling is therefore of great importance for fully understanding the nature of information flow in networks of neural cells across spatial and temporal scales, and more broadly, other types of excitable tissue.

The Cytoskeletal Link to Ion Channels

Multiple regulatory proteins and protein pathways are already known to interact with both actin and ion channels, chief among them select ABPs (actin-binding proteins) [66]. Due to the important role the cytoskeleton plays in muscle cells regarding force transduction, cardiomyocytes contain one of the most canonical examples of an ABP acting as a link between actin and ion channels, calcium-induced calcium release (CICR). CICR is a process by which an increase in intracellular calcium ion (Ca2+) concentration leads to the release of more calcium ions from intracellular stores, resulting in a positive feedback loop that amplifies the initial increase in calcium ions.

In heart cells, CICR is initiated by the activation of calcium channels in the cell membrane, which allow an influx of calcium ions into the cell [13]. The resulting increase in intracellular calcium ions activates a protein called ryanodine receptor (RyR), which is located on the sarcoplasmic reticulum, a specialized intracellular organelle that stores calcium ions. Activation of RyR results in the release of calcium ions from the sarcoplasmic reticulum into the cytoplasm, further amplifying the increase in intracellular calcium ions [78].

Actin is involved in regulating CICR in heart cells by modulating the activity of the RyR. Actin-binding proteins (ABPs) can bind to RyR and modulate its activity,

either by stabilizing the open state of the receptor or by inhibiting its opening. For example, ABPs such as troponin I and actin-associated proteins such as calmodulin can bind to RyR directly and stabilize its open state, leading to the sustained release of calcium ions and the maintenance of contraction [78].

The actin cytoskeleton can also physically regulate the localization of RyR in some cells, with the concentration of RyR in proximity to calcium channels being critical for the initiation of CICR [79]. There is also limited evidence that the actin cytoskeleton can modulate the activity of calcium channels themselves by controlling its localization and distribution in the cell membrane, further regulating the influx of calcium ions into the cell and triggering actin dynamics through the troponin/tropomyosin complex [77]. Tropomyosin, an ABP, covers myosin binding sites during periods of low calcium influx, and uncovers them during periods of sufficiently high calcium influx. This synchronizes force transduction events with electrical activity. Tropomyosin complexes exist in neurons as well, and may serve a similar role [80].

In neurons, these ABP-related links between the cytoskeleton and ion channels are less well-studied. However, there are known pathways that involve the regulation and localization of ion channels in neurons by surface-interacting ABP complexes. For example, focal adhesion kinase (FAK) is a protein kinase that plays a key role in the regulation of cell adhesion, migration, and survival. FAK is a key component of the signaling pathways that mediate cell-matrix interactions and is essential for the formation and maintenance of focal adhesions, which are complexes of proteins and carbohydrates that anchor cells to the extracellular matrix on one end

and are known to trigger actin polymerization on the other end [81, 82]. Focal adhesions act as a central hub for integrating signals from various growth factor receptors and integrins (cell-anchoring proteins), transmitting these signals to the intracellular machinery and regulating the dynamics of the cytoskeleton.

There is growing evidence that FAK is also involved in the regulation of ion channel function and membrane potential. For example, the activation of FAK has been shown to increase the activity of potassium channels and to decrease membrane potential. Conversely, potassium channels have been shown to regulate the activity of FAK through modifications in the clustering of integrin receptors, upregulating or downregulating expression of FAK [83, 84].

Actin, shown to play a role in synaptic size and strength regulation already, may also therefore act on proteins like FAK to alter the activity of potassium channels directly, while potassium channel activity may regulate the local polymerization of actin.

Actin as an Integrator of Electric Cues

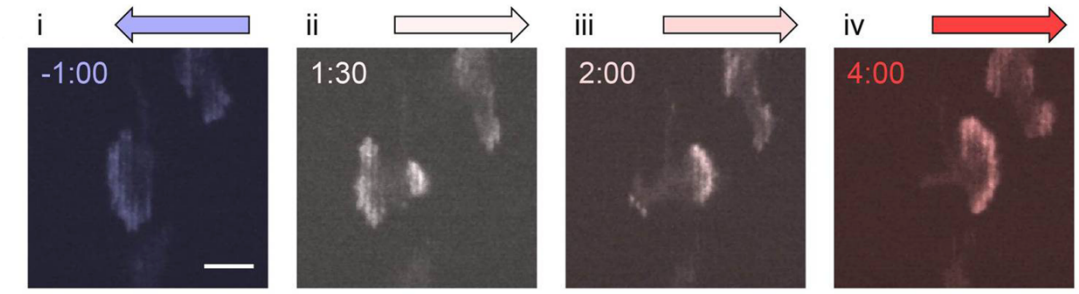

Figure 5: Actin waves in fluorescently labeled neutrophil-like HL60 cells showing a distinct switching in response to a switched electric field direction. Cathode direction is to the left at negative times, and to the right at positive times. Field switch occurs at 0:00. Scale bar represents 10μm. [Actin Dynamics as a Multiscale Integrator of Cellular Guidance Cues, Yang et. al, 2022, reprinted by permission of Front. Cell Dev. Biol.]

Actin may also act as an electric sensor in addition to being a mechanical sensor. Actin waves have been shown to respond directly to a change in the polarity of a globally applied electric field. In the example shown in Fig. 5, HL60 cells exposed to such a field demonstrate a preference for actin polymerization in the cathodal direction before and after field polarity switching [61]. In fused Dictyostelium cells exposed to a constant electric field, actin waves have also been shown to have a prolonged lifetime and wave area. These changes in actin waves occurred gradually over the course of ten minutes, and caused increased protrusions in these cells in the direction of the cathode, ultimately leading to electrotaxis, the directed migration of cells in the presence of such a constant electric field [62]. This gradual polarization of internal cytoskeletal signaling is thought to be the sensing mechanism of migratory, non-excitable cells to such global fields. In such cells, HL60 and Dictyostelium, mechanical and electrical guidance cues have also been put into competition. Researchers have found that such non-excitatory cells seemingly

prioritize mechanical cues such as surface texture in the short term, but over longer time periods integrate electric cues as well to bias surface texture-aligned migration [61].

These electrical responses play a vital role in the body. Wounds inherently create local electric field gradients through changing tissue organization [85]. Cells naturally produce electric fields, and therefore the lack of cells changes local electric field topology. These electric field gradients have been shown to guide cells through electrotaxis in similar ways to that previously described [86]. The biochemical mechanics of how the electrical signal gets transduced to actin waves is not yet known, or if actin itself is inherently electrically responsive despite its weak dipole moment, but it is then established that actin at the very least plays a role in a minute-scale electrical response mechanism and therefore acts as a sensor of physical cues in general, not just mechanical [87].

This minute-scale electrical response system may play a key role in neuronal networks. These timescales are similar to functional short-term memory, currently thought to be a byproduct of local neurotransmitter depletion [88]. Actin may act as another input to this system and generate a feedback loop between itself and other electrical communication machinery.

Challenges in Imaging Electrical and Mechanical Coupling

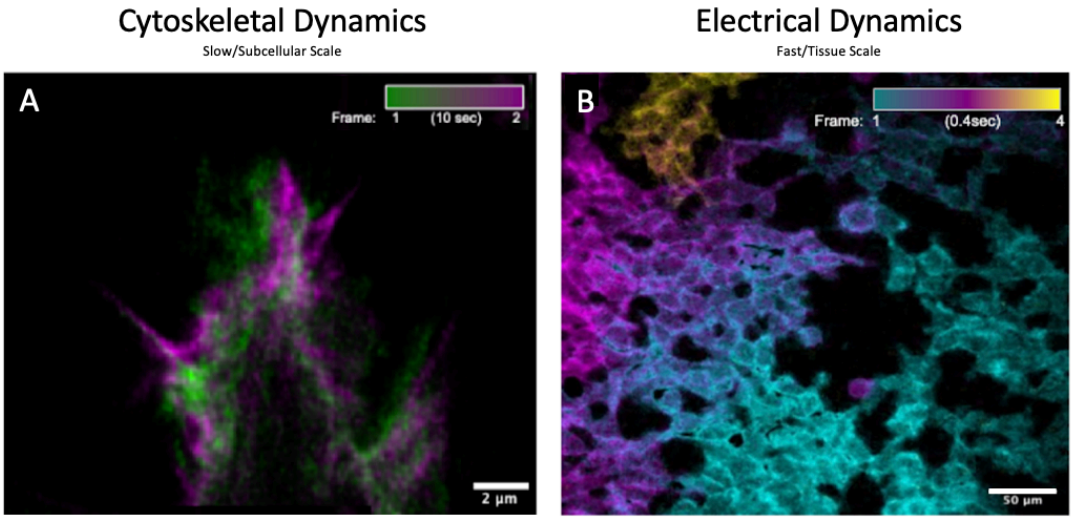

Figure 6: Kymographs showing mismatch in spatiotemporal scales between actin and electrical dynamics in cardiomyocyte-like HEK293/T cells. A: Two subsequent frames, separated by 10 seconds, showing a displacement of less than 10µm in fluorescently labeled F-actin. B: Fluorescent membrane potential indicator in the same cells showing a small portion of a circular electrical wave around a void in the tissue monolayer. The wave crosses the 325µm x 325µm frame in less than 500ms.

The existence of such a feedback loop or other functional consequences of a coupling between the cytoskeleton and electrical communication proteins is yet to be directly established. A key challenge obstructing researchers interested in this interplay, alluded to in section 2.2.3, is the vast spatiotemporal scale difference between the dynamics of the two systems. Visualizing actin, tubulin, or intermediate filaments demands as high of a spatial resolution as possible over the scale of seconds and minutes [67, 89]. Visualizing electrical dynamics on the other hand requires large FoVs with high temporal resolution. This mismatch in scales is highlighted in Fig. 6, where over 10 seconds HEK293/T cells modified to express cardiomyocyte-derived sodium and potassium channels display small changes in actin morphology over a

nanometer to micron scale, while collective electrical activity travels across a factor of 10 larger field of view in less than 500ms. This larger field of view does not appear to capture the entire waveform, but merely a small portion of it.

Large FoVs inherently result in lower numerical aperture objectives and require smaller detector pixels to resolve intracellular details with the same resolution as high magnification objectives. However, low numerical aperture (NA) degrades signal, and ever smaller detector pixels are limited by semiconductor fabrication abilities and quantum efficiency (the efficiency of detection of impinging photons by a semiconductor chip) [90]. High speed acquisition limits imaging methods as well, both through exposure time and placing limitations on scanning equipment. Many optically sectioned microscopy techniques, required for cytoskeletal imaging, require the scanning of a laser across the cell, which dramatically increases acquisition time (as laser scan time becomes a limiting factor). Some, like confocal microscopy, also use a pinhole to reject light from outside the focal plane of the objective, which decreases acquired signal as most light gets rejected by the pinhole [91].

Recent developments in microscopy have tried to avoid these series of tradeoffs. Karel Svoboda, et. al, introduced the mesoscope in 2016 as a method for visualizing large fields of view while retaining single cell resolving power and relatively high NA [92]. However, NAs in mesoscopes are still well below that of traditional high magnification immersion objectives, causing a lower maximum lateral resolution of 660 nanometers, limiting the actin-resolving power of these microscopes to larger scale waves and stress fibers.

Light sheet microscopy is another promising technique that illuminates entire slices of cells at once using either Bessel beams or dithered scanned beams [93]. This overcomes limitations in laser scanning speed and pinhole light rejection and is known to be fast and generate high signal-to-noise ratios (SNRs). A tradeoff between FoV and resolving power still occurs though, as the use of an identical set of detectors through one pair of identical objectives limits the scale of an FoV and resolution at high FoVs in the same way as other techniques.

Other techniques such as simultaneous fluorescence microscopy and atomic force microscopy (AFM), seek to visualize cell electrical activity using fluorescence microscopy while a landed nanoscopic probe monitors the mechanical state of the cell or even maps the topography and stiffness of cellular subregions [94]. This method holds promise for matching the scale difference between mechanical and electrical phenomena but does not allow for direct imaging of intracellular cytoskeletal dynamics due to the inability for a probe to enter a cell without rupturing the cell membrane.

The first study in this thesis highlights this need for multiscale-capable imaging tools, and associated multiscale image analysis techniques, which can appropriately investigate dynamics across these spatiotemporal scales and provide direct interrogation of electrical and mechanical coupling mechanisms and functional effects. Measurements on neuronal networks guided by asymmetric textures show that mechanical inputs can drive structural alignments that resemble those seen in cortical columns. However, structural alignment of processes does not lead to functional asymmetries, and it is not clear whether further electrical and mechanical

remodeling on small scales, or larger scale observations will be required to detect functional asymmetries. We then demonstrate multiscale-capable mechanical signal analysis techniques, noted as currently lacking in 2.2.3, applied to systems where cause and effect relations may span multiple scales.

Finally, this thesis introduces custom microscopy approaches that allow both small scale and large-scale observations to be performed simultaneously, both on cellular-to-tissue scales, and tissue-to-organ scales.

Chapter 3: Measuring Electrical and Mechanical Coupling in Neuronal Networks via Calcium Imaging and Superresolution Microscopy

This section has been adapted from the work "Scaffold Asymmetries Drive Neuronal Network Structural, but not Functional Asymmetries" by P. Alvarez, K. O'Neill, M.J. Hourwitz, Z. Bowen, J.T. Fourkas, and W. Losert

P. Alvarez designed the experiment, collected data, wrote, modified, and ran analysis, and wrote the manuscript. K. O'Neill dissected animals, plated cells, and contributed to the experimental design and manuscript. M.J. Hourwitz fabricated ridged polymer scaffolds. Z. Bowen designed functional analysis workflow.

Introduction

Many neuronal networks in the central and peripheral nervous system display distinct spatial structure reflecting their functional purpose. In the canonical example of the spine, axons spatially elongate, providing long "train track" style architectures along which information is transmitted to and received from the rest of the body [95]. Neurons in the sensory cortex form aligned units as well. Groups of neurons with similar receptive fields organize into functional columns. These functional columns represent process bundles across neuronal layers which are functionally correlated and contain long, aligned processes connecting groups of neurons between layers [96]. Since these aligned neuronal networks have proven to be vital to overall

function and processing in the central and peripheral nervous systems [97], researchers have sought to re-create these structured networks in-vitro.

Apart from aligning axons for peripheral nervous system regeneration, much focus has involved the recapitulation of the 3D layer structure of the sensory cortex to understand how sensations are processed and perceived by the brain [46, 98]. Various experimental models have been proposed for this purpose [99, 100], but proper network development involves both “spatial” network formation steps, in which growth cones are oriented and axons branch, and “functional” steps, in which synapses are formed and strengthened [101]. Both these spatial and functional formation steps need to occur to generate the requisite neuronal network morphology.

Typically, creating spatially ordered networks requires a continually applied mechanical or chemical stimulus [102-105]. Due to its ease of implementation, fabrication, and cell compatibility, researchers in neuroscience typically use cell scaffolds with defined patterns for this purpose [97, 102, 104, 106-109]. The scaffolds can be fabricated from commonly available FDA-approved biocompatible materials, such as polydimethyl siloxane (PDMS), polylactic acid (PLA), biodegradable hydrogels, or polycaprolactone (PCL) [97, 102, 104, 106-109].

Patterned scaffolds that have been studied for guiding neuronal network formation include nanopillars [110, 111], electrospun nanowires [112, 113], randomly imprinted scaffold topographies [113, 114], and patterned microgrooves [56, 110, 111, 114-116]. Each of these patterns has independently been shown to increase markers of neuronal health and substrate attachment, as well as guide individual neurite outgrowth [113]. The former effect, increased neuronal health and upregulated

attachment, has been studied extensively. Proliferation ratio in neural stem cells and outgrowth in primary neurons are heavily correlated to certain material properties, including stiffness, roughness, and alignment [108]. These properties are also related to differentiation fate in neuronal stem cells [104, 108]. The second effect, the guidance of neurite outgrowth, is of particular importance for recapitulating sensory cortex layer structure. Prior studies have shown alignment of 2D cellular polarity and neuron/axon outgrowth due to patterned microgrooves in extracted neurons and neuronal stem cells [117-119]. Other work has also leveraged the process guidance effects of patterned scaffolds, in conjunction with micro-electrode arrays, to probe changes in internal neuronal dynamics in response to network structuring [112, 113]. Regenerative medicine researchers have also leveraged these effects using chemically activated neural stem cells to ensure neurite outgrowth is directed towards sites of injury, to repair severed neuronal connections [97, 120-122].

The same mechanical stimuli that guide processes can also provide cues that modulate the strength of network connectivity, i.e., functional cues. These functional cues may be provided by a connection between the cytoskeleton, a key sensor of the mechanical cellular environment, and the pathways that regulate ion flows and electrical signaling in cells [123-126]. This link between the cytoskeleton and electrical activity in cells is typically attributed to the anchoring of ion channels to the cytoskeleton and modulation of activity of Na+/K+-ATPase enzymes by actin in neurons [8, 75]. Cytoskeletal-binding proteins have also been shown to be a key signaling factor in the process of long-term potentiation, which involves persistent strengthening of synapses and is a main driver of neuronal network plasticity [83].

Given these links between the cytoskeleton and protein dynamics related to electrical transmission, mechanical stimulation in the form of scaffold-derived cues may affect both physical and functional networks simultaneously. The expected effects of scaffold-derived spatial cues on functional networks has also been simulated in-silico [127]. However, network-level spatial and functional effects, especially regarding single-cell level process alignment and activity correlation strength, are not well studied.

Here, we introduce a study aimed to address this gap. Using embryonic rat cortical neurons, we study the development of a structural and functional neuronal network that is driven by ridged PCL scaffolds. Embryonic rat cortical neurons provide a robust platform for studying effects decoupled from differentiation; while the neurons exhibit high plasticity and are known to develop complex neuronal networks in-vitro, their identity and fate are tightly controlled [32, 128]. We image spatial networks using 3-D Airyscan microscopy at super-resolution (up to 120nm laterally, 350nm axially). Alignments of structures are then analyzed via Laplacian of Gaussian (LoG) filtering, giving alignment information along each process segment. We also image functional networks using fluorescent calcium imaging, a popular technique for visualizing individual neuronal activity. Correlation networks derived from calcium imaging are commonly used as a metric for functional connectivity in-vitro and are analogous to so-called noise correlations between neurons in-vivo [129, 130].

Methods

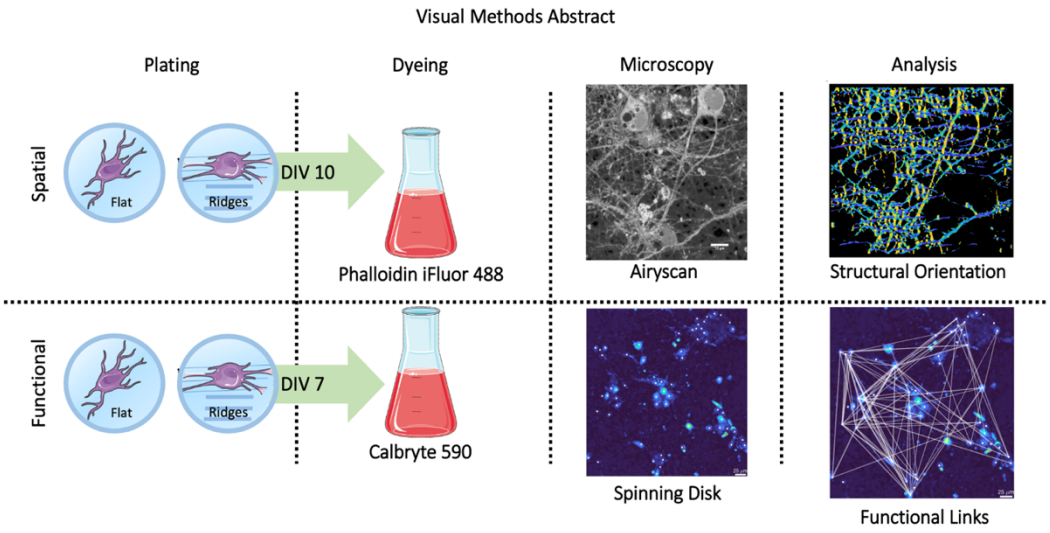

Figure 7: Visual methods abstract showing experimental workflow.

Fig. 7 provides a visual reference to the general workflow of the methods described in this section, which yield the structural orientations and functional metrics used for comparison between conditions.

Primary Neuron Cell Culture

Primary cortical neurons were obtained from Sprague Dawley rats at embryonic day of gestation 18 (E18) as previously described [131]. Briefly, timed pregnant female rats were euthanized via CO_2 asphyxiation, and embryos were removed by Cesarian section. Embryos were decapitated, meninges removed, and both the hippocampi and cortices were isolated from each cerebral hemisphere. Cortices were mechanically dissociated through a fire-polished Pasteur pipette, counted using a hemocytometer, and plated at the appropriate amount. All dissections were performed in concordance with the recommendations of and approval by the

University of Maryland (UMD) Institutional Animal Care and Use Committee (IACUC; protocols R-JAN-18-05 and R-FEB-21-04).

Neurons are plated on 1.6μm or 3.2μm-pitch ridged scaffolds, 1μm in height, fabricated from either PCL or a proprietary acrylate compound. All 1.6μm pitch ridges were fabricated from acrylate, and almost all 3.2μm pitch ridges were fabricated from PCL. This mismatch in substrate material was due to supply limitations incurred during the course of this experiment. A direct comparison of the ridge materials can be seen in Fig. 8. No notable difference was observed. The ridge size and pitches were chosen because they are both significantly shorter than the cell body and smaller in pitch than a typical growth cone, thus allowing for mechanotransduction without physical confinement. To promote long-term neuronal adhesion, glass dishes (the control) and ridged scaffolds were coated with 0.1 mg/ml poly-D-lysine (PDL; cat. no. P0899, Sigma-Aldrich) in borate buffer (pH 8.5) for at least 1 hour at 37 C, washed three times with sterile dH_2O, and coated with 10μg/ml laminin (cat. no. L2020, Sigma Aldrich) in media for at least 1 hour at 37 C. For control scaffolds, 35mm dishes with a 20mm glass center were used (cat. no. P35G-1.0-20-C, Mattek). The same dishes were used for ridged scaffolds, with the original glass removed and custom scaffolds glued after coating. For functional imaging, primary cortical neurons are plated at densities of 520 cells/mm^2 on both control and ridged scaffolds (corresponding to 5 x 10^5 cells/dish). For structural imaging, primary cortical neurons are plated at densities of 260-520 cells/mm^2 on both control and ridged scaffolds (corresponding to 2.5-5 x 10^5 cells/dish). After plating, neurons are allowed to mature for 7-10 days in vitro (7-10 DIV) in NbActiv4 growth media (cat.

no. N4, TransnetYX Tissue) at 37 C in a humidified 5% CO_2 environment to form a complex network. Half media is replaced every 3-4 days to ensure cell health while also preventing large fluctuations in media pH.

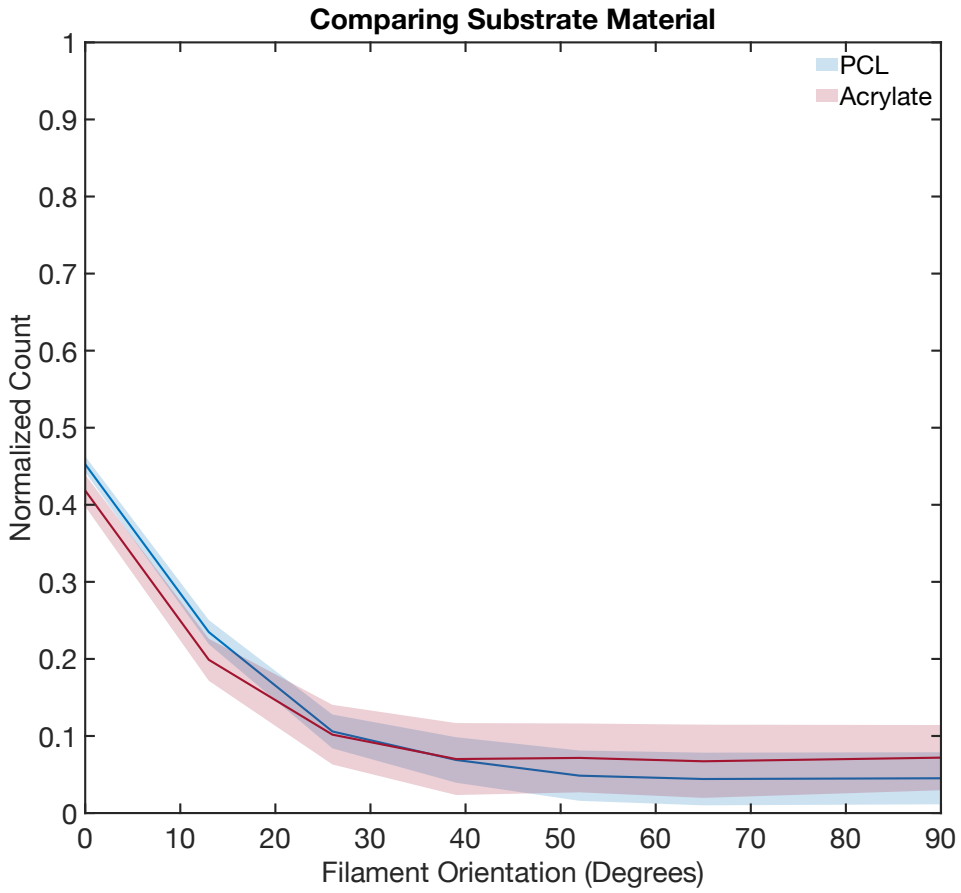

Figure 8: Sample comparing differences in alignment strength between 3.2μm pitch ridges of fabricated from PCL and acrylate.

Live Calcium Imaging

On DIV 7, the neurons are incubated with 1.5 μg/mL Calbryte-590 calcium dye for 1 hour. Calbryte-590 was chosen for its photostability and long residence time in the cytosol.

To image the resulting functional neuronal network, cells are placed on a Perkin-Elmer spinning disk confocal microscope, and 3 or more random locations per sample, each location containing a minimum of 40 active neurons, are found. Each of these locations are imaged for 5 minutes. The process is repeated for both flat and ridged scaffolds.

Superresolution Imaging

On DIV 10, a separate sample of cells is fixed via paraformaldehyde 4%, which provides fixation, and is then permeabilized with Triton X-100. Phalloidin-iFluor 488 stain is diluted in PBS 1:100 and incubated with cells for 1 hour at room temperature. This label allows us to determine the spatial structure of the neuronal network by labeling all processes homogenously.

For all fixed cell studies, we relied on 3D superresolution imaging provided by a Zeiss Airyscan 980. In addition to providing up to 120nm lateral resolution imaging of terminal dendrites, the superresolution system allows us to study the structure of the network along the z-axis, including processes with small gaps between them.

Each z-slice, separated by 350nm, was analyzed independently using LoG filter analysis. Additionally, vertical contact points were qualitatively observed to determine the existence of separated network layers with discrete contact points.

Deconvolution of Airyscan images was performed in Zeiss Zen 2.0 software to achieve 120 nm spatial resolution in the XY plane, and 350nm in Z, small enough to visualize even the finest terminal dendritic branches in our system. At least 5 FOVs are imaged from at least 3 separate dissections for each condition.

Results

LoG Analysis in the Fourier Plane

To measure the alignment of processes throughout mature neuronal networks at different ages and plating densities, we adapted an algorithm from our previous studies which leverages the edge enhancement properties of Laplacian of Gaussian (LoG) filters to determine the preferred orientation of filamentous structures in images [15, 132]. Briefly, this algorithm takes as input a 2D biological image with filamentous structures such as developed neuronal monolayers (Fig. 9A, as an example), then first creates an array of 2-dimensional LoG filters of a predetermined width, comparable to the fibers of interest, oriented from 0 to 180º at a specified angular resolution (this study uses angular increments of 2º). Examples of LoG filters can be seen in Fig. 9B. The image of processes and the filter array are then both Fourier transformed and convolved in the Fourier plane to create an image stack showing various levels of intensity enhancement of each fiber due to particular filter rotations. This Fourier plane convolution avoids "locking" of the filter on pixel edges in the original image. The convolved images are then inverse Fourier transformed, and the preferred orientation of each pixel is found in the image stack. The image is then masked using a binarized version (threshold determined as three standard

deviations below the mean intensity of the image) of the original image to reduce spurious angular noise from background pixels. An example of a resultant orientation image is shown in Fig. 9C below. A polar histogram showing the resultant angle distribution is seen in Fig. 9D. Of note in Fig. 9C is the effect of non-fibril features, which typically show “enhancement” at every orientation. As such, these features add a small level of uniform background noise.

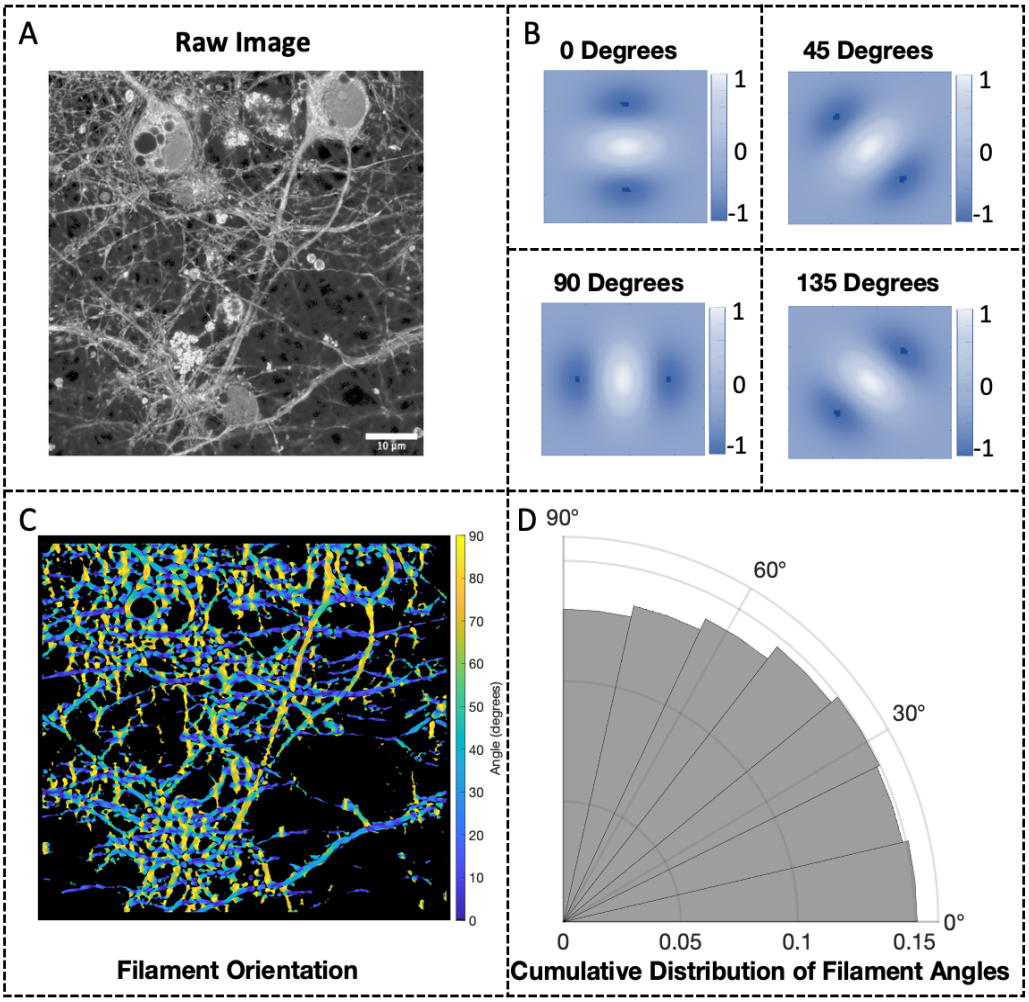

Figure 9: Image showing LoG analysis workflow. A) Raw image showing neuronal filaments on a flat surface propagating at a variety of angles. B) LoG filter in a selection of orientations. C) Image showing angles of all filaments in image shown in A. D) Polar histogram of preferred angles demonstrating no noticeable bias in direction of ridges. Steps are labelled chronologically as applied.

Local Analysis of Process Alignment Reveals Consistent Guidance and Signaling Competition

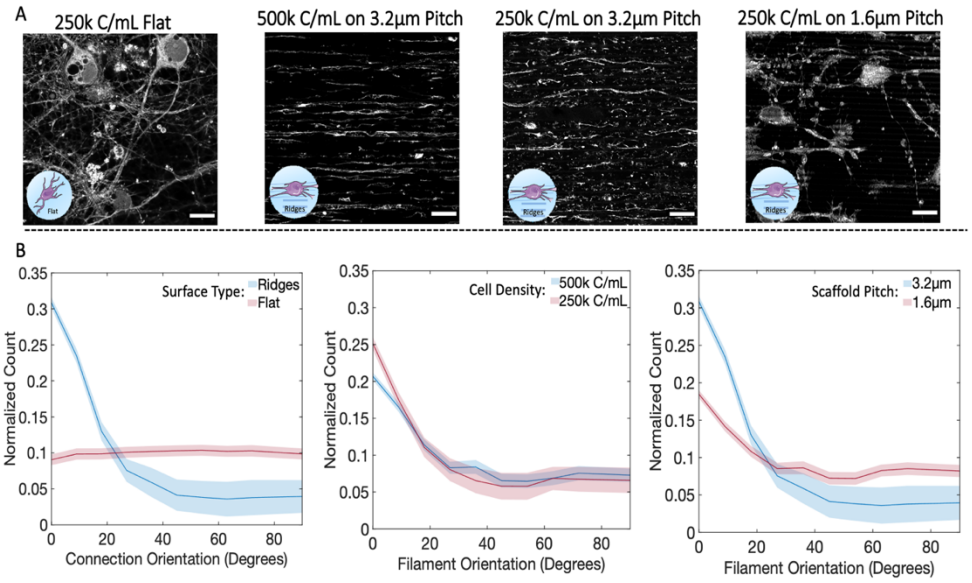

Figure 10: A) Images showing representative phenotypes of tested culture conditions. B) Histograms showing distribution of angles found through LoG analysis. From left to right: 3.2µm ridged scaffolds (n=6) vs. flat (n=5) scaffolds, low density cell seeding (n=3) vs. high density (n=3) on 3.2µm ridged scaffolds, and 3.2µm ridged scaffolds (n=6) vs. similar scaffolds of half pitch width (n=3). All distributions are normalized such that the sum of their heights is 1 (probability normalization). Error bars represent three standard errors of the distribution. For the ridged scaffolds, an angle of 0 indicates alignment with the ridges, while 90 represents anti-alignment. All images taken ~170nm away from the coverslip. Scale bars represent 10µm.

As noted above prior studies have already shown the ability of micro-grooved cell scaffolds to align individual processes and exert alignment forces on excised tissue. Not well studied, however, are the spatial effects of these scaffolds network-wide on an individual process level. We implemented the outlined analysis method to

investigate the alignment of individual processes on our ridged scaffolds in fixed samples with both varied densities and varied ridge spacings.

Fig. 10A shows examples of neurons plated on ridged and flat scaffolds. Neurons plated on ridged scaffolds displayed both strong guidance and long persistence in process outgrowth. Processes were able to extend over hundreds of microns with little deviation from the underlying topography, especially in low density samples. Cells morphologically looked otherwise normal and healthy, indicating general biocompatibility with PCL-based ridged scaffolds over the course of the experimental timeline.

After applying LoG analysis to the different densities of cells grown on flat and ridges substrates, quantitative results mirrored observational findings and showed clear evidence of guidance of processes on ridged scaffolds, demonstrated in Fig. 10B (left). Processes, in both low- and high-density samples, show preference for growth along the ridges. In contrast, as expected, processes grown on flat scaffolds had random growth directions. We also observed that cells plated on ridged scaffolds achieved a decreased strength of guidance in higher density samples (Fig 10B, middle). A decrease was also seen on scaffolds with narrower ridge pitch (Fig. 10B, right).

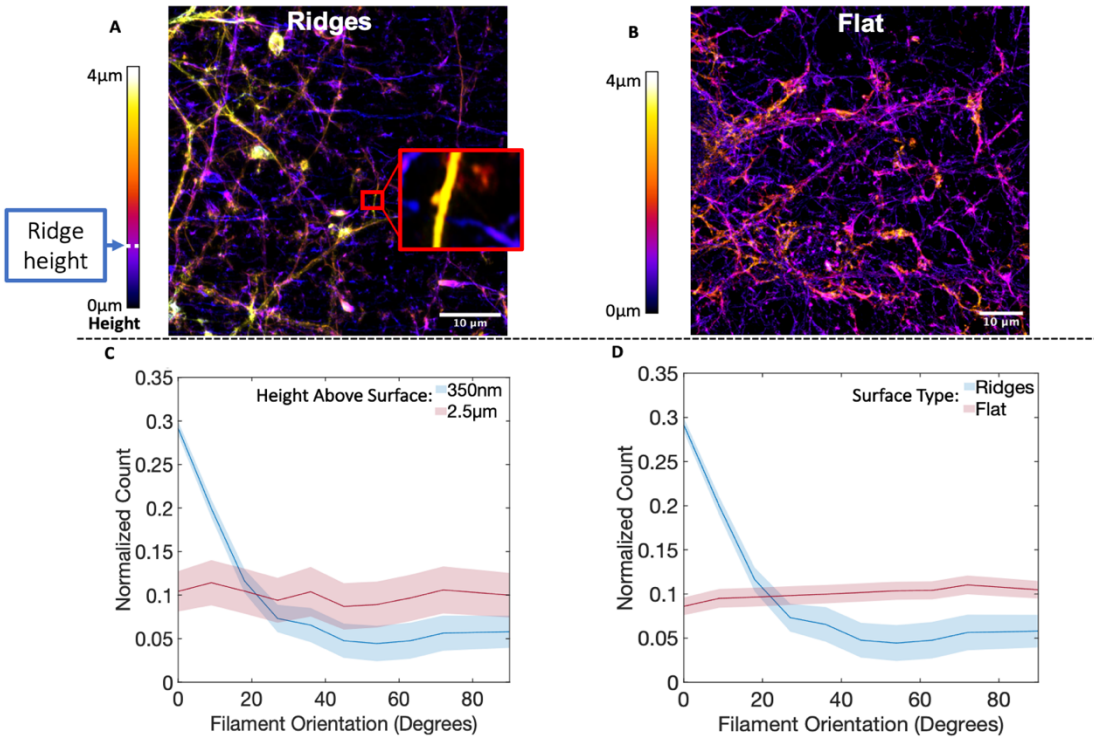

Figure 11: A) Representative dataset showing processes at different heights above the coverslip. Orange arrows represent ridge direction. Processes proximal to the coverslip surface visually appear aligned, while processes distal from the coverslip appear randomly oriented. Red insert shows higher-level process appearing to pass over lower-level processes without contact. B) Similar plot showing 3D profile of processes on flat surface. C) Linear plot quantifying the drop off in alignment above the coverslip. Aggregated data from multiple samples shows a rapid drop-off in alignment from 350nm to 2.5µm away from the coverslip. D) Direct comparison of the alignment of neurites 350nm above the coverslip on ridged vs. flat scaffolds. Error bars represent three standard errors of the distribution.

In addition to alignment along ridged scaffolds, such scaffolds also yield height-dependent effects. Though previous studies have only focused on 2D alignment on ridged substrates, ridges of a sufficient height (> 1µm) provide an opportunity for processes to pass over one another without contact. This effect may allow for a 3D network architecture, with layers possessing different topologies, due to layers

experiencing differing levels of guidance, cytoskeletal activity, and even synapse formation caused by changes in process intersection points where synapses are formed.

Fig. 11A shows an example of the 3D network architecture we found to be evoked by a ridged scaffold. In the ridge image, qualitatively, processes close to the coverslip are clearly aligned and show a strong preferential direction. This alignment progressively diminishes farther away from the coverslip and has entirely disappeared by approximately 2-3μm away from the coverslip. Evidence can also be seen in Fig. 11A of process branches with no strong lower layer components, almost entirely existing within the upper region away from the scaffold for most of the field of view. Highlighted in red are areas where upper layer processes are seen crossing coverslip-adjacent processes, hinting at the existence of multiple discrete process layers with spatially separated contact points. The flat counterpart, seen in Fig. 11B, displays a homogenously dense mesh network in the areas close to the coverslip, with the density falling off with height. In contrast to the ridged image, we observe that the upper layers and lower layers display a similar lack of directional preference for processes.

In Fig. 11C we quantify this height-based alignment dependence. Strong guidance is seen close to the coverslip, at 350nm, but is no longer present at 2.5μm away from the coverslip (or 1.5μm above the peaks of the ridge structure).

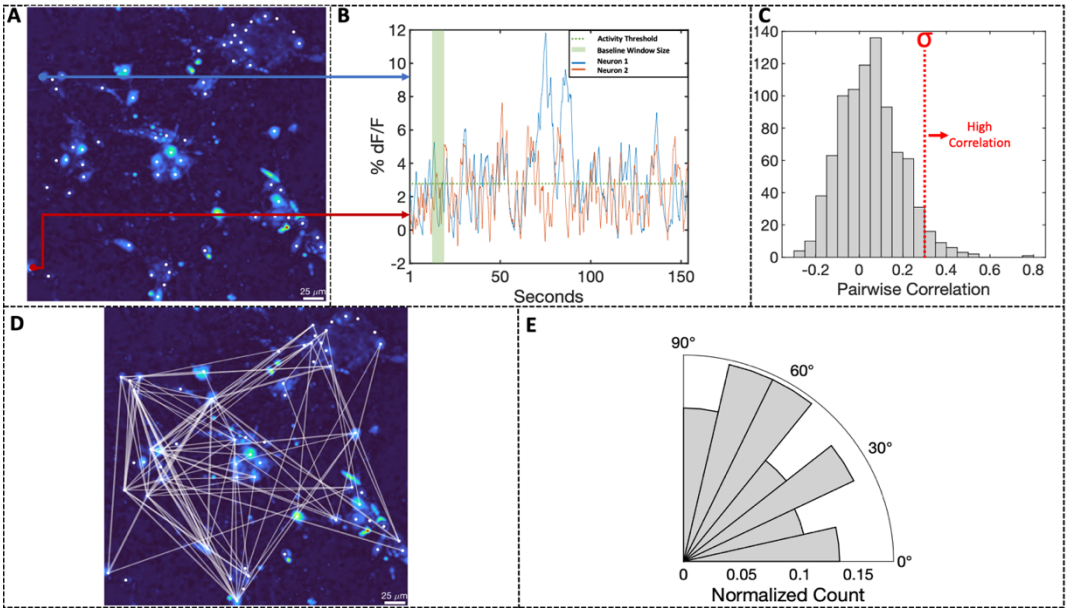

Figure 12: Experimental workflow of functional analysis, visually represented. Steps flow left to right, top to bottom. First, neurons are identified, and fluorescence is averaged in space from a circle around the center of each neuron. Standard deviation projection shown for representation. (A). Fluorescence traces are then extracted (B). Traces here are colored respective to the selection circle around each neuron. Neurons that have no peaks, determined through deviation from baseline (green, solid), in activity below a specified threshold (green, dashed) are considered inactive. All traces are pairwise correlated to each other, and a correlation distribution is created (C). For functional network formation, only positive correlations greater than one standard deviation greater than the mean are considered. Image shows resulting functional network overlaid with standard deviation projection. Line widths between nodes are scaled by relative correlation strength (D). The angle and distance of these pairwise connections are then calculated and compared between conditions (E).

As previously discussed, network-scale functional effects of ridged scaffolds on neuronal networks are not well understood due to the focus on morphological changes and internal dynamics in previous studies [97, 113, 117, 133]. Therefore, to

provide a more holistic view of how ridged scaffolds shape network development, we also examined functional effects using the established paradigm of calcium imaging and analysis via correlation networks. Because we want to measure spatiotemporal biases in addition to more traditional metrics of correlation strength, we developed a modified method which also analyzes the preferred directionality of high correlation pairwise functional connections.

Fluorescence extraction

Neurons were identified manually from the time-averaged image of the motion-corrected image sequence. Circular regions of interest (ROI) with radii of 10 pixels were drawn on cells identified via manual selection. Overlapping ROI pixels (due to closely juxtaposed cells) were excluded from analysis. For each selected neuron, a bleach-corrected fluorescence signal over time (F) was extracted by averaging across pixels from the ROI overlying the soma. The raw fluorescence for each neuron was then converted to a relative fluorescence amplitude ($\Delta F/F_0$), where $\Delta F = (F - F_0)$. F_0 was estimated by using a sliding window that calculated the average fluorescence of points less than the 50^{th} percentile during the previous 6-second window (chosen as approximately twice the FWHM of an entire calcium transient in our dataset). Fig. 12A, B highlights this step of the process.

Pairwise correlations

To assess the functional similarity of neurons, we computed correlations based on the covariance of their activity over time. Pairwise correlations were

obtained for each neuronal pair by calculating the correlation coefficient of their $\Delta F/F_0$ utilizing MATLAB's "corrcoef" function, which performs the following:

$$\rho(A,B) = \frac{1}{N-1}\sum_{i=1}^{N}\left(\frac{A_i - \mu_A}{\sigma_A}\right)\left(\frac{B_i - \mu_B}{\sigma_B}\right)$$

where A and B represent the $\Delta F/F_0$ of each neuron at frame i out of N acquired imaging frames and where μ and σ represent the mean and standard deviation of $\Delta F/F_0$ over all frames. Pairwise correlations and pairwise distances between neurons are recorded and compared between all active neuron pairs. Neurons that did not display transient peaks in fluorescence signal above a threshold, set to approximately the full width at half maximum of the largest such event in the dimmest active neuron, are not considered. Fig. 12B shows this thresholding effect and Fig. 12C shows an example resulting correlation distribution, and Fig. 12D shows all high-correlation network pairs overlaid with the mean image of the underlying dataset.

Functional networks and spatial connectivity

Functional networks are constructed by considering all pairwise correlations between neurons and then pruning them in two separate applications via thresholding. The thresholding method prunes all connections below the chosen threshold amount. Thresholds are chosen based on the standard deviation of correlation strength. The first threshold used in this study is one standard deviation above the mean correlation strength, such that only neurons with high correlations are considered. An additional threshold is also placed on the dataset, in which neurons that fire more than 3

standard deviations above the mean firing frequency of the neurons in the FOV are discarded. These hyperactive neurons are known to be drivers of the neuronal network but, in a sample of the activity of 10s of neurons, would dominate the network such that only connections between them and other neurons are analyzed. Angles between these non-hyperactive neurons are then calculated for each connected neuron pair to analyze the angle of the connection with respect to the alignment of the substrate. These angles are then rotated to align with the ridges, with 0 degrees the representing an angle parallel to the ridges and 90 degrees representing an angle fully perpendicular, and then aggregated and binned into histograms. Fig. 12E shows one such histogram derived from the network shown in Fig. 12A.

Ridged Scaffolds Reduce Overall Correlations in Cultured Neuronal Networks

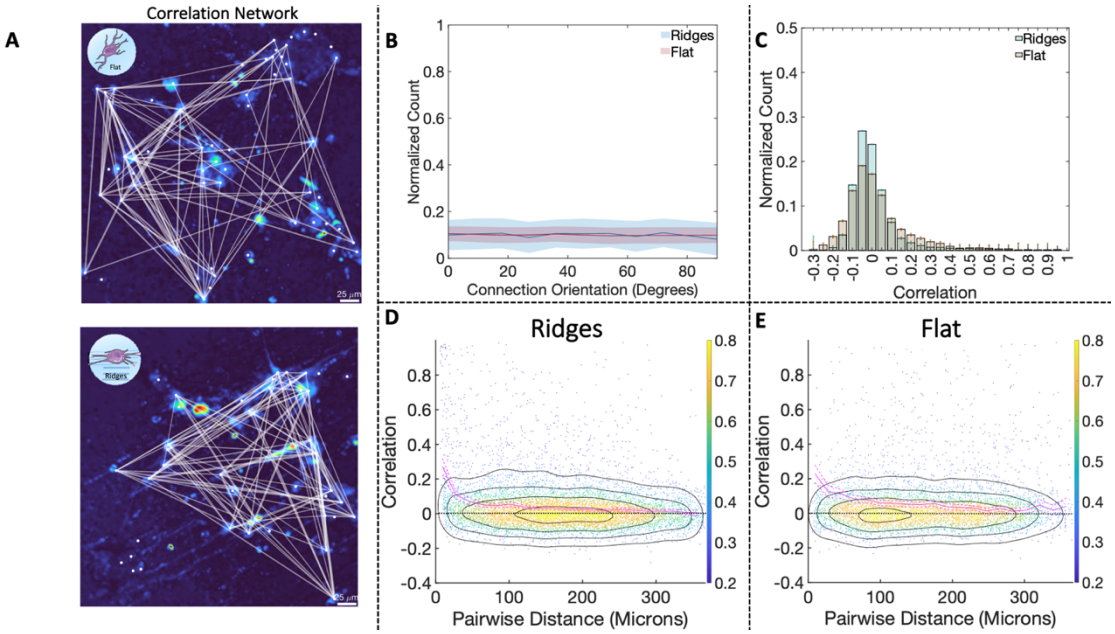

Figure 13: Functional comparisons of neurons on aligned surfaces vs. flat surfaces. A: Standard deviation projections showing example fields of view (FoVs) with associated pairwise high-correlation links on flat and aligned surfaces. Line widths between nodes are scaled by relative correlation strength. B: Distribution of connection angles (w.r.t. ridge direction, for aligned surfaces) for all pairwise connections. Error margin represents 1 standard error. C: Distribution of correlations for flat and aligned surfaces. Error bars represent 3

standard errors of distribution. D-E: Scatter-cloud plots showing pairwise correlation vs. pairwise distance for all pairwise connections on aligned vs. flat surfaces.

After applying this technique for measuring correlations and spatial biases to our data, we observe a lack of preference for ridge-oriented correlations in spatial patterns of neuronal functional connectivity. Fig. 13A shows example images and correlation networks for both experimental conditions, flat scaffold and ridged scaffold. Fig. 13B demonstrates this lack of preference after DIV 7 in high-correlation functional connections.

Fig. 13C shows correlation distributions for networks cultured on ridged and flat scaffolds. Notably, overall correlations for ridged scaffolds were lower than their flat counterparts, both positive and negative. Fig. 13D-E shows another effect of these scaffolds. Although the average correlation drops more quickly over distance in ridged samples than flat samples, there is a mildly increased number of mid-length pairwise distances spanning approximately half the length of the FOV (~175 μm). This increase may be explained by increased neuronal aggregation, likely induced by the stiffness of the PCL substrates (see Fig. 13A and Fig. 14) [134]. Increased aggregation was seen with samples plated on both flat PCL, and even further aggregation was observed when ridged scaffolds were added. Given that we attempted to maximize the number of neurons in each FoV, this aggregation-inducing effect resulted in approximately 3-4 neuronal aggregates in each data set. By configuration, 3-4 neuronal aggregates fit inside each field of view roughly in quadrilateral or triangular patterns, both resulting in a high number of diagonal connections. Coated glass scaffolds displayed little aggregation, in contrast. Overall,

this result indicates that ridges do not seem to automatically upregulate correlations between neurons in the direction of ridges. Therefore, in the context of this study, it does not seem that ridged scaffolds create desired functional structure in addition to spatial structure in neuronal networks.

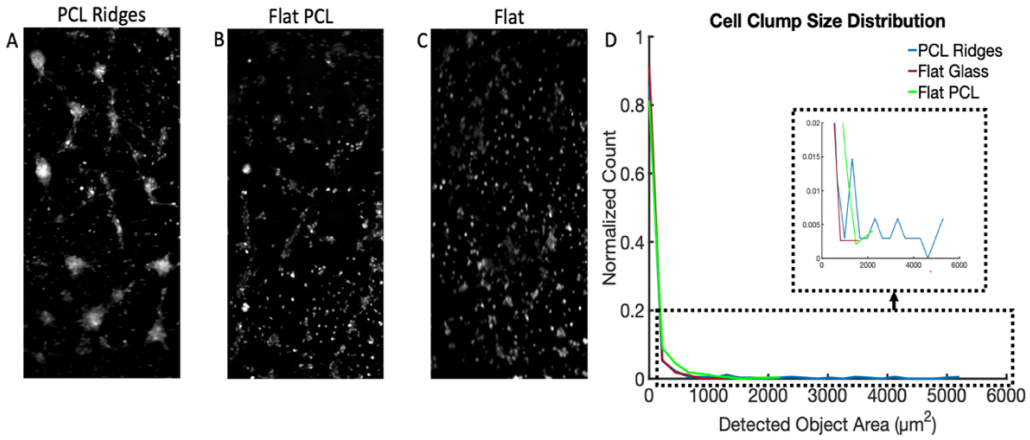

Figure 14: Quantification of aggregation differences observed on various surface types. A-C: Images of aggregates on ridged PCL, flat PCL, and flat glass surfaces. D: Normalized distributions of detected aggregate sizes after binarization and segmentation on each surface type.

Discussion

Patterned scaffolds offer a promising method of guiding neurite outgrowth, creating patterned neuronal networks, and simulating complex neuronal functional groups in-vitro. They have been shown in both this study and previous studies to reliably align processes with underlying scaffold topography over long distances, and they can be manufactured not only from biocompatible materials but also from biodegradable materials, as in this work [135-137].

In our study, we observed distinct guidance of processes in higher density culture conditions than previously reported (Fig. 10). This demonstrates that even in an environment with a high number of neighboring neurons, mechanotransduction of scaffold texture can be achieved during growth. In these high-density samples, however, there was a noted decreased strength of guidance (Fig. 10B). This could be explained by mechanical signals in neuronal networks experiencing competition from chemical and electrical signals emitted by neighboring neurons during development. We expect that this competition increases with a greater cell density due to the increase in the number of neighboring neurons. Due to this density dependence, one may expect the existence of a threshold where competition from other signaling factors overwhelms guidance effects provided by scaffold texture. Locations with very high neuronal densities may not generate structured networks.

In our study, we also found that 1.6μm ridge spacings provided poorer guidance compared to 3.2μm ridge spacings (Fig. 10B). This could be because of reduced confinement of growth cones and their internal signaling processes during neurite extension from the soma. Both of these spacings are within the range of pitches reported to induce guidance effects. Previous studies have found that suitable ridge spacings are between 1 and 10μm in pitch [97, 117, 135, 136]. However, the optimum pitch within this range is likely dependent on neuron type, and therefore our specific result of 3.2μm ridge spacings being more optimal than 1.6μm ridge spacings for guidance may only be true for the studied rat cortical neurons. We also found a dependence on height away from the surface for spatial alignment (Fig. 11C, D). The strong guidance dichotomy between coverslip-proximal and coverslip-distal

processes suggests a multi-layered network, where upper layers of processes, crossing multiple ridge peaks while occasionally dipping into valleys, experience very little guidance (if at all) and reflect a typical disordered network seen on flat scaffolds. Lower layers, sitting almost entirely within ridge valleys, experience mechanical guidance and have process structure that runs parallel to the ridge direction. These layers may communicate with each other at discrete contact points and therefore can influence the others' intralayer dynamics. Somas themselves are much larger than the ridges and therefore do not reflect this layered phenotype, though this layered synapse structure could create unique perturbations to the overall functional network topology.

Previous work in this field has been primarily morphologically focused and has only addressed spatial patterning of neuronal networks or changes to functional dynamics on an individual neuron/neuronal cluster level [97, 113, 117, 133]. Few studies have attempted to address both the spatial and functional aspects of neuronal network formation. We found in our study that there was no clear spatial bias for high correlation pairwise connections, and that correlations dropped overall in the neuronal network grown on ridged scaffolds (Fig. 13). This result is consistent with prior observations of the vertically varying nature of the ridged spatial network, i.e., reduced contact points due to the ability of neurites to transit over each other without contact (Fig. 11). Additionally, neurites may have a longer persistence length in the direction of the ridges during growth and therefore may travel longer distances before encountering other neurites during development. Reduced correlations may also indicate that non-Hebbian modes of plasticity are more prominent in a mechanically

dominated network formation regime. Another possibility is that scaffold stiffness itself may down-regulate synaptic strength, an effect that would require follow-up study to untangle.

Importantly, our results indicate a decoupling of spatial connectivity from functional connectivity, as neuronal networks as grown in our work show structural alignment yet are functionally not aligned. The immediate implication of this decoupling is a potential need for a secondary training mechanism which can provide asymmetric functional cues to the network. Some examples of this could include optogenetic stimulation, local electrical stimulation, or asymmetric global electric fields. Spatially structured networks may also benefit from more persistent results from training regimens from their randomly oriented counterparts, due to weaker coupling between processes and a higher energy barrier to synapse formation resulting from the spatial separation of processes.

However, our results indicate that further work using more complex analysis and experimental techniques may reveal more information. Neurons respond to cumulative inputs from many neighbors and produce distinct firing patterns in response to structured stimuli. Correlations as studied in this work are analogous to noise correlations in-vivo, and therefore may require analysis techniques which go beyond pairwise correlations or visualize directed metrics of information flow to expose network asymmetries. The structured stimuli response may also be revealed by optogenetics, in a similar method as previously suggested.

Imaging of larger fields of view also has the potential to reveal more functional network characteristics from our experimental platform. Already, both theoretical and experimental work has been published indicating that collective metrics, such as characteristic correlation length and critical point, depend heavily on the size of imaged fields of view [44, 45]. These results suggest that differences in collective metrics may appear similar in local windows. Traditional in-vitro FoV sizes of <1mm, as used in this study, may limit the ability of analytical techniques to assess the differences in metrics caused by mechanical perturbations. Larger FoVs may provide different results, especially in the case of parallel ridges, which cause long, straight processes and are therefore likely to alter long-range communication (and therefore long-range correlations) between neuronal clusters.

In addition to improving metrics of functional network alignment, we encourage future studies to directly image the interplay between cytoskeletal modulation and neuronal networks. Decreased overall correlations, like those found in this work, have also been found to result from arresting actin polymerization in neural cell networks [126]. Due to its importance as the primary mediator of mechanical stimuli, the decreased correlations found in this work could also indicate an underlying change in actin polymerization dynamics causing functional effects in neuronal networks grown on ridged scaffolds.

Spatial networks could also show not just static effects, but dynamic effects of cytoskeletal modulation, particularly in actin, the most dynamic cytoskeletal protein [51]. Neuronal network growth requires significant internal coordination between the cytoskeleton and the surrounding cellular environment to realize synaptogenesis,

migration, generation of processes, cell polarity, and neurite migration [50, 138, 139]. Network formation in neuronal cultures is realized through the extension of actin-rich neurites, which result in a complex web of synaptic connections between the axon of a single neuron and several dendrites extended from many neurons. Axons in particular have been demonstrated to have rich actin-based dynamics governing their outgrowth on patterned scaffolds [74, 140]. Both the neurites themselves and the neurons from which they originate also rely on actin-rich focal adhesions to interact with their surrounding environment [47, 118, 141, 142]. In vivo, this surrounding environment is often represented by perineuronal nets, a complex matrix of multiple proteins heavily involved in regulation of network plasticity [48, 49]. Imaging these various actin dynamics, both during development and directly during calcium imaging, would provide another metric of connectivity between cells and highlight modulated physical intracellular connections.

Other scaffold patterns used in previous work by our lab, such as sawteeth and nanopillars of varying sizes, could also provide controlled, pre-defined topological perturbations specific to research or clinical needs and reflect the varying network topologies seen in the nervous system, potentially within the same culture dish [58]. This ability to provide multiple topologies in the same dish could occur with multiple adjacent patterns, or through the 3D effects we have potentially uncovered in this study. These 3D network structures could mimic topologies such as the organizational disparity between the tonally structured layer 4 of the murine auditory cortex, juxtaposed with its more randomly patterned layer 2/3 just above [143].

Conclusion

In this paper we have studied the network-scale effects of ridged scaffolds on embryonic rat cortical neurons. We found that ridged scaffolds of multiple pitch sizes robustly aligned neurons plated at multiple densities. We found that pitch size influenced the strength of this alignment effect, as did plating density. We also found that processes were able to form complex, height-varying networks even though neuronal bodies existed in a monolayer on the dish scaffold. Finally, we found that functional networks, counter to theoretical predictions, did not display any similar preferential alignment in high correlation connections, indicating a decoupling between the spatial and functional networks. Correlations were also reduced overall. This lack of observed effect prompts the need for further studies involving secondary training beyond patterned scaffolds, newer imaging techniques, and imaging on larger spatial scales which can span the entire length of multiple processes. If functional alignment and control is achieved, the general system described here, of networks grown on patterned scaffolds and imaged optically using calcium imaging techniques, could be applied not only to study the effects of these scaffolds for peripheral nervous system regeneration, but also to mimic and study the structure of other spatially ordered networks in the brain.

Chapter 4: Optical Measurements of Mechanical Dynamics Across Multiple Scales

As highlighted in the previous chapter, understanding electrical and mechanical interactions often requires measurements across dramatically different scales to capture the full extent of the effects of one system on the other. In that study, actin alignment on a small scale likely led to alignment of whole processes, but the functional effects on a full network scale were difficult to discern without full network imaging. This challenge of measurement across scales has been highlighted as well in other electrical and mechanical studies completed during this dissertation, including those on individual cells, cell networks, and whole organs. In this chapter, we introduce a mechanical analysis technique which is capable of multiscale measurement. This is a key enabling technology for our future work which seeks to investigate not only electrical and mechanical coupling on the nanometer-to-micron scale, but also electrical and mechanical bulk functional effects on the tissue and organ scale. I showcase two studies that highlight its use, first in tracking actin polymerization inside cells and cell migration, and next in tracking the mechanical responses of neurotransmitter exposure in a whole dissected organ via muscle contraction.

Using Optical Imaging to Track Intracellular Actin Events

The first highlighted study in this section introduces a multiscale-capable analysis algorithm derived from optical flow, a method adapted from computer vision to track

dynamic events in real-time. In this study, this algorithm was used to track actin polymerization events in multiple cell types on ridged scaffolds, similar to those used in Chapter 2.

This section has been adapted from the work "Quantifying topography-guided actin dynamics across scales using optical flow" by R.M. Lee, L. Campanello*, M.J. Hourwitz, P. Alvarez, A. Omidvar, J.T. Fourkas, and W. Losert. Mol Biol Cell, 2020. 31(16): p. 1753-1764.*

R.M. Lee and L. Campanello designed the experiment, wrote the manuscript, and performed analysis. M.J. Hourwitz fabricated nanotopographical surfaces. P. Alvarez and A. Omidvar collected optical data in MCF10A cells and HL-60 cells, respectively. Below are sections focused on my contributions and commentaries on the remainder of the manuscript indicated as [… ...] .

Introduction

Understanding the rearrangements of the cytoskeleton is essential to developing a complete picture of the dynamic forces involved in cellular processes such as migration, division, and differentiation. Cytoskeletal dynamics, and in particular actin dynamics, have been shown to be important for the growth of cell junctions and focal adhesions [144] and for immune-cell activation. The formation of actin waves through directional polymerization and depolymerization of filaments drives many types of cell migration [145] and has been associated with the establishment of polarity in a variety of cell types [146]. Forces from the extracellular

environment are an important modulator of actin dynamics. Physical and chemical characteristics of the extracellular environment, such as rigidity, biochemical composition, and topography, have been shown to influence actin dynamics and associated cell behavior [147-150]. One mechanism for this modulation is mechanosensing via focal adhesions [151]. In addition, actin waves respond when cells encounter obstacles [73]. It has been established that ridges of width comparable to fibers in the extracellular matrix (ECM) can alter actin dynamics significantly [56, 57, 151] and bias the localization of focal adhesions [152]. Thus, in vivo, the topography of the ECM, such as collagen networks [153, 154], is likely to modulate actin dynamics. Periodic nanotopographic surfaces provide the opportunity to obtain systematic data on the modulation of such intracellular dynamics. In prior work, we have shown that actin waves can be nucleated near, and guided along, periodic nanotopography, in a phenomenon termed esotaxis. Actin-wave guidance has been observed in cell types that exhibit distinct physiological functions and migration phenotypes, including Dictyostelium Discoidium [56, 57], neutrophil-like HL60 cells [57], B cells [151], and breast cancer cell lines [58]. However, there are clear differences in the responses of each of these cell types to nanotopography. For example, although both D. Discoidium and HL60 cells exhibit esotaxis, these two types of cells have been found to move preferentially in different directions on specific nanoscale asymmetric sawtooth textures [57]. Furthermore, different breast cancer cell lines preferentially move in different directions on asymmetric sawtooth nanotopography [58]. Here we introduce a method for performing quantitative measurements of the influence of nanotopography on intracellular dynamics at both

the submicron and the micron scales. This approach enables the detection of subtle differences in cytoskeletal dynamics and allows for in-depth analysis of both the differences and the similarities of these dynamics across cell types and phyla. Our method of quantification of actin dynamics across scales is based on optical flow, an image-analysis technique developed in the fields of robotics and navigation control that uses changes in pixel intensities to detect motion in image sequences [155, 156]. Because of the popularity of particle image velocimetry (PIV), optical flow has seen limited use on biological images. However, PIV is poorly suited for the variety of features that can be exhibited in fluorescence images of amorphous concentration fields. Indeed, a recent study indicated that optical flow may be better suited for analysis of fluorescence images, as it provides a more accurate estimate of ground-truth flow fields [71]. Here, we use optical flow to measure the dynamics of actin polymerization with submicron precision, and we further expand the utility of optical flow by introducing modeling and fitting approaches to the analysis of optical-flow vector fields. Clustering of the optical-flow data further allows us to quantify actin dynamics on the micron scale. Thus, this optical–flow-based analysis enables the identification of similarities and differences between esotaxis in neutrophil-like HL60 cells and human breast epithelial MCF10A cells across length scales.

Results

[*The main result of the study is that actin dynamics is guided similarly by ridges for MCF10A epithelial cells and HL60 neutrophil-like cells. This quantification was performed with an image analysis algorithm adapted from*

computer vision based on optical flow. This optical flow-based algorithm can robustly track actin dynamics, both the instantaneous directions of individual waveforms as well as the overall direction on flow overtime. Below, details of this algorithm and main results are highlighted and discussed.]

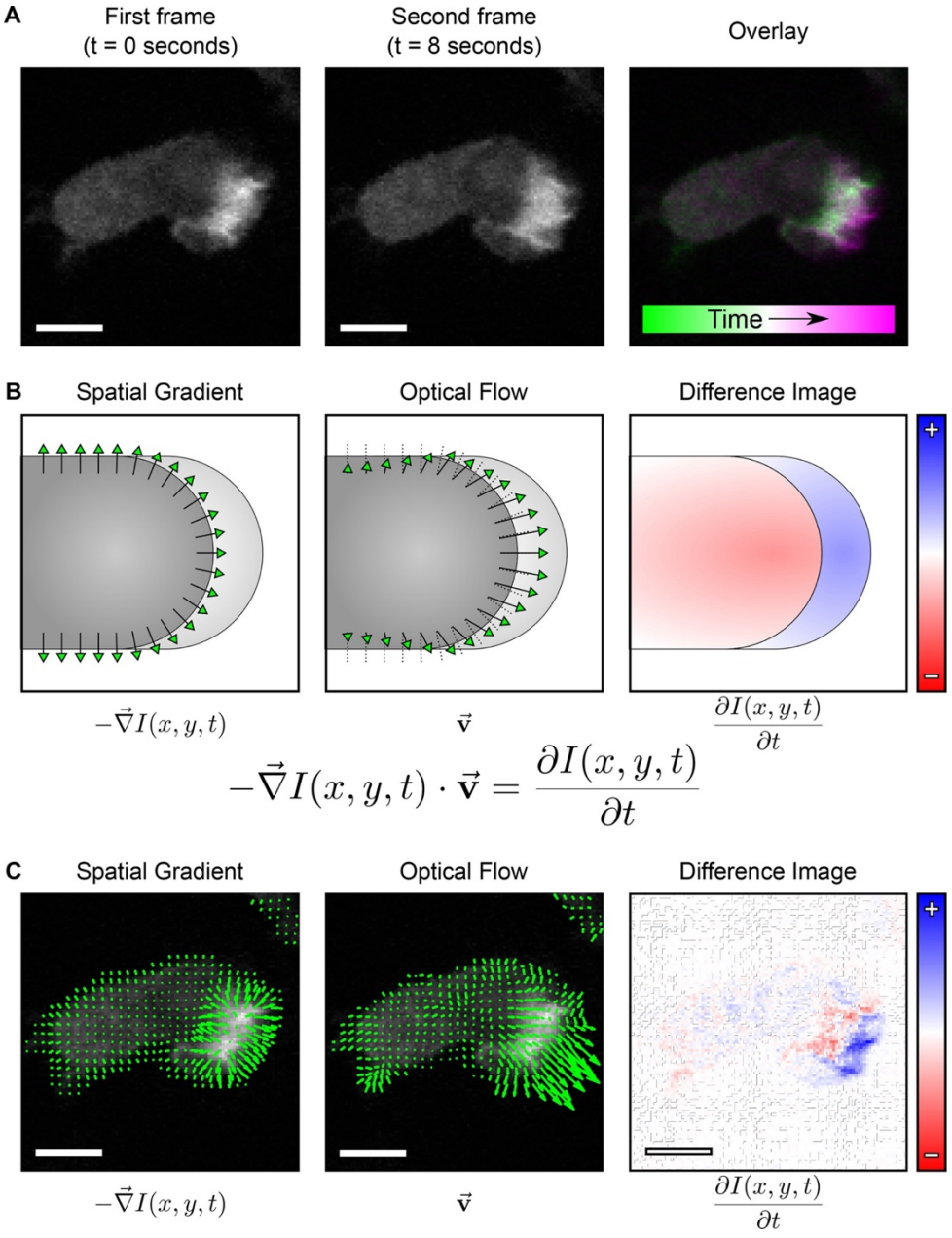

Figure 7: Optical-flow calculations capture the dynamics in movies of actin fluorescence. (A) Two frames of a representative HL60 cell obtained 8 s apart and a merged image show the dynamics of the cell's behavior over time. The schematic in B illustrates how the procedure used to carry out optical-flow calculations combines the spatial gradient of an image (left) and the difference image/temporal gradient (right) to yield the optical-flow vector field (center). These calculations are applied to the images in A and shown in the images of C. The spatial gradient field (left) and temporal gradient (right) result in the output optical-flow vector field (center). Blue pixels in the right panel of C indicate a positive change (increase) in the pixel brightness from the first frame to the second frame, and red pixels in the right panel indicate a negative change (decrease) in the pixel brightness from the first frame to the second frame. All scale bars are 5 μm.

Our method is based on a computer-vision algorithm from robotics and navigation control called optical flow [155, 156], which provides pixel-based information about the direction and magnitude of intensity flux in a series of time-lapse images. Fields of optical-flow vectors are calculated by integrating changes of intensity in space and time, as shown schematically in Figure 16. For example, two images of a migrating HL60 cell taken 8 s apart are shown with changes in time highlighted by a green-to-magenta montage (Figure 16A). The magenta region indicates growth of the actin front (which, as expected, occurs at the leading edge of the cell), and the green region indicates a decrease in actin intensity.

[…]

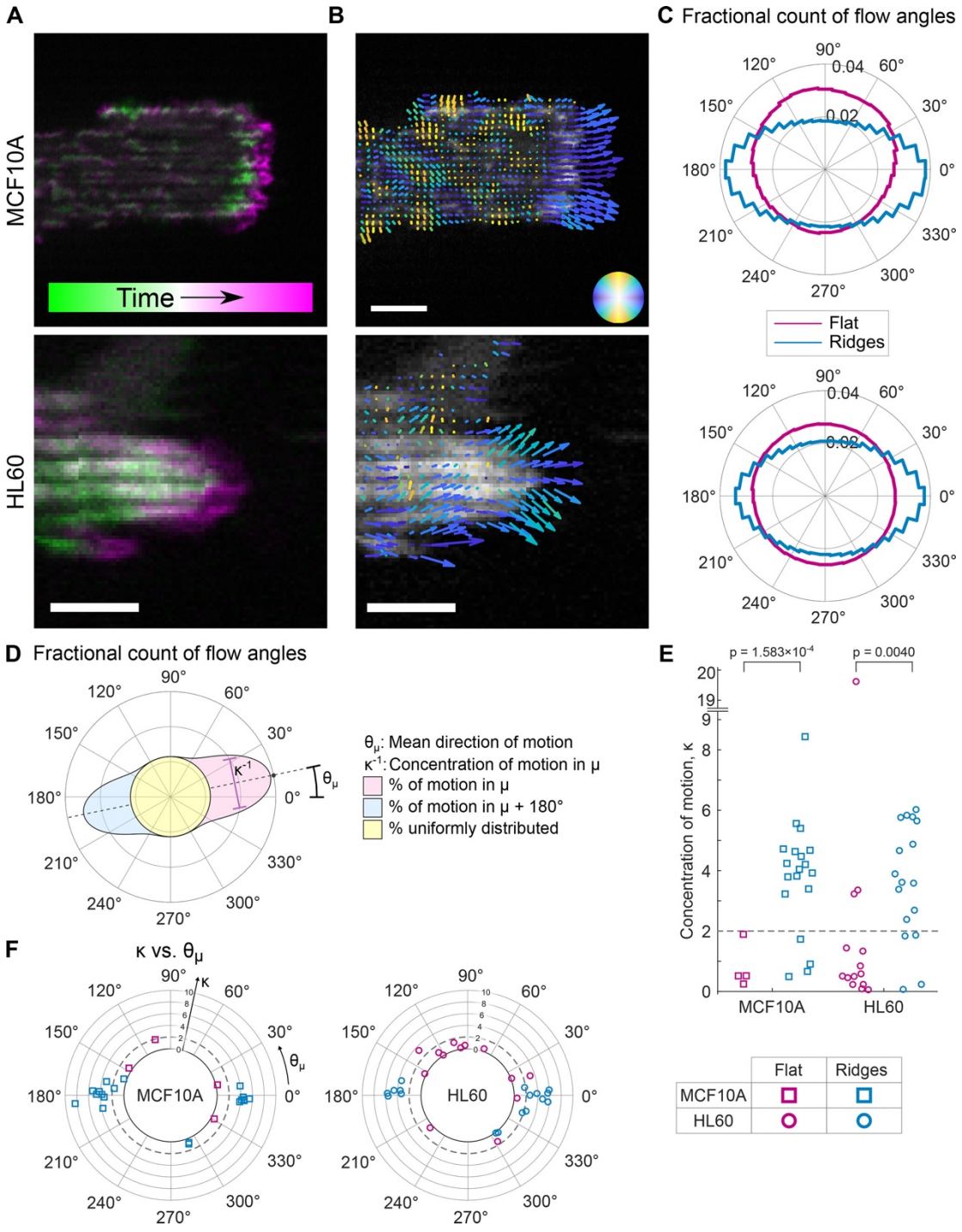

Figure 8: Using optical flow to measure pixel-scale guidance. (A) Representative merged time-lapse images of an MCF10A cell (top, 100 s apart) and an HL60 cell (bottom, 8 s apart). (B) Optical-flow vector fields colored by direction relative to the horizontal ridges. Blue indicates motion aligned with the ridges and yellow indicates motion perpendicular to the ridges. All scale bars are 5 μm. The dynamics in B are shown in Supplemental Movies

S4 and S5. (C) Cumulative distributions of the directions of optical-flow vectors for multiple HL60 and MCF10A cells on flat and ridged surfaces; all cells are weighted equally in the distribution. (N = 4 MCF10A cells on flat surfaces from three independent experiments, N = 19 MCF10A cells on ridges from four independent experiments, N = 14 HL60 cells on flat surfaces from two independent experiments, and N = 17 HL60 cells on ridges from three independent experiments.) (D) The distribution of angles can be fit to a mixture of two von Mises distributions with five fitting parameters: θμ (primary direction of motion), κ (inversely related to distribution width), and three coefficients indicating the component of motion in the θμ direction, the component in the θμ + 180° direction, and the component that is uniform. (E) In both MCF10A and HL60 cells, the distribution width, parameterized by κ, shows significant differences (p = 0.0001583 and p = 0.0040) on flat versus ridged surfaces. (F) For each cell, the mean direction of motion (angular axis) is plotted vs. κ (radial axis). Values of κ less than 2 (indicated by the dashed line) indicate cells with direction distributions that are statistically indistinguishable from a uniform distribution. We note κ = 19.6 for one HL60 cell, and this point is not visible in this figure.

Optical-flow measurements of actin intensity translation enable the quantification of the pixel-scale response of actin dynamics to nanoridge topographies (Figure 17). The green-to-magenta montages of representative HL60 and MCF10A cells show dynamic and protrusive actin behavior at the leading edge of the cell (Figure 17A). Coloring the calculated flow fields based on direction relative to the nanoridges (Figure 17B) reveals the clear bias of actin wave guidance in the direction parallel to the ridges, which is consistent with the qualitative features of the montage images in Figure 17A. Measurements of the optical-flow directions on all HL60 and MCF10A cells on both flat and ridged surface topographies are shown in the histograms of Figure 17C. In both cell types, the cumulative distribution of flow in cells on flat surfaces shows no appreciable bias in any direction. However, cells on ridges exhibit a clear preference for flow along the ridge direction. We note that the images for the MCF10A and HL60 were obtained with different objectives (100× and 60×, respectively) and at different acquisition rates (10 and 2 s between frames,

respectively). Nevertheless, the optical-flow algorithm performs well on each set of data, emphasizing the broad applicability of this approach. The two cell types also use different actin-labeling approaches (LifeAct for the MCF10A and Actin-YFP for the HL60), which may have different overexpression effects on actin dynamics [67], but in both cases produce reliable optical-flow results that are indicative of nanotopography-guided actin dynamics. For further quantification, we fit the distribution of flow directions from each cell to a bimodal von Mises model with a constant offset. The distribution used consists of a uniform component and two peaked components that are 180° apart. The five parameters of the bimodal model are illustrated in Figure 17D. The angle $\theta\mu$ indicates the direction of the main component, and $1/\kappa$ is proportional to the width of the distribution. The values of κ on ridged regions are significantly higher than those than on flat regions for both the MCF10A and the HL60 cells (Figure 4E, $p = 0.0001583$ and $p = 0.0040$), indicating that the ridges strongly guide the actin flows in a bidirectional manner. A comparison of κ and $\theta\mu$ shows that cells with a bidirectional actin flow (i.e., high κ values) are more likely to be guided along the ridge direction (Figure 16F). Although the optical-flow vector field indicates preferred directions of actin flow, it does not yield propagation speeds of actin polymerization waves directly. The magnitude of an optical-flow vector incorporates both the shift of actin in space and the change in actin intensity over time. This submicron-scale (i.e., pixel-scale) flux of intensity does not translate directly into characteristics of the dynamics that are notable on the micron-scale (i.e., tens of pixels), such as the organization of waves across ridges or the speed of wave propagation. To quantify these micron-scale characteristics, we combined similarly

oriented optical-flow vectors into clusters (Figure 18A), which were then tracked over time. To ensure that we tracked robust clusters, we applied additional constraints, such as requiring sufficiently large intensity changes. The result of this clustering was the identification of broad regions of actin that moved collectively (Figure 17B). We applied peak-finding and tracking algorithms [157] to follow the locations of maximum alignment of these optical-flow clusters on the micron scale. Although the optical-flow results shown in Figure 17 follow motion on the pixel scale, by following the peak alignment of the optical flow, we are able to track larger coordinated clusters of actin. Our tracking is consistent with the actin dynamics seen in kymographs, as shown by representative kymographs of MCF10A (Figure 18C) and HL60 (Figure 18D) cells overlaid with the tracked location of actin waves. Unlike kymographs, which are sensitive to motion along a chosen direction, tracks of clustered flow vectors reveal the micron-scale motion of actin in two dimensions. The benefits of our approach are illustrated in Figure 17C for an MCF10A cell. For the initial frames, the kymograph indicates a stationary actin structure (Figure 18C, left), but when the actin dynamics are viewed in two dimensions (Figure 18C, right), it is evident that in the early frames this wave is moving perpendicular to the ridges, a motion that cannot be captured in this one-dimensional kymograph. Thus, the combination of optical flow, clustering, and tracking allows us to follow actin waves without being limited to tracking only motion that occurs along a straight line. The speeds of the tracked actin clusters (Figure 18E) are similar to speeds derived from actin kymographs (Figure 18, C and D), despite an approximately order-of magnitude difference in speed between the two cell types that is consistent with their distinct in

vivo functions and with previously reported cell-migration speeds [158, 159]. For both cell types we find no significant difference ($p = 0.5529$ and $p = 0.0586$) between actin-wave speeds on flat and ridged surfaces (Figure 18E), implying that topography steers actin dynamics but does not alter wave speeds. On flat surfaces, the directions of the clusters are distributed uniformly for MCF10A cells but show distinct peaks in multiple directions for HL60 cells (Figure 18F). This observation is consistent with the polarized character of actin in several of the HL60 cells on flat surfaces, corresponding to κ values greater than 2 in Figure 17, E and F.

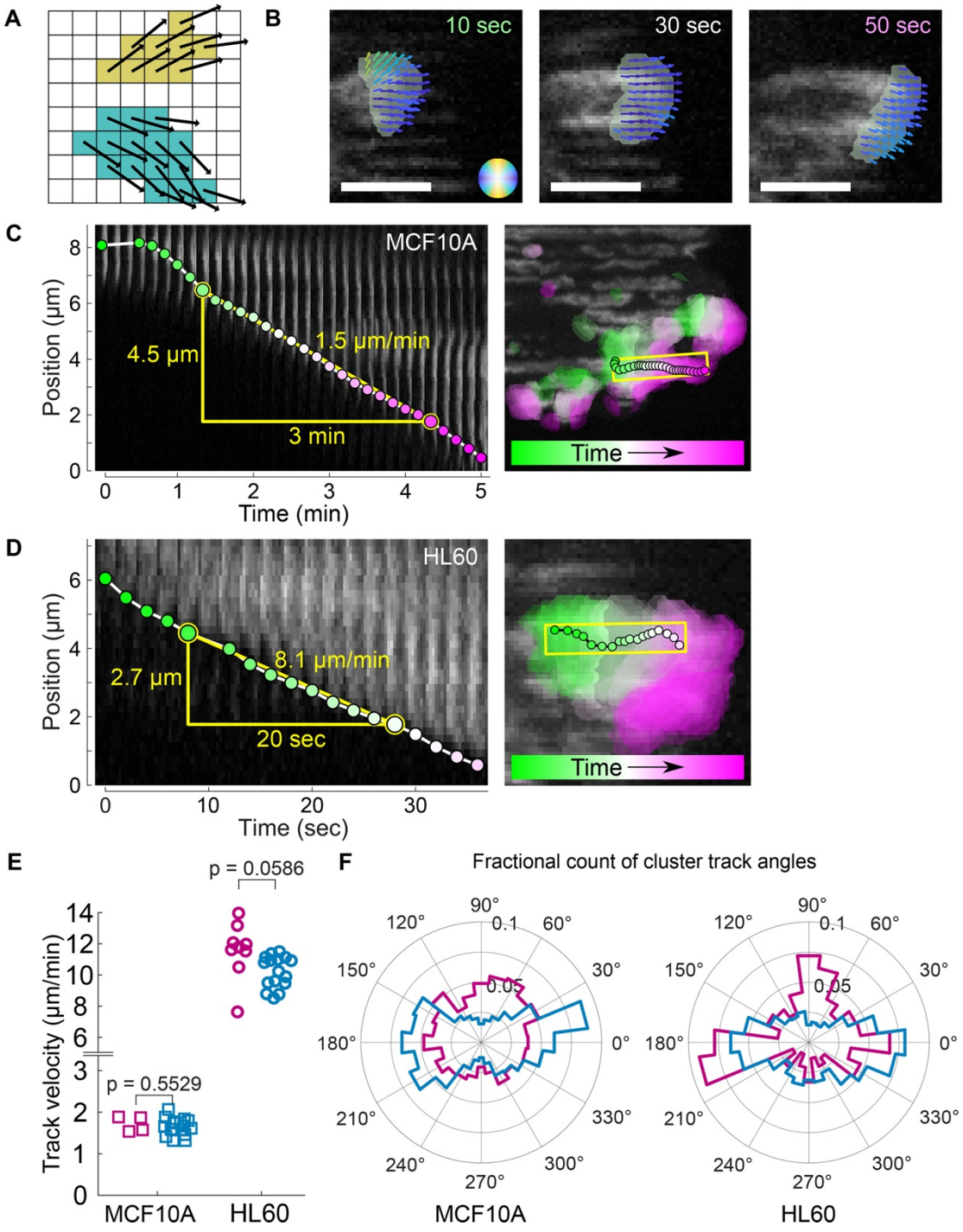

Figure 9: Clustering of optical-flow vectors to measure micron-scale dynamics. (A) Similar flow vectors are grouped into clusters. (B) Clusters contain optical-flow vectors with a wide array of orientations, resulting in micron-scale structures. All scale bars 5μm. (C, D) Particle-tracking algorithms are applied to the tracked clusters. The cluster tracks are consistent with the motion at the leading edge of the actin waves seen in the

kymographs in both HL60 (C, left) and MCF10A (D, left). Panels to the right of each kymograph show the same track in the 2D context of the cells; clusters found throughout the cell over time are indicated by colored regions. The dynamics in C and D are shown in Supplemental Movies S6 and S7, respectively. (E) The cluster tracks are used to determine speed distributions of actin waves on the ridges in the MCF10A and HL60 cells, which show no significant difference ($p = 0.5529$ and $p = 0.0586$) between flat surfaces and ridges. (F) Cumulative angle distribution of cluster track directions for multiple HL60 and MCF10A cells on flat and ridged surfaces; all cells are weighted equally in the distribution. ($N = 4$ MCF10A cells on flat surfaces from three independent experiments, $N = 17$ MCF10A cells on ridges from four independent experiments, $N = 9$ HL60 cells on flat surfaces from two independent experiments, and $N = 16$ HL60 cells on ridges from three independent experiments.)

Discussion

Extracellular texture, which is an important component of the 3D, in vivo environment, is capable of spatially patterning actin and modulating actin dynamics. Using nanoridge structures in conjunction with optical-flow approaches, we are able to probe and quantify this intracellular response to extracellular textures in a systematic manner. Previous studies of D. Discoidium [56, 57] B cells [151], and tumor-associated fibroblasts [160] showed similarity in actin response to texture, which suggests that guidance of actin driven by texture (esotaxis) is broadly conserved across cell types. Controlled textures are thus a useful model microenvironment for the systematic, reproducible, and quantitative study of intracellular dynamics and force regulation. Here we demonstrated the analysis of time-lapse images of two cell types that have distinct physiological function. Neutrophil-like HL60 cells are polarized and highly motile and respond to a variety of cues as they fulfill their role in the immune system. Epithelial MCF10A cells, however, have a nonmotile physiological function. Nevertheless, both cell types show

clear, and quantitatively similar, actin dynamics in response to surface textures. Consistent with our prior results [56, 160], we find that nanoridges lead to persistent streaks of actin that are not seen on flat surfaces. Optical flow enables the quantification of both the reproducible streaks of actin seen on nanoridged surfaces and the more chaotic actin waves seen on flat surfaces. The latter waves are typically much wider than guided actin waves. On flat surfaces the waves often change direction and can also grow wider and split. Such motion phenotypes are not easily captured with standard techniques such as kymographs. Optical flow enables us to follow these dynamics and thus yields insights beyond those derived from kymograph-based techniques. We note that optical flow is suitable for comparisons of systems imaged under different conditions (e.g., 60× vs. 100× objectives), enabling comparisons of widely varying cell sizes and migration speeds. The use of varying acquisition rates (i.e., 2 and 10 s) in this work was based on the differences in cell migration speeds of the two cell lines studied. In general, optical flow requires a frame rate such that changes in fluorescence intensity between frames are small but larger than noise. Our use of the Lucas–Kanade optical-flow constraint also makes the assumption that there is a smoothness to the flow field over a certain neighborhood, which is a length-scale parameter in the optical-flow analysis. This assumption is met by a wide variety of biological imaging data sets, and thus the use of our optical-flow approach is not limited to actin dynamics. Optical flow could provide insights into the motion of other cytoskeletal proteins, such as tubulin, or into the dynamics of other fluorescent markers that exhibit a spatially and temporally changing intensity field. Our use of clustering to study larger-scale actin dynamics

could similarly be adapted to other fluorescent markers under the assumption that there are larger-scale dynamics that move together in similar directions. In this work, we used a spinning-disk confocal microscope for image acquisition, but our analysis pipeline would also be appropriate for other imaging techniques, such as epifluorescence. When working with other imaging modalities or fluorescent markers, the size of the Lucas–Kanade neighborhood and the threshold for vector reproducibility can be adapted to only include robust results in further analysis. Using submicron-scale optical flow and associated micron-scale analysis, we have shown that both MCF10A and HL60 cells have actin flows that are biased along nanoridges. By clustering similarly oriented optical-flow vectors, we are able to measure the speed of actin waves within the cell. The measured speeds are comparable to speeds calculated from actin kymographs. Optical-flow analysis allows us to determine that the speeds do not differ significantly on flat versus ridged regions. This finding indicates that nanotopography guides, but does not fundamentally alter, the speed of actin dynamics. We measure actin-wave speeds on the order of 1 μm/min in the MCF10A cells, consistent with previously reported cell migration speeds of approximately 0.5 μm/min [159]. In the HL60 cells we find actin speeds ranging from approximately 8 to 14 μm/min, consistent with the 8 μm/min speed for cell migration previously reported [158].

Fitting the optical-flow vectors to a bimodal von Mises distribution enables quantification of the differences in the directionality of actin flows on flat and ridged surfaces in both cell lines. The fit parameters also show differences in actin polarization in these two cell lines. HL60 cells occasionally exhibit coordinated and

directed actin flows even on flat surfaces, whereas MCF10A cells on flat surfaces show uniform direction distributions of actin waves. On the micron scale, actin-wave tracks from individual HL60 cells on flat surfaces generally polarize and have a preferred direction, consistent with the behavior of immune cells, which tend to polarize and migrate in a directed manner. Tracks from MCF10A cells on a flat surface, on the other hand, are more directionally uniform for each cell. In both cell types, ridges guide actin waves in a bidirectional manner.

[This final paragraph highlights the potential limitations and potential impacts of this work.]

Although the systematic modulation and interrogation of all possible molecular factors of esotaxis is beyond the scope of this article, our analysis yields two remarkable constraints on the molecular sources of esotaxis. First, the speed of actin waves is not altered by esotaxis. Second, the directional guidance provided by nanotopography is comparable in the two cell types investigated, despite their disparate functions and migratory phenotypes. Quantitative analysis of esotaxis as a physical phenotype could yield crucial prognostic disease insights, especially in the case of cancer, in which changes in the texture of the microenvironment correlate with disease progression.

End of Excerpt

This study represents an important milestone in the context of this thesis, an algorithm which can be used to track dynamic events on multiple scales using an experimental platform like that used in Chapter 2. An important limitation of this

study, noted in the closing paragraph, was the lack of ability to monitor either intracellular trafficking or large-scale migratory behavior to connect the dynamic behavior of actin to either molecular pathways driven by this excitatory system or to functional outcomes in tumorigenic cells. Actin has also been shown to play a role in the response to electrotaxis [59, 61, 62, 87]. This technique, employed in a system able to image both intracellular dynamics and tissue-scale migratory behavior, would be able to connect changes in actin spatiotemporal morphology to electrotactic responses.

Using Optical Flow Analysis to Image Whole Organ Response to Neurochemical Cues

This study further builds upon the previous work and adapts the same optical flow-based algorithm to a very different experimental system, both in paradigm and in scale. Here, motion of a dissected crayfish gut in response to neurotransmitter exposure is tracked using optical flow. Important metrics about how these neurotransmitters result in both lateral and longitudinal muscular waves, an important consequence of intra- and inter-cellular mechanical activity, are measured without any fluorescent labels. This highlights the scale-free adaptability of this analysis workflow.

This section has been adapted from the work "Interactions between CNS regulation and serotonergic modulation of crayfish hindgut motility" by S. Pathak, N. Peña-Flores*, P. Alvarez, J. Feeley, R. Ghodssi, W. Losert, and J. Herberholz*

S. Pathak designed the analysis pipeline, analyzed collected data, and wrote the manuscript. N. Peña-Flores performed experiments and co-wrote the manuscript. P. Alvarez helped design experiment and analysis pipeline and contributed to the manuscript. J. Feeley helped analyze collected data.

Introduction

The nervous system is an information-processing system involved in sensing, integrating, and controlling all bodily functions. From interpreting internal and external sensory information received through afferent neurons to coordinating behavioral responses through muscular activation, the Central Nervous System (CNS) plays an integral role as the body's command center. While most bodily functions are controlled by the CNS, many aspects of "day to day" operation of an organism are only weakly supervised. They are instead regulated by *local* neural populations and associated cellular systems that receive sensory input and coordinate motor and neurosecretory output, especially in the gastrointestinal (GI) tract and heart [161].

Here we investigate GI motility which allows intestinal contents to mix and propel along the GI tract and is a critical function of the GI system to maintain homeostasis. Uniquely, the GI system is the only organ system to have evolved an independent nervous system – the Enteric Nervous System (ENS) - which in concert with the CNS and local biochemical environment regulates its sensory, motor and secretory functions [162]. In mammals, this complex phenomenon is modulated by overlapping and cooperating neural systems, namely, the intrinsic ENS, extrinsic innervation by the CNS, and pacemaker-like cells (interstitial cells of Cajal (ICCs) [163]. Disorders that affect GI motility such as Irritable

Bowel Syndrome (IBS), Parkinson's, Alzheimer's, and Hirschsprung's disease have a neuropathic component where dysfunctional CNS and ENS neurons lead to intestinal dysmotility [164, 165]. Compromised gut motility prevents proper nutrient absorption and can be potentially fatal (6). Notably, functional disorders of gut-brain interaction are prevalent among more than 40% of the global population [166]. Despite the pressing need to better understand the mechanisms underlying GI dysmotility in these diseases, the neuroanatomical complexity and limited accessibility of mammalian models have limited causal studies of GI motor control dynamics [167, 168].

Conveniently, basic functions of the GI system such as intestinal motility are highly conserved across evolution. The general structure and neurochemistry of the GI tract is found across species as diverse as hydra, arthropods, octopuses, and humans [169-171]. Thus, simpler animal models with more tractable and accessible GI systems provide a promising alternative to study the neurogenic mechanisms regulating hindgut motion.

In particular, crustacean decapods have a simple, accessible, and well-characterized anatomy that allows dynamic study of the interplay between the GI tract and the CNS. The posterior segment of their digestive system located in their abdomen, the hindgut, has especially simple anatomy and a physiology similar to that of mammals. The hindgut connects to the abdominal nerve cord, which is part of the CNS, via a single nerve ("Nerve 7") in crayfish [172] or a paired nerve ("Paired Intestinal Nerve") in lobster [173]. Moreover, the abdominal nerve cord contains well-characterized neuronal circuits that control important behaviors like escape and swimming [174]. Groundwork on these animal models was laid almost a century ago [173].

Crayfish, a group of inexpensive, wildly available freshwater crustaceans, are particularly well suited for *ex vivo* imaging of hindgut motility. Like the mammalian

GI tract, even without external stimulation or CNS innervation, the crayfish hindgut spontaneously manifests wave-like movement caused by the contraction of circular and longitudinal muscles [175]. These rhythmic contractions are produced by putative myogenic pacemakers [176], and modulated by the CNS (i.e., in lobster) [173], and by several neurotransmitters including serotonin [177], dopamine [178], glutamate [179] and neuropeptides [180, 181]. Moreover, the crayfish preparation is particularly robust as the hindgut and connected nervous system can remain active for several hours when pinned down in a dish filled with crayfish saline, allowing *ex vivo* real-time study of hindgut motility through direct imaging.

Among the most important mechanisms affecting hindgut motility is serotonergic modulation [182]. Serotonin (5-HT), a common neurotransmitter, plays a key role in GI motility functions and pathologies in mammals [183, 184]. It is the most abundant neuromodulator of the mammalian GI tract produced endogenously by enterochromaffin cells [185] in the intestinal wall and exogenously supplied by extrinsic neural processes [186]. This combination of endogenous and exogenous 5-HT has complex effects on a vast array of differentially localized 5-HT receptors including 5-HT1, 5-HT3, 5-HT4, and 5-HT7 [187, 188]. In crayfish, exogenous serotonergic modulation of hindgut motility and serotonergic innervation of the hindgut have been characterized [177, 189, 190]. Particularly, 5-HT receptors 5-HT1α and 5-HT2β have been shown to be differentially expressed along the crayfish hindgut [191]. Moreover, bath application of 5-HT has been shown to modulate hindgut motor activity, increasing power and frequency, in an isolated crayfish hindgut [190]. Thus, 5-HT receptors may have spatially differentiated and

concentration-dependent effects on crayfish hindgut motility, as observed in mammals. Despite the potential for understanding gut motor dynamics using a crayfish model, the invasive and low-resolution nature of traditionally used methods (e.g., force transducers) have rendered dynamic changes in the physical properties of the hindgut and their corresponding motility patterns largely unknown.

In this study, we used neuropharmacology combined with optical flow analysis - a non-invasive machine vision technique that extracts pixel level (μm) spatio-temporal flow fields - to investigate the effects of hindgut denervation and subsequent 5-HT application on hindgut motility. We predicted both CNS and 5-HT would impact different aspects of hindgut motility revealing CNS serotonergic modulation of hindgut motor control as well as parallel mechanisms intrinsic to the hindgut and independent of CNS control. To extract multiscale motility parameters related to hindgut motion, we applied Fourier analysis to our spatio-temporal flow fields to better understand the underlying time scales as well as the overall strength of hindgut motion. Previous work has shown that these dynamics can be combined to track cellular or tissue movement across different spatial and temporal scales [192, 193]. By providing a multiscale analysis framework, our study lays the groundwork for the real-time investigation of the cellular-molecular mechanisms governing CNS and serotonergic modulation of gut motility in a crayfish model. In addition, our results will inform studies in other organisms and improve our limited understanding of the complex mechanisms underlying GI motility control.

Visual Abstract

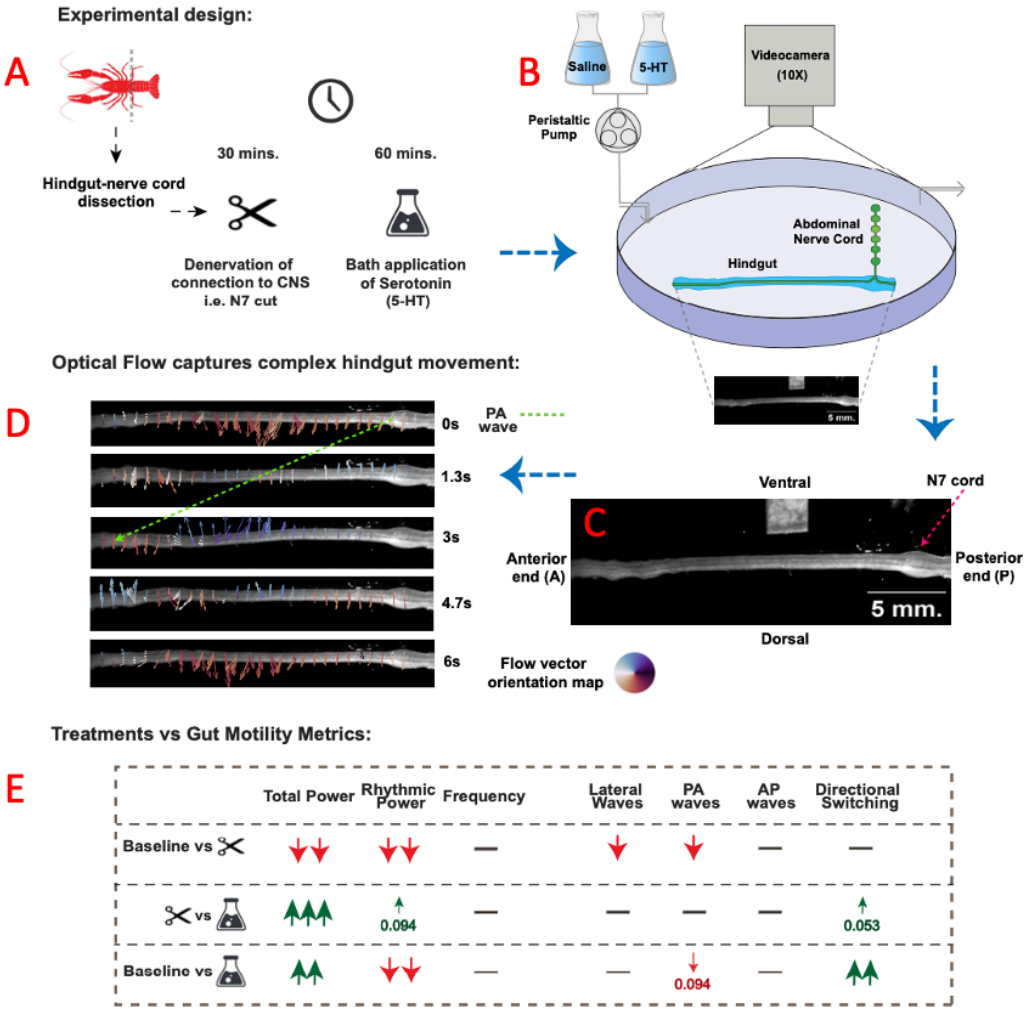

Figure 10: (a) The hindgut-nerve cord preparation was dissected from the crayfish abdomen (b) The ex-vivo hindgut-nerve cord preparation was pinned on a Sylgard-lined petri dish and video recorded at 10x magnification under 3 sequential conditions (30 minutes each): 1. perfusion of crayfish saline (baseline) on intact preparation; 2. perfusion of crayfish saline on hindgut isolated from CNS by N7 neurectomy; 3. Perfusion of crayfish saline (control) or perfusion of 5-HT at 1, 10 or 100 μM. A second control experiment video recorded the intact preparation superfused with saline throughout 90 minutes. (c) Pixel intensity-based thresholding was used to binarize the movies, extracting the hindgut outline in the process. (d) Optical flow analysis was performed on the temporally smoothed time-lapses to capture movement of the hindgut. Arrow lengths quantify the magnitude of

motion at different spatial locations whereas different directions are color coded using a circular map. Finally, all dorsal-ventral (DV) movement (perpendicular to the central axis of the gut) was averaged along the DV axis to obtain mean instantaneous velocities. Their changes in time were captured from the resultant spatio-temporal plots with blue and red bands indicating periodic DV movement along two directions. (e) Motility parameters like wave speed, wave power, spatial span and directionality were extracted from the bands. Results, and magnitudes thereof, are summarized between all conditions.

Image Analysis Workflow

[Methods involving animal preparation are outside of the scope of this study and are therefore left out in this excerpt. Attention will instead be drawn to the adaptation of the previous optical flow method to this particular application of gut imaging.]

Post-processing of images:

The raw time-lapses were cropped using ImageJ to zoom on the entire hindgut region. Transition frames accounting for denervation and 5-HT application were removed. The mean time elapsed for these cropped transition phases were 29s (denervation) and 8s (5-HT). We found hindgut movements happened at relatively long timescales, and hence for our analysis purposes, reduced the frames per second (f.p.s.) of raw images from 30 to 3 by skipping every 9 frames. All down-sampled movies were smoothed in time using the Simoncelli (5 consecutive frames with the weights - 0.036, 0.249, 0.431, 0.249, 0.036) smoothing filter [194]. Results were not considerably sensitive to the exact smoothing parameters used given that 5-frame smoothing only affects the power spectrum at higher frequencies and our characteristic motion occurred at much lower frequencies. Spatial smoothing was avoided to retain sharp features for optical flow analysis.

Identifying hindgut outline and spatio-temporal flow fields using Optical Flow:

The hindgut outline for each timeframe was extracted from raw cropped images using "*strel*" and "*imerode*" in *MATLAB*. Median pixel intensity of every image was used for the binarization threshold. Optical flow analysis was performed on the smoothed and cropped time-lapses by the Lucas-Kanade method [156]. The optical flow weight matrix around each image location was a Gaussian with a standard deviation of 2 pixels. A reliability threshold of 0.01 was also imposed to ensure movements only within the gut region were considered. Sub-threshold flow vectors were made zero. We confirmed that the size and shape of the Gaussian filter did not significantly alter motion capture and downstream analysis. Subsequently, all lateral optical flow vectors within the extracted hindgut region were averaged along the dorsal-ventral axis of that frame. As a result, we obtained dorsal-ventral motility plots (Fig. 19D), i.e., averaged lateral motion along the length of the hindgut as a function of time. For visualization, we used Gaussian smoothing on the raw flow vectors to obtain movement directions and magnitude at a larger spatial scale and ignore spurious localized effects due to random fluctuations in pixel intensity. A threshold was also applied to the resultant vector magnitudes to avoid background noise.

Power analysis of flow fields:

Applying Fast Fourier Transform (FFT) on the dorsal-ventral motility plots against the time axis, we obtained 2-D power spectral density (PSD) of lateral hindgut motion. Averaging along the spatial axis we derived the squared amplitude corresponding to all frequency components below the Nyquist frequency of 1.5Hz (sampling frequency is 3Hz). In signal processing terms, power is the sum of these squared amplitudes of all time-domain or frequency-domain samples divided by the signal length. We could identify characteristic frequency peaks (corresponding to the highest power value) and harmonics for different phases of each experiment. Similarly, using FFT against the spatial axis of motility plots led

to instantaneous power. Here, sum of the squared amplitude of all frequency components has been interchangeably used with the term 'power' as higher amplitudes of the input signal (i.e., the spatio-temporal flow field) correspond to higher mechanical power of movement.

Frequency peak of PSD:

The overall power embedded in a signal has contributions from a regular, periodic component (rhythmic power) and an irregular, noise-like component of the signal. Relative rhythmic power (rhythmic power divided by total power) from power spectral density quantifies the contribution of the peak frequency band to the overall power. It is regarded as a measure of temporal regularity in the input signal. For pure white noise, the PSD should be a flat horizontal line whereas, for a signal with a purely single frequency, the PSD would be a Dirac-delta function, and thus the relative rhythmic power near the peak should be 1. Based on this, we quantified the regularity of hindgut movement with the metric, relative rhythmic power. To define a frequency band near the peak, we used a window of 0.04 Hz symmetrically on both sides. We noted that the resulting analysis does not change qualitatively based on the chosen peak width within a reasonable range.

Lateral hindgut wave identification:

From dorsal-ventral (DV) flow fields, we applied area, length, and speed thresholds to extract individual lateral waves. First, we applied a Gaussian filter with a standard deviation of 2 pixels to extract regions having instantaneous speed above a chosen threshold (top 30% speed value, pooled across all movies). Then we used *"bwareaopen"* and *"bwlabeln" (from MATLAB)* to find and label all connected components (above the area threshold of 100 pixels) within our identified region. Finally, we extracted individual regions having a spatial span of more than 1/5th of hindgut length, separating out large-scale (spatial

and magnitude) movements from small, local fluctuations in the process. Upon identification, we used *"bwskel" (from MATLAB)* to extract the central axis of the wave regions. The spatial span divided upon the temporal span (i.e., slope of the extracted bands) provided us with the lateral speed of the wave. A wave without any 'temporal span' indicated parts of the hindgut moving in synchrony without any waveform passing through. We used the term 'mixed wave' for referring to these motility patterns. We also identified directionality of these lateral waves by labeling all anterior- posterior (AP) movements with positive wave speed and posterior-anterior (PA) movements with a negative wave speed, respectively.

Choosing time-windows for statistical analysis:

We only considered the last 15 min of the first two phases and the first 15 min of the third phase for our analysis, as we aimed to capture the response of the hindgut upon serotonergic excitation. We had observed that any increase in power is short-termed and thus for quantification, the hindgut motility was analyzed immediately before and after the application of 5-HT. We also ran statistical tests to find differences between 15 min intervals among the treatments which supported our rationale for choosing such discrete time-intervals.

Statistical testing for inter and intratreatment effects on hindgut motility parameters:

Shapiro-Wilks normality tests were performed to test distribution of motility parameters corresponding to each kind of treatment (N = 6). Thereafter Friedman and subsequently Wilcoxon's (on those passing Friedman with $p < 0.05$) signed-rank tests were performed for pairwise comparisons between different phases (baseline vs 2nd phase, baseline vs 3rd phase, 2nd phase vs 3rd phase), for each unique treatment (see supplementary tables 1, 2). All saline + N7 cut movies (N = 24) were pooled together to test the effects of N7 cut with respect to the baseline. Similarly, all saline + N7 cut + 5-HT movies (N = 18)

were pooled together to test the effects of 5-HT application with respect to the baseline as well as the N7 cut phase. p-values are reported in figures for $0.1 > p > 0.05$, * for $0.01 < p \leq 0.05$, ** for $0.001 < p \leq 0.01$, *** for $0 < p \leq 0.001$.

Results

To investigate the complex hindgut motion observed in crayfish, we developed an image analysis workflow that captures and quantifies motility parameters from brightfield images (as shown in Fig. 19C). We used 'optical flow', a widely used machine vision technique [71, 193], to detect movements at individual pixel level, constructed spatio-temporal flow fields to obtain averaged movement along the dorsal-ventral (DV) direction, and applied Fourier transformation to reduce the complex motion down to a few meaningful motility parameters. The workflow is further described in Materials and Methods.

Fig. 19C shows a representative crayfish hindgut image. The principal or anterior-posterior (AP) crayfish gut axis has the nerve cord N7 attached near the posterior (P) end (pointed at by the red arrow). Thereafter, through a sequence of timeframes, optical flow analysis demonstrates wavelike motion, at different regions of the gut. The length and direction of the arrows quantify the magnitude and direction of instantaneous motion at each spatial location.

Most movements occurred in the DV direction and very few flow vectors were aligned with the AP axis. In successive timeframes we observed a wavelike progression of localized movements along the AP axis which is perpendicular to the direction of instantaneous velocities. In this representative case, we noted a localized downward waveform traveling from the posterior to the anterior end (shown in form of the dashed green

line) in a time span of 3s. We denoted these lateral wave-like movements along the AP axis as ‘lateral waves.’ In Fig. 19D we constructed spatio-temporal (ST) motility plots that captured the wavelike progressions of mean DV movement along the length of the gut. We observed slanted alternate blue and red bands in this chosen time-window, indicating gut movement in a coordinated and periodic manner. In other instances, we also found wave-slants along the other direction, ‘mixed waves’ (vertical slants), merged waves, or waves changing directions at the midpoint of the gut. To quantify and characterize this complex motion, we applied 2-D Fast Fourier transformation to the ST motility plots and in Fourier space, averaged the contributions from all gut locations. The power spectral density (PSD) from Fig. 19E demonstrates how different frequencies contributed to the rhythmic nature of the gut movement. The total area under this PSD curve (power) quantifies the extent of gut movement and is characteristic of the mechanical power of the system undergoing motion. We observed a sharp peak in the resulting PSD close to a characteristic frequency of 0.2Hz (shown by the brown dashed line). The normalized area around the peak is a measure of temporal regularity of the movement. To extract further information about lateral waves, we measured the speed of the waves from the space-time plots as shown in Fig. 19D. The slope of the extracted bands provides us with the traveling wave speeds (shown in Fig. 19D), where we can notice different directions of waves travel within the given time window (AP movement is denoted by positive velocity values). Using a longer time span of gut motion (15 min of saline treatment on the hindgut preparation) we found a bimodal distribution of velocities with a clear preference for PA movement.

[Further highlighted in the results are the physiological effects of these waves which are outside the scope of this thesis. However, the implications of using optical flow analysis to track whole-gut movement in response to external perturbations as an experimental platform are discussed below. Of note is that existing methods for

collecting similar data require expensive and technique sensitive devices such as force transducers, which also give a limited picture of gut movement due to their small size relative to the gut length.]

Discussion

The crayfish *ex vivo* hindgut-nerve cord preparation and analysis framework we developed offers a useful model to advance our understanding of CNS regulation and interrelated neurochemical modulation of GI motility. The hindgut displayed steady power dynamics during 90 minutes of saline perfusion, allowing us to investigate transient changes after denervation and subsequent application of 5-HT. Moreover, our analysis framework was non-invasive, solely using brightfield images to study lateral movements of the hindgut. Using optical flow analysis allowed us to detect and quantify movement at pixel (equivalent to μm-scale) resolution along a significant length of the hindgut (24.2 ± 0.93 mm, or ~50% total hindgut). This method, coupled with Fourier transformation further provided us with the tools to distinguish between different regimes of lateral hindgut motility, such as rhythmic, regular movement and more uncoordinated, irregular motion. Using multiple parameters to characterize gut motility - such as frequency, total power, rhythmic power and wave direction - we were able to discriminate among the different modulating systems of hindgut motility - including the motion driven by intrinsic putative myogenic pacemakers of the hindgut [176], the CNS, and associated serotonergic effects.

While previous work in animal models has focused extensively on wave behaviors in short intestinal segments innervated by the ENS, few methods exist for directly tracking whole gut motility in concert with CNS regulation and serotonergic modulation while

providing continuous spatial localization of these movements [192, 195-197]. Our model provides a simpler anatomical platform than traditional mammalian or zebrafish models for analyzing this interplay continuously across organ systems [198]. Moreover, unlike existing techniques such as force transducers or motion analysis of short intestinal segments, this platform aggregates data across multiple scales, allowing detection of local effects as well as visualizing global behaviors. In the future, concurrent electrophysiology of N7 neurons could be combined with neuropharmacology and optical flow video analysis to expand the modalities of our multiscale analysis framework.

End of Excerpt

This study builds on the previous one and establishes the ability of our previously established optical flow technique to track dynamics on much larger scales. Though the discussion mentions the ability to observe these larger scale dynamics as a key differentiator compared to other techniques, it does so in this study as the expense of the counterpart fine scale dynamics, including tissue-scale signal trafficking and direct imaging of neuronal responses to innervation with neuromodulators. Follow-up studies, discussed in a later section of this work, seek to leverage the capabilities of new optical systems to image these two scales simultaneously, tracking intracellular calcium and neurotransmitter flow as whole organ behavioral dynamics are recorded and quantified.

Chapter 5: Optical Tools for Multiscale Measurements

The Multiscale Microscope

Introduction

Previous sections in this thesis have repeatedly emphasized the need for optical systems which can observe multiple scales simultaneously. This need has been the driving force behind this work, and culminated in the building of two dedicated optical systems which fulfill it. The first microscope we developed can record network-level activity on the scale of millimeters while imaging protein-level actin dynamics on the scale of hundreds of nanometers and is called the Multiscale Microscope (MSM). The MSM is designed to image, simultaneously, these two separate scales via a combination of epifluorescence microscopy and re-scan confocal microscopy through the same objective placed on a standard inverted microscope body. The two paths, detailed in the next subsection, are coupled through dichroic mirrors tuned to standard fluorophores used for each of these imaging types. This use of a single objective on a standard inverted microscope body allows the user to access this new imaging modality with no modifications to their normal experimental setup, as the microscope can accommodate any standard K-stage (160mm x 110mm) insert, including those for multiwell plates, 35mm petri dishes, and standard microscope slides.

Optical Description

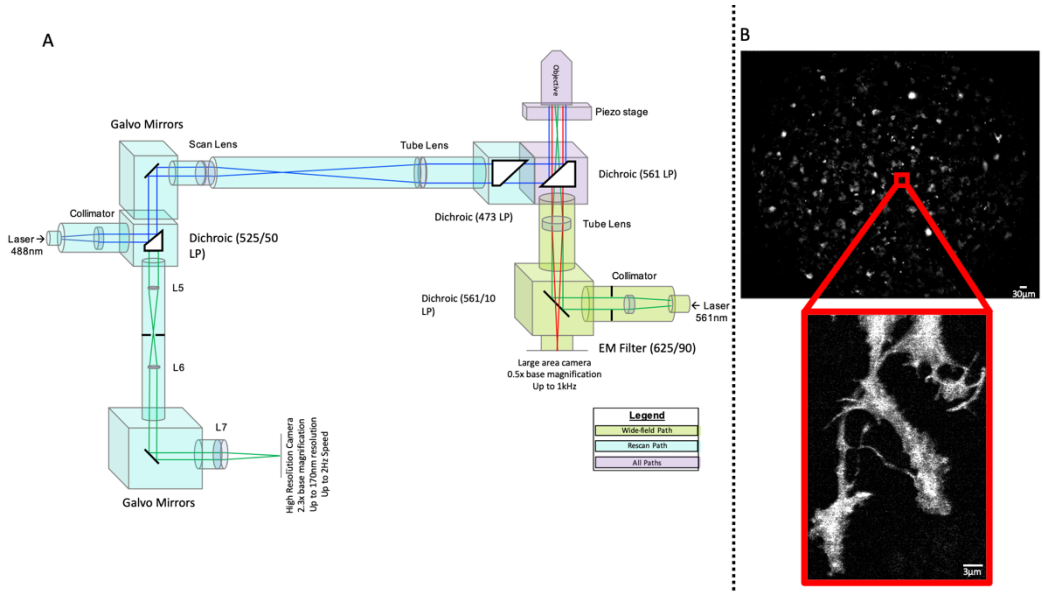

Figure 11: A) Optical layout of the Multiscale Microscope. Microscope is divided into three sections, the widefield path, in green, the rescan confocal path, in blue, and components shared by both paths, in purple. B) Simultaneous image taken in primary neuron culture stained with a fluorescent calcium dye and a fluorescent actin label. The top image shows an image from the widefield path of the calcium dye-labeled neurons. The inset shows a simultaneous image taken from the rescan confocal path of the actin label along with the size of the scanned FoV relative to the widefield FoV.

The MSM contains two entirely separate light paths imaged through the same inverted 1.4 NA 40x oil immersion objective (Olympus UMPFLN 40XO), split by dichroic mirrors. These paths are shown in Fig. 20A in detail.

The first path is a standard epifluorescence path (shown in Fig. 20A in green) in which a 561 nm laser is expanded to fill the back aperture of the objective, and the subsequent fluorescence excited by the light is expanded to the resulting image, produced on an sCMOS camera (Andor Zyla 4.2 PLUS) that was chosen for its large

number of pixels and high frame rate and thus allows us to image electrical wave propagation in real-time, at approximately 22x magnification.

The second light path (shown in Fig. 19A in blue) is a commercial re-scan confocal imaging path (purchased from Confocal.nl), in which a 488 nm laser is scanned via a galvanometric mirror and passed through an F-theta/tube lens pair onto the back aperture of the objective. The resulting fluorescence passes back through this lens pair, whose specifications were chosen to magnify the resulting image to approximately 92x magnification for high-resolution imaging of internal cellular dynamics. It is then, after passing through an emission dichroic, imaged onto a pinhole (via L5, L6, Fig. 19A) to eliminate light emanating from outside the focal plane. Finally, the light is scanned by a second galvanometric mirror onto an sCMOS camera (Andor Zyla 4.2 LT), imaged by L7 (Fig. 19A), at 2x the original scanning speed. This provides an extra lateral resolution increase (up to 170 nm with 488 nm excitation light) due to decoupling of the scanning magnification of the object and the magnification of the scanning spot, allowing super-resolution imaging of dynamics without any experimental modifications beyond those normally used for confocal microscopy [199]. Both paths are controlled via Micro-Manager 2.0, an open-source microscope control software [200].

Fig. 19B shows example imaging data from the microscope taken from each of the paths simultaneously. The top image shows an image of primary rat embryonic neurons labeled with Calbryte-590 AM. Of note is that this view contains thousands of neurons in a single FoV. The inset image is of a set of 3-4 neurons labeled with CellLight BacMAM 2.0 Actin-GFP, which transduces cells to express GFP proteins

on all g- and f-actin. Actin dynamics typically occur on a slow timescale (fully resolved with a frame rate on the order of 1-10 seconds per frame, depending on the cell line of interest), so the maximum frame rate of approximately 2 seconds per frame at full field of view with rescanning enabled (0.5 seconds per frame with cropping) is fast enough to sample cytoskeletal polymerization waves, a design objective of the microscope.

The microscope stage is also incubated for long-term imaging sessions with an Ibidi K-frame incubator to maintain a physiological environment of 37 degrees Celsius, 5% CO_2 concentration, and >80% relative humidity.

The rescan confocal path consists of an adapted rescan confocal module, acquired from Confocal.NL (RCM 1). The RCM 1 unit consists of two galvanometric scanning mirrors controlled by National Instruments DAQ cards (NI-6738) and a bypass mirror which images the sample on the camera directly to provide an epifluorescence view to aid in sample focusing. Integration of this component into our microscope involved custom adapters for laser control, as well as implementing and aligning a non-standard tube lens with custom length tube to adapt the module and the microscope to a new 2F configuration and keep the beam enclosed for safety purposes. A fiber-based voice-coil laser attenuation module provides additional power control. A set of sample images taken in both rescan confocal mode and regular confocal mode from the integrated setup appears below (Fig. 20). Image quality, after acquisition and denoising, achieved theoretical performance limits. Super-resolution images are further deconvolved using SVI Huygens analysis software to achieve up to 120nm resolution.

Resolution was tested by imaging diffraction-limited nanobeads, 100nm in size, and measuring the average full-width at half the maximum (FWHM) of their intensity distributions. The average width was found to be 179nm in X and 173 nm in Y. These parameters are within specification for the commercial rescan confocal module.

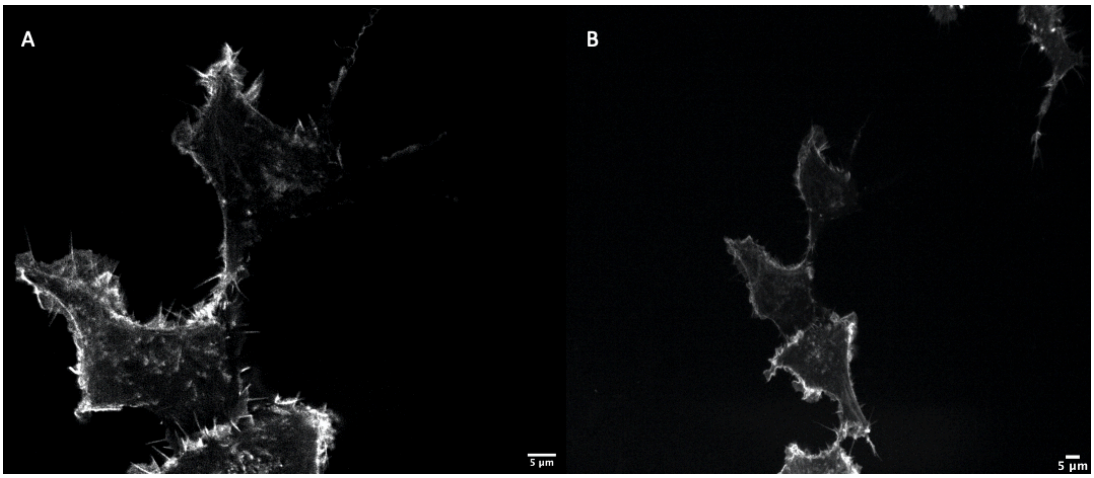

Figure 12: Example images from the MSM rescan confocal path, showing HEK-293/T cells labeled with LifeAct-GFP. A) Image taken in rescan confocal mode at full field of view, deconvolution applied. B) Image taken in diffraction-limited confocal mode at full FoV leveraging the ability to scan a 2x larger field of view at a similar speed. Dim cells in center represent FoV seen in A.

Ongoing Research

This ability to image both electrical and mechanical cellular activity on their native scales simultaneously has already proven useful to researchers in our research group. Already, multiple projects are underway which exploit these capabilities to understand how actin and calcium couple in healthy and diseased model systems as well as primary neural cell populations. Some of these projects are outlined briefly in this section.

One current study leverages wide field of view imaging to capture network dynamics in thousands of primary cortical neurons grown on ridged scaffolds at various stages of development. The goal of this work is to understand how spatial and functional network structure changes over time when the dynamics of thousands, as opposed to hundreds, of active neurons are captured. Additionally, using human neural progenitor cells (hNPCs), differences in network characteristics between healthy, aged, and Alzheimer's disease model cell lines will be compared. Actin and calcium will be imaged simultaneously in this population to understand the role that actin plays in these healthy and diseased, and developmental network dynamics. This work will augment recent findings derived from in vivo cortical imaging, where it is not possible to image thousands of cells due to technical challenges associated with intravital imaging.

Another ongoing study will quantify the contributions of astrocytic dynamics to neural network activity. In co-cultures of primary cortical neurons and astrocytes, we perform dual imaging at different spatial scales: wider FoV functional imaging of both astrocytes and neurons and high-resolution imaging of astrocytic cytoskeletal dynamics. Since our recent work demonstrated that astrocytes respond to extracellular stimuli via actin dynamics, the goal for this work is to determine whether astrocytes also use cytoskeletal dynamics to sense and respond to neural network activity [15].

One final ongoing study of note using this microscope is the imaging of calcium activity of hNPCs at different temperatures. We hope to use temperature to drive the network into a state of criticality, where the correlation length of the network becomes scale-free.

The Bio-Electrical and Mechanical Microscope

Introduction

Though the Multiscale Microscope excels at imaging interactions between slow, subcellular dynamics and fast, tissue-scale dynamics, the tube lens focal length on the rescan confocal path fixes the separation in imaged scales and the reliance on epifluorescence and confocal imaging limits the ability to image 3D dynamics. To appropriately address the need for multiscale imaging tools for tissue and organ scales, we needed to develop another system with fully decoupled imaging paths, opening the possibilities for multi-objective imaging and alternative imaging methods.

To this end, we created a second microscope, which we call the Bio-Electrical and Mechanical Microscope (BEAMM). BEAMM combines an inverted epifluorescence microscope, equipped with a camera able to image at rates up to 1kHz, with an upright laser-scanning microscope implementing a tunable femtosecond laser. Using two separate microscopes focused on the same samples allows users to choose two different objectives, with different magnifications and design specifications, tailored to their independent application. For instance, one may choose a low magnification, large area objective for the epifluorescence path letting the user see an entire tissue monolayer or whole dissected organ, while the upright microscope has a high magnification image for detailed investigation of actin, calcium, or neurotransmitter flow between cells using two-photon imaging. Unlike traditional one-photon microscopy, which excites molecules with a single high-energy photon, two-photon imaging uses two lower-energy photons to excite the fluorescent molecules. These

lower-energy photons are approximately double the wavelength of the single high-energy photon, and therefore have a much longer scattering length. Two-photon imaging can be used to image samples up to 400μm deep such as the surface layer of a gut or a brain slice created with a vibrating microtome. However, two-photon excitation requires very high peak powers due to a non-linear dependence on intensity, and therefore generally relies on ultrafast lasers. Ultrafast lasers, which generate pulses on the picosecond and femtosecond time scales, have peak powers of up to hundreds of kilowatts with standard Titanium:Sapphire sources. An additional limitation is that the focal volume size of the scanned laser, and therefore the imaging resolution, is limited to the diffraction limit of the longer-wavelength excitation light, typically around 0.6μm laterally and 3.3μm axially [35, 40, 41, 43, 201]. This is still enough to measure larger scale actin waves intracellularly and is certainly above the threshold for measuring bulk mechanical responses such as organ movement or waves of cytoskeletal activity across multiple cells. However, individual actin filaments or bundles may not be able to be resolved.

These two imaging modalities, epifluorescence and two-photon imaging, allow for the linking of not just actin and electrical dynamics, but also neurotransmitters in ex-vivo organs and slices. In addition to epifluorescence and two-photon imaging, we also included a way to not just observe activity but to drive it at the timescale at which it occurs. We implemented a separate two-photon excitation path coupled to a fast spatial light modulator (SLM), which can shape beams of light into arbitrary shapes and lets users target neurons for optogenetic excitation at the rate said excitation occurs. Optogenetics is a budding branch of biology which uses light-gated

ion channels to induce activity selectively in individual, or groups of, cells to understand how information is encoded in the collective firing patterns of populations of excitable cells [43, 202, 203]. By imaging neuronal electrical and mechanical activity on multiple scales, assessing existing functional connectivity and driving desired patterns of activity optogenetically with the SLM through a custom designed software package, BEAMM can study how cellular and tissue-scale mechanical effects cause entire organ-scale downstream consequences such as gut movement, heart beating, and neuronal network plasticity in brain slices.

Optical Description

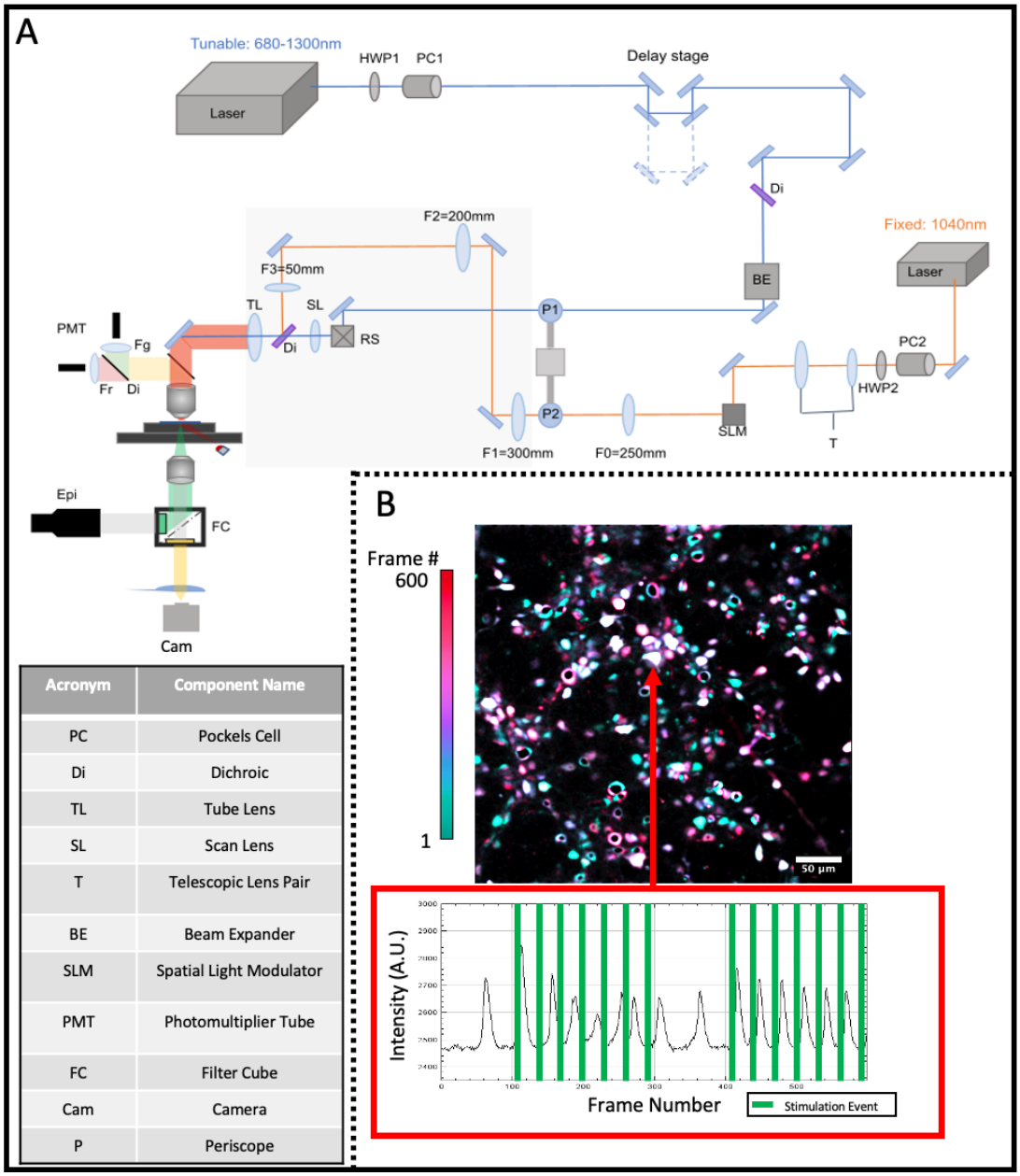

Acronym	Component Name
PC	Pockels Cell
Di	Dichroic
TL	Tube Lens
SL	Scan Lens
T	Telescopic Lens Pair
BE	Beam Expander
SLM	Spatial Light Modulator
PMT	Photomultiplier Tube
FC	Filter Cube
Cam	Camera
P	Periscope

Figure 13: A) Optical Diagram of the Bio-Electrical and Mechanical Microscope showing individual components in optical path. B) Above: Kymograph of population activity in network of in-vitro network of hNPC-derived neurons. Fluorescence detected in successive frames are shown in different colors respective to the frame. Cells shown in white have fired throughout multiple frames. Inset: Cell indicated by arrow is targeted with photostimulation light. The detected intensity of light throughout the dataset from the targeted cell is shown along with the timings of individual photostimulation events, shown in green.

As previously stated, BEAMM combines an upright two-photon imaging path, a two-photon stimulation path, and an inverted epifluorescence imaging path. The two-photon paths are both imaged through an upright Sutter Moveable Objective Microscope. The two-photon imaging path uses the tunable output of a 2W Coherent Chameleon Discovery laser, which is expanded by a 2x reflective beam expander and scanned through a galvo-resonant scanning mirror pair. It is then projected onto the back focal plane of the upright objective. Photomultiplier tubes pick up the excitation light from the two-photon imaging process in two color channels simultaneously (green and red). This path is shown in Fig. 21A as the blue optical path.

Beneath the heated, automated sample stage, an inverted microscope images the sample using an epifluorescence path as well as the SLM-modulated stimulation pattern. A Hamamatsu EMCCD camera collects the fluorescence light from a high NA objective at rates up to 1kHz. A simplified view of the internal optical path of the microscope is seen in Fig. 22A. A sample network activity kymograph is shown in Figure 13B. The fluorescence detected in successive frames is shown as different colors corresponding to the respective frame. Different neurons can be shown firing at different times. The two-photon imaging area is calibrated to this epifluorescent imaging area prior to the experiment using a fluorescent slide. The fluorescent slide allows the area scanned by the galvo-resonant scanning pair to be seen on the lower camera. The Sutter MOM upright microscope can move in four dimensions, X, Y, Z, and rotationally, and therefore this scanned area can be centered in the FoV of the lower microscope very precisely.

The two-photon stimulation beam, also sent through the same upright microscope as the two-photon imaging beam, uses a fixed output of a 5.5W 1064nm femtosecond laser (Fianum Fidelity). After emission, a half wave plate and Pockels cell are used to modulate light intensity and match the polarity of light to the preferred polarity of the SLM. The beam is then expanded by a telescopic lens set to fill the SLM surface (Boulder Nonlinear Systems 1536x1536) which shapes the light in a novel virtual lens configuration (described further below) [204]. The BNS SLM is part of a new generation of fast SLMs which can change patterns in less than 2ms, meaning that different populations can be targeted at rates as fast as action potentials occur to control activity propagation. The modified light beam reflecting from the SLM is combined with the scanned imaging beam using a notch dichroic before also projected on the back focal plane of the upright objective. This beam path is shown in Fig. 21A in orange. A sample stimulation regime is shown in Figure 13B. In the inset, a targeted neuron (indicated by red arrow) seen firing in an image of calcium activity is shown to respond reliably to successive stimulation events (shown in green overlayed with fluorescence trace).

A Virtual Lens to Reduce Holographic Artifacts

The text below outlines the unique SLM configuration seen on BEAMM, and its purpose increasing the targeting fidelity for our goal of high-speed real-time neuronal stimulation.

This section is an excerpt of "High Fidelity Spatial Light Modulator Configuration for Photo-Stimulation" by S. Aghayee, M. Weikert, P. Alvarez, G. Frank, and W. Losert. Frontiers in Physics, 2021. ***9****.*

S. Aghayee built optical systems, wrote, and adapted analysis code, wrote the manuscript, and performed experiments. M. Weikert performed preliminary experiments. P. Alvarez built optical systems and contributed to the manuscript. G. Frank contributed to the conceptual design of the experiment and optical systems.

[…]

Stimulation of individual neurons with light often does not alter the information flow in the brain in a substantive way. Emerging evidence shows that information in the brain is encoded in the simultaneous or avalanche-like firing of multiple neurons, and that these neuronal groups are usually not direct neighbors [205]. Interrogating these distributed groups of neurons, which collectively process information, requires simultaneous targeting of multiple neurons. This can be achieved by arrays that direct and modulate the intensity of light on a pixel-by-pixel basis such as Digital Micromirror Devices (DMD) [206, 207]. DMDs are well suited for targeting multiple neurons in transparent models such as *C. elegans*, where a single-photon regime is proven effective [208]. However, two-photon infrared microscopy is better suited for non-transparent tissue such as mammalian brains, because of the higher penetration of infrared light, and its quadratic dependence on intensity which results in excitation localized to the focal volume [41]. DMD devices

are not an efficient choice for two-photon excitation due to “off” pixels that reflect light away from the sample, effectively wasting laser power. This power is needed for two-photon excitation, due to its quadratic dependence on intensity and therefore requires focusing light into high intensity points. Spatial Light Modulators (SLM) have proven more suitable for such two-photon in-vivo applications due to their ability to modulate the phase of the light, preserving the power of the beam during modulation [43, 201, 209-212]. In addition to having higher intensity, phase-only SLMs also allow for the reconstruction of multiple target points in three dimensions [213, 214]. However, since SLMs create the desired light field as a 1^{st} order diffraction pattern from a pixelated phase pattern, they have imperfections and an additional reflected 0^{th} order light field [215, 216]. The 0^{th} order light is focused on the same plane as the modulated light and can be seen as a bright spot in the center of the image plane in typical SLM based multipoint stimulation systems (Figure 22A). In neuroscience applications, this would generate additional photo-stimulation at this location, and for optical micromanipulation applications, this creates an inaccessible zone right in the center of the field of view [217]. In addition to this unwanted 0^{th} order focal point, “ghost patterns” also appear, as shown in an intensity-adjusted image (i.e., displaying the log of intensity) in Figure 22B. These ghost patterns are due to the phase-only nature of many commonly used SLMs, including the one used in this study, and usually reflect the specific symmetries of the phase modulation pattern. The imperfections have first been noted in other applications of spatial light modulators that are dependent on the exact shape of a light field, such as optical trapping [218-220], where force measurements depend on an accurate gradient of

light intensity. Ghost patterns also lower the signal to noise ratio for photo-stimulation applications. Figure 22C is the target intensity pattern used for calculating

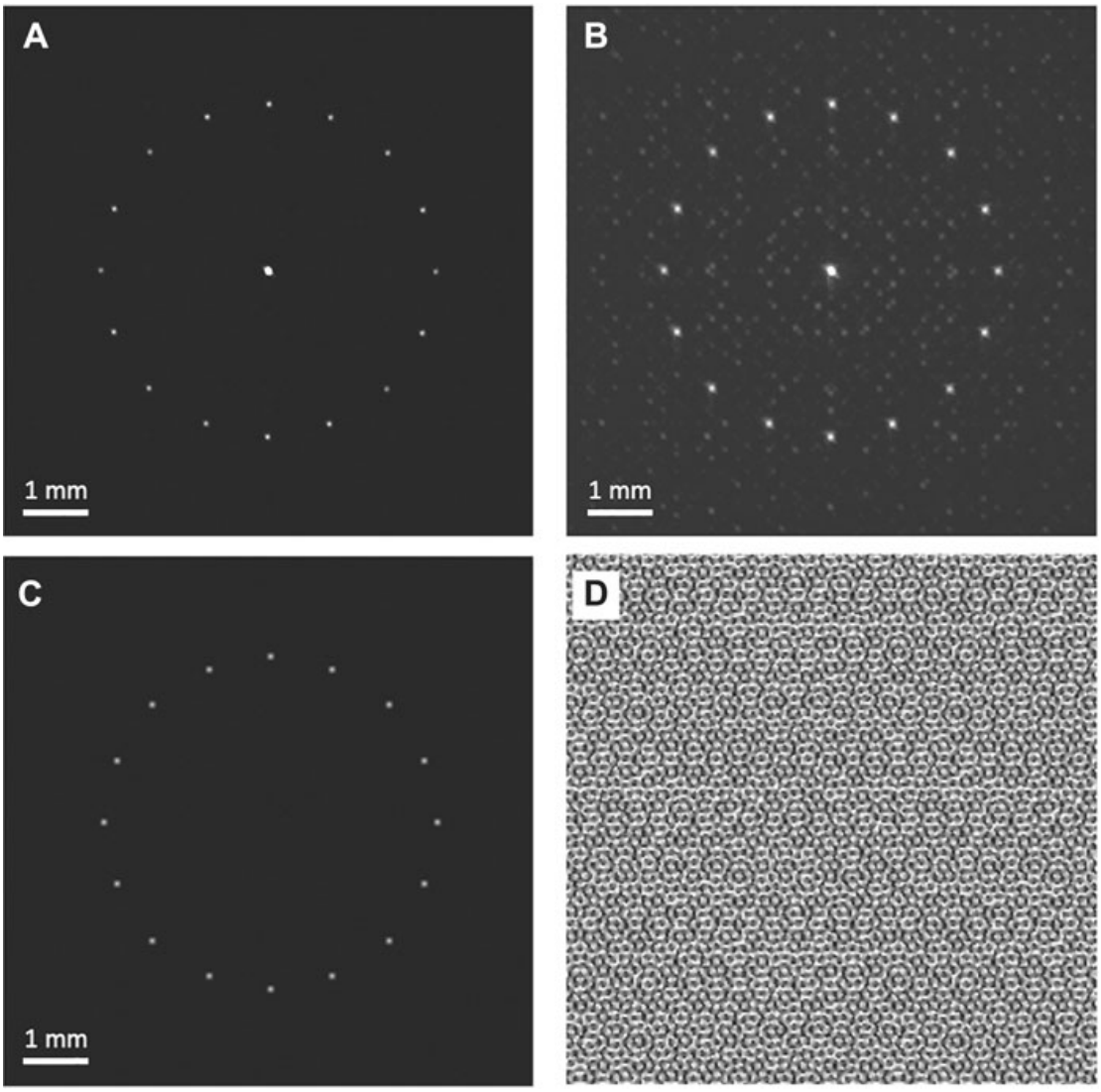

the phase mask, and Fig 22D is the associated phase mask.

Figure 14: The Unmodulated Light focuses to a central bright spot and ghost patterns are formed due to diffraction from the SLM. (A) intensity pattern from the conventional beam path captured by an sCMOS camera that is positioned in the object plane. The unmodulated light is focused at the center of the FoV by the objective lens creating an undesired central focal point. (B) intensity-adjusted representation of A highlighting ghost patterns. (C,D) Target intensity pattern and its corresponding phase mask.

[The following discussion takes place in the context of optogenetics, where target intensity patterns are difficult to anticipate in advance. These patterns,

constantly changing in structure, require a solution to remove the zeroth order light which does not block any phase information of the patterned, higher order light. In other fields, such as Structured Illumination Microscopy, higher order patterns are more predictable and can be passed while blocking zeroth order light using pinhole arrays or other structural elements in the beam path. Not discussed in the context of this thesis is that with our virtual lens beam path highlighted below, a 0^{th} order spatial filter can, and has been, implemented without negatively impacting the FoV accessible by the SLM or the spatial homogeneity of the excitation pattern.]

Spatial filters are commonly used to block the 0^{th} order light at the point in the light path where it first comes to focus [209, 221]. However, because 0^{th} order (unmodulated) and 1^{st} order (modulated) light come into focus in the same plane, it is not possible to block one without the other, i.e., it is not possible to generate points within the blocked region.

Optical designs that are based on higher order diffraction can be used to achieve complete blocking of the unmodulated light without having an inaccessible central region [222-224]. However, such designs require filtering out unmodulated light using a slit, which cuts the SLM field of view in half of its original size for binary SLMs. Moreover, less laser power is transmitted through higher order diffraction patterns. Grating-based methods have been developed that utilize SLMs capable of modulating to 4π phase delay, to simultaneously modulate for two phase masks in order to remove the replicated higher orders as well as the 0th order [225]. However, the accessibility of these techniques is somewhat limited due to the popularity of SLMs with a maximum phase modulation of 2π.

Removing the 0^{th} order from the object plane by axially shifting the focus of the unmodulated light has been suggested using a slightly converging incident beam on the SLM. The modulated light is shaped by the SLM into collimated beam, which focuses in the object plane, whereas the unmodulated beam is focused above the object plane [220]. However, this configuration has limitations. First, because the unmodulated light comes into focus above the object plane, the sample thickness is limited in this approach. Second, because a beam block is implemented in a plane where the modulated light is not collimated, both the phase and amplitude information from the modulated light is obstructed. This results in partially occluded intensity patterns. An alternative approach to limit 0th order light is through computational removal [226]. This method, which requires calculating a hologram that superimposes and cancels the unwanted intensity, is simple to implement from a hardware perspective, but requires complete characterization of the amplitude and phase components of the 0th order beam, which is unique to each pattern imposed on the SLM.

[…]

To decouple the focal planes of the unmodulated and modulated light, we added an additional focusing lens to the diffraction pattern programmed into the SLM. The SLM is thus programmed to display a modular sum of two phase modulations: the phase-mask corresponding to the target intensity pattern and a Fresnel lens. Since only the modulated light is affected by the virtual lens, the beam path is configured such that the modulated light focuses in the Fourier plane of the

unmodulated light, and the unmodulated light focuses in the Fourier plane of the modulated light.

[…]

In this system (BEAMM) we are able to demonstrate that a virtual lens configuration is compatible with two-photon excitation. A long focal distance virtual lens (F_{vl} = 600 mm) is used for two reasons: First, a longer focal distance lens leads to Fresnel fringes that are spaced further apart, limiting the interference with the added phase mask. Second, the higher order diffraction patterns generated by the weaker Fresnel virtual lens will become further spaced apart axially from the first order of diffraction. To show the two-photon excitation capability of the photo-stimulation path we used a thin, uniform fluorescent sample made by a droplet of 2 mM X-Rhod-1, AM dye in 100% dimethyl sulfoxide (DMSO), sandwiched between two No. 1.5 coverslips in the object plane. We illuminate the sample with a 1040 nm laser modulated with a superposition of a virtual lens and a phase mask that produces a ring of 16 focal points. This result shows that even in the absence of a spatial block, only the intended target points generate two-photon fluorescence. This demonstrates

the suitability of our virtual lens configuration to neuroscience photo-stimulation experiments utilizing two-photon excitation principles [38, 39].

Additionally, while ghost patterns are still formed, they occur in deeper planes and thus have reduced impact in many experimental settings, especially those in neuroscience, due to additional absorption and scattering. Below, we demonstrate this axial displacement of the ghost patterns, created by the second order of diffraction, with respect to the target pattern (Figure 23). Figure 23A shows the target pattern at the object plane (Z = 0 μm). The objective is then moved away from the sample until the second order of diffraction comes into focus at Z = 40 μm (Figure 23B). To compare the intensities created in each point, the peak intensity from each point is extracted. Figure 23C shows the distribution of the peak intensities. The first order of

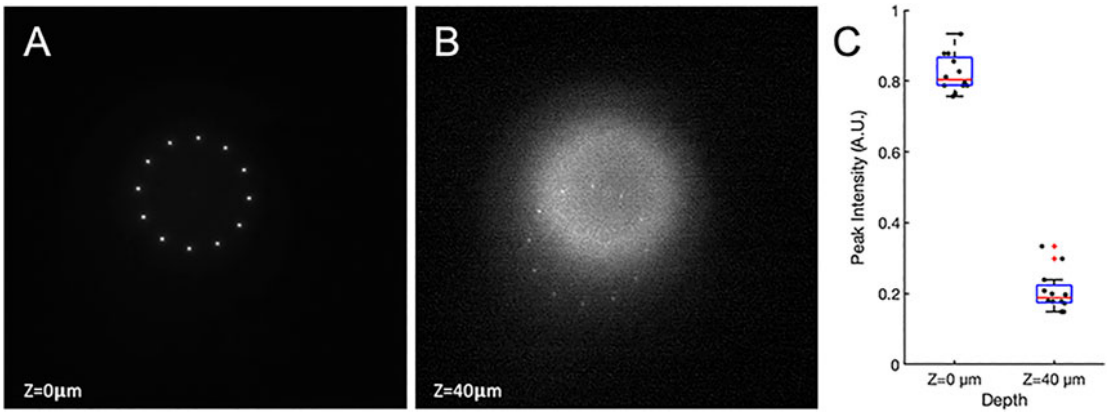

Figure 15: Two photon images of first and second order diffracted light. A thin fluorescent sample is used, sitting at the object plane of both the bottom and top objectives. (A) The first order of diffraction forms at the object plane. (B) The top objective is moved axially away from the sample by 40 μm where the second order pattern is formed. (C) The distribution of peak intensity at each point.

diffraction is shown to be approximately 4-fold more intense than the points comprising the second order ghost pattern.

[End of Excerpt]

Ongoing Research

Several projects are underway which either serve to enhance this microscope's capabilities or take advantage of its existing ones to image 3D samples across multiple spatiotemporal scales simultaneously. A selection of these projects are outlined in this section.

As previously discussed, this microscope can image, analyze, and drive activity across scales simultaneously. However, if a user wishes to assess the current state of a neuronal network and its extant patterns of firing and then elicit said patterns or train new ones, the microscope requires additional control software capable of assessing connectivity and generating related SLM phase masks in real time. To fill this role, we are creating a custom-designed software we call NeuroART (Neuronal Analysis in Real-Time). NeuroART includes a selection of GPU-accelerated automated cell segmentation routines, correlation analysis, and SLM phase mask generation and targeting in one graphical user interface. Users can see in real-time the activity and correlation coefficients of all neuronal pairs in the observed network. Users can then select cells for stimulation, and the corresponding phase mask is displayed on the SLM. Sample images of this GUI can be seen in Figure 16.

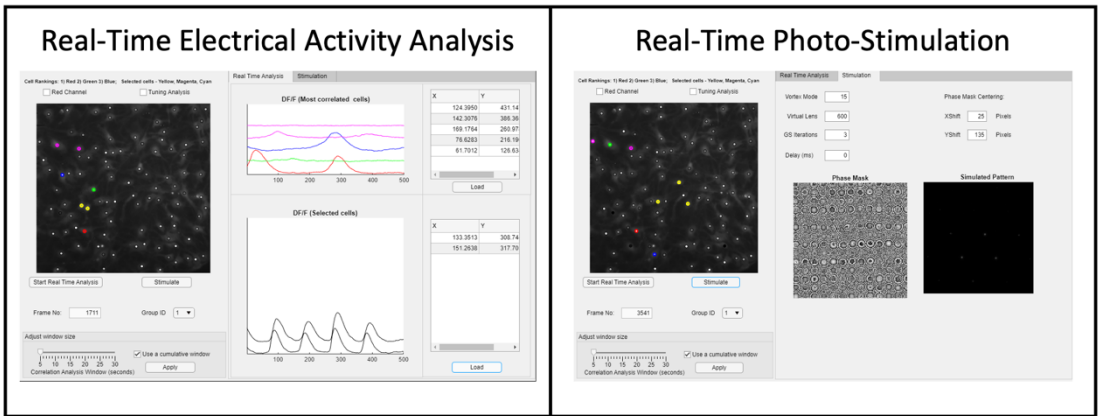

Figure 16: Left: Image showing screenshot of NeuroART real-time network analysis interface. Displayed are the activities of multiple neurons analyzed in real time, along with their locations and relative correlations. Right: Targeting interface of NeuroART, showing stimulation parameters such as phase mask centering for beam alignment, virtual lens strength for both axial targeting and axial alignment, and vortex mode, which generates optical vortices for efficient stimulation of cell membranes.

NeuroART is currently being tested on a project involving the training of a neuronal network using photostimulation. In this project, the connectivity of an existing neuronal network is assessed via correlation networks derived from calcium imaging. Low-correlation subpopulations are then targeted for training. These sub-populations are made to fire in rapid sequence repeatedly, which will likely cause STDP to occur, upregulating their connection strength [24, 227]. The connectivity of the network is then reassessed to determine the emergence of new firing patterns from the same population.

Another important project leverages the ability of the microscope to visualize below the surface of whole organs. As in Chapter 4.2, whole guts are dissected from crayfish. These guts are then perfused with fluorescent calcium dye and placed on the sample stage to be imaged via low-magnification epifluorescence. Large-scale patterns of enteric motor neuron activity will be able to be seen traveling along the

gut as lateral and peristaltic waves propagate from one end of the gut to the other [228]. At the same time, the upright microscope will be exploiting a multiphoton auto-fluorescence effect of serotonin. Endogenous serotonin has been shown in multiple cell types to exhibit UV fluorescence in response to high intensity NIR stimulation [229]. This allows for label-free quantification of the location, trafficking and amount of serotonin existing in key neurons and groups of neurons below the surface of the gut, including in the seventh nerve (N7) of the sixth abdominal ganglion (A6) which was shown in our prior study to heavily modulate gut activity. This simultaneous imaging of organ-level calcium waves and mechanical motion coupling to cell-level neurotransmitter movement is key to understanding the gut-brain axis, a proposed link between ingested food and chemicals, gut movement, and brain activity [230].

Chapter 6: Future Directions

In this chapter, I will discuss how the experimental paradigms, analysis pipelines, and optical hardware covered in this dissertation can drive future experiments. These experiments may elucidate the mechanisms and effects of electrical and mechanical coupling at multiple spatiotemporal scales. Also touched on are the theoretical impacts of this work as a potential basis to motivate further research in this area.

Section 1: Training Networks

The third chapter of this work demonstrated the ability of ridged scaffolds to generate asymmetric spatial structures in neuronal networks, but also highlighted limitations in generating functional asymmetries with the same platform. The conclusion highlighted possible methods to induce such functional asymmetries, namely, network training and large field-of-view imaging. Here I will outline potential methods for neuronal network training as well as specific experimental paradigms by which one might create bias not just in network structure but also in network function. By driving specific network phenotypes similar to those seen in-vivo, such as the aforementioned cortical columns, spatially elongated spinal networks, tonally-grouped auditory cortex neurons, or the centralized hubs seen in the visual cortex [96, 97, 120, 121, 143, 211, 231], we can understand how such phenotypes might be generated from a series of electrical, chemical, and mechanical cues in-vivo during development.

Optogenetic Training

One particularly useful method of network training, optogenetics, was mentioned at the end of chapter 3, and again during description of BEAMM in chapter 5. Optogenetics is a powerful tool that allows researchers to selectively control the activity of neurons using light. This is achieved by expressing light-sensitive proteins, such as channelrhodopsin, in specific populations of neurons typically by using a viral vector or electroporation. When these transfected neurons are exposed to light, they can be activated or inhibited, allowing for precise control over their electrical activity [203].

Optogenetics has several advantages over traditional methods of neuronal stimulation, such as electrical stimulation. For example, optogenetics allows for temporal and spatial control over neuronal activation with single cell resolution, making it ideal for investigating the complex interactions between different populations of neurons [43, 211, 212]. By exploiting the ability to shape light arbitrarily with SLMs (Spatial Light Modulators), excitation patterns can reflect certain desired spatial biases. For example, future work building on this thesis may involve stimulating linear strips of neurons parallel to underlying topography. Repeatedly stimulated neurons would likely undergo STDP (Spike-Timing-Dependent Plasticity), creating stronger connections in the direction of ridges. BEAMM as a platform can simultaneously image calcium activity in a network and modify existing connections optogenetically via its SLM path, and future research should make use of this ability to update parameters of network training in real time,

such as up- and down-regulating connectivity between extant functional groups to achieve desired network architectures.

External Electric Fields

An alternative method to optogenetics in the training of neuronal networks is the use of external electric fields. Although global electric fields lack individual neuronal specificity, it is known that low-strength external electric fields can modify subthreshold oscillations, bursting, and can even guide neurite outgrowth independent of surface topography [231, 232]. By implementing globally applied weak electric fields during neurite growth in conjunction with topography, one could direct these subthreshold oscillations and actin activity inside dendritic spines to bias functional connectivity of the resulting network. Already, global field stimulation devices for use with standard 35mm glass coverslips exist (for example, Warner Instruments RC-37). These devices are compatible with existing experimental infrastructure and fit in standard stage top incubators like those used on the MSM and BEAMM. Future experiments may use these stimulation devices with patterned scaffolds to create directed functional networks. Both BEAMM and the Multiscale microscope have already been tested with such global electrical stimulation devices in experimental compatibility trials in genetically modified HEK293/T cells.

Guiding and Preventing Aggregation

An important side effect of neuronal network growth on ridged scaffolds composed of PCL, which was discovered during the work outlined in chapter 3, is increased aggregation of neurons. This aggregation was due both to cell-material

interactions with PCL and to secondary effects imposed by the ridge structure (see Fig. 15). By tuning both ridged scaffold material properties such as stiffness and adhesivity as well as tuning ridge geometry, one may be able to prevent, or intentionally guide neuronal aggregation. This tuning may serve to enhance any extant weak functional alignment effects, as neurons are known to have stronger connections with neighboring neurons and aggregated neurons are located with no directional preference relative to other neurons in the aggregate. Guided aggregation could also be used in conjunction with training mechanisms (i.e., electric field stimulation or optogenetics) to create distinct layered, hub-and-spoke, or other complex neuronal network structures in-vitro.

Section 2: Simultaneous Imaging

A key theme of ongoing research outlined for each microscope, the Multiscale Microscope and BEAMM, is the usage of simultaneous imaging to investigate the coupled effects of electrical and mechanical signaling. In this section I highlight possible experiments building on the work performed in this thesis to perturb actin biochemically and mechanically to elicit coupled electrical-mechanical effects. These coupled effects elicited in the manner prescribed represent ideal targets for simultaneous imaging, and help maximize its overall scientific benefit in the study of electrical-mechanical coupling.

Perturbing Actin Biochemically During Calcium Imaging

The Multiscale Microscope was built with the ability to image actin and electrical activity in mind. As already shown through ongoing research, this ability is being exploited to study these two systems in multiple cell types and with multiple experimental variables. An important experiment not covered previously that would bolster evidence for the influence of mechanical remodeling on electrical transmission would be to perturb actin polymerization dynamics chemically while imaging neuronal electrical activity. Already experiments in recent collaborative projects I have been involved in show that arrested actin polymerization causes increased activity bursts and fewer correlations in neural networks grown from human neural precursor cells [126]. However, what remains unclear is not what happens during *halted* actin polymerization, but reduced or increased actin polymerization. Through the application of varying amounts of jasplakinolide, an actin filamentation promoter, or Latrunculin B, an actin monomer polymerization inhibitor, actin polymerization can be dynamically up- or downregulated. Process-localized actin can be imaged simultaneously with calcium activity and analyzed using optical flow to understand the mechanisms behind the previously observed reduced correlations. It would also elucidate whether this reduction in correlations with arrested actin polymerization occurs smoothly or in discrete steps as particular thresholds of polymerization are reached. The latter effect, discrete steps, would indicate critical thresholds in the rhythmic activity of actin in dendritic spines and a fundamental interaction between two excitable systems.

Large Field of View Imaging of Multiple Substrate Types

Mentioned in the discussion section of chapter 3 are recent results which indicate that neuronal network parameters, such as characteristic correlation length, heavily depend on the scale of observations. Already, research is being performed on the Multiscale Microscope to view the calcium activity of scaffold-grown neuronal networks on a much larger scale in conjunction with actin dynamics in individual processes, as discussed in chapter 5.1.3. Additionally, by using the dual-objective setup of BEAMM, even larger networks can be imaged, possibly more than 10mm wide. These ultra large networks may represent both better model systems and ones which can contain multiple sub-patterns on a single scaffold. Already, our lab has pioneered techniques to pattern multiple ridge pitches and pattern types, such as sawteeth and nanopillars, all on the same coverslip [233]. Neurons can be plated on all these patterns simultaneously, and the functional variance of, the transitions between, and actin dynamics inside each of these sub-networks can be imaged. This would provide a much broader perspective on the influence of mechanical forcing on electrical dynamics, as each pattern type represents the generation of a distinct network topology.

Synaptic Imaging

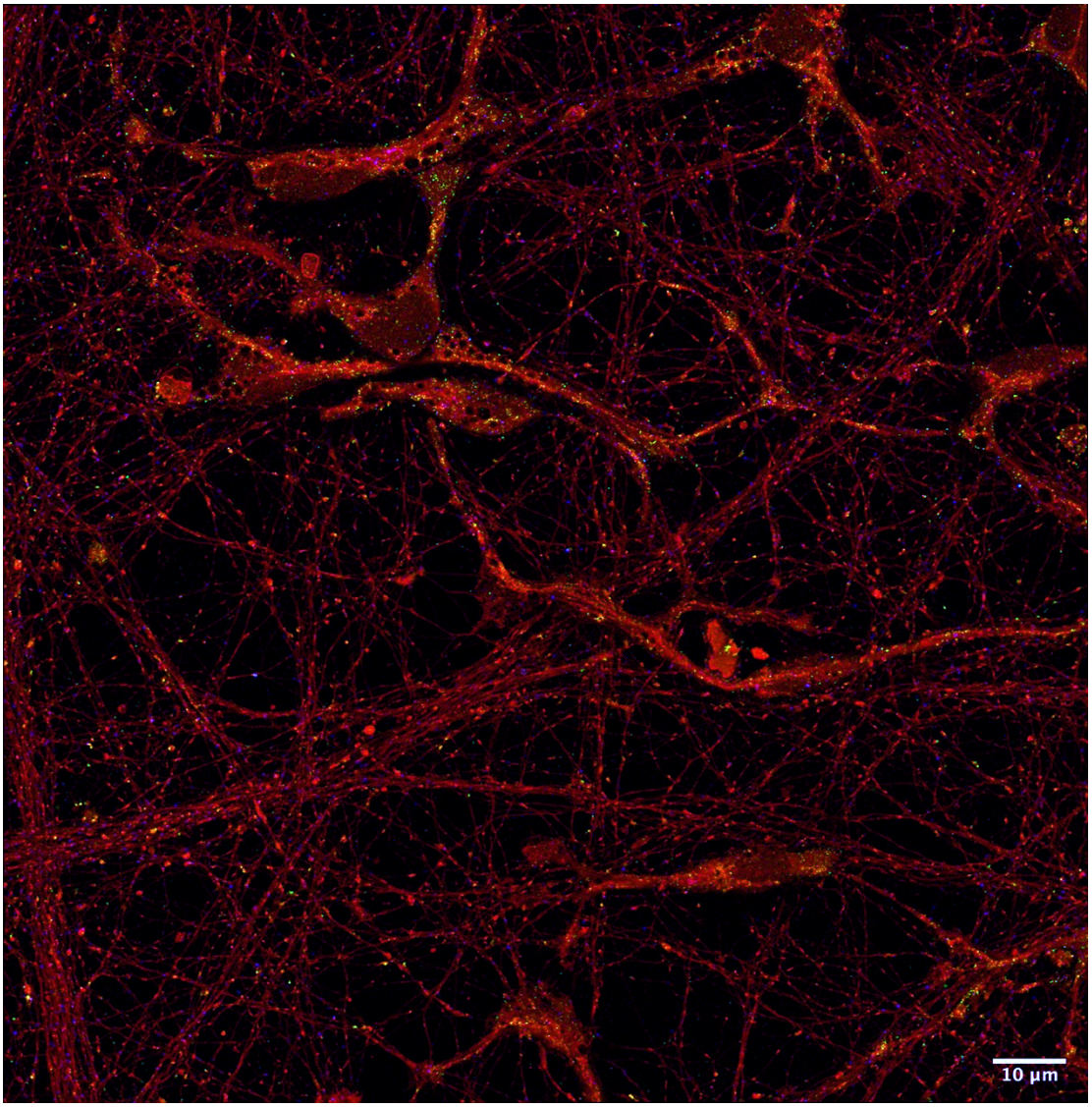

Figure 17: Image showing multi-color synaptic vesicle labeling of fixed primary neurons. Actin is labeled in red, while synaptophysin (a pre-synaptic protein) and PSD-95 (a post-synaptic protein) are labeled in green and blue, respectively. Areas of overlap between synaptophysin and PSD-95 outside of the soma indicate the existence of a synapse.

Already noted is the ability of the Multiscale Microscope to image nanoscopic structures. In addition to actin, this allows for imaging of dendritic spines and even individual synapses. Synapses are difficult to optically resolve as their size is less

than 100nm. However, their location can be inferred through labeling of synaptic vesicles. By labeling both a pre- and post-synaptic vesicle, such as synaptophysin and PSD-95, and ensuring dendritic spines themselves are visible using stable plasma membrane markers, one may infer both the location and strength of a synapse by looking at both the overlap and flow of synaptic vesicles at these dendritic spines. An example of such a staining is seen in Fig. 25. Imaging of dendritic spines responding to mechanical forcing in the form of probing with a glass micropipette has already shown to result in increased release of neurotransmitters such as glutamate [234]. Unknown, however, is if alterations in neurotransmitter release in synapses formed on structured surfaces exist due to continuous mechanical forcing. Synaptic imaging and tracking of neurotransmitter flow with either optical flow or a complementary technique such as particle image velocimetry (PIV) would provide a much deeper mechanistic understanding of the nanoscopic effects of continuous mechanical forcing on neural cells, like that which they might experience in-vivo.

Section 3: Hypotheses and Conclusions

A Mechanical Theory of Working Memory

Many people, especially those unfamiliar with medical or neuroscience, often are familiar with only two forms of memory, short- and long-term memory. There exists a third, less discussed form of memory, called working memory, which is not wholly distinct from short-term memory but temporally bridges the gap between short- and long-term. Short-term memory typically refers to the ability to hold and recall information on the seconds timescale. Long-term memory, mediated by

fundamental plasticity events, occurs over a much longer minutes-to-indefinite timescale. Working memory, in contrast to short-term and long-term memory, refers to the ability to manipulate short-term events, such as doing mental arithmetic and remembering phone numbers. These manipulations typically take tens of seconds to minutes, and therefore the information must be stored for at least that long [235].

One of the current theories of working memory involves patterns of neurotransmitter release and depletion in synapses [88]. According to this theory, the formation of working memory is associated with an increased release of neurotransmitters, such as dopamine and serotonin, at specific synapses in the brain. This increased release leads to the activation of specific neurons and the temporary strengthening of the connections between them, ultimately resulting in long-term memory formation if the information is recalled repeatedly. As the information is held in working memory, the neurotransmitters are rapidly removed, either through reuptake or degradation, maintaining the transient nature of the memory. This theory also suggests that a reduction in the levels of neurotransmitters in the synapses may contribute to a decline in working memory capacity, which is observed in aging and in certain neurological disorders such as Alzheimer's disease (AD) [236]. Conversely, meta-analyses have found that selective serotonin reuptake inhibitors, used to treat anxiety and depression amongst other mental disorders, have no significant observable effect on memory [237].

Some studies have indicated a mechanical component to working memory. In one study, structural abnormalities in the brain at the organ scale without a change in volume resulted in altered working memory performance [238]. A change in structure

without a change in volume would imply a similar neuronal density with an altered mechanical environment surrounding the cells such as a relocation of gaps and voids. This study suggests that the structural abnormalities themselves are responsible for altering electrical propagation in areas of the brain participating in the learning process. In Alzheimer's disease, there are already studies which demonstrate a role for actin in disrupted signaling pathways related to one of the main etiologies of AD, tau-induced neurodegeneration (TINd) [72]. Tau protein serves a variety of native physiological functions in the brain, including cytoskeletal networking and transportation of intracellular cargo, as shown in Fig. 26. However, in patients with TINd, tau proteins become misfolded, eventually leading to AD. Build-up of these misfolded tau proteins has been shown in cell models to induce accumulation of F-actin. Similarly, changing levels of F-actin through genetic engineering changes phenotypes seen in TINd models [72]. This feedback process loop is enhanced by the introduction of β-amyloid plaques, a pathology commonly seen in patients with AD [72]. Therefore, there exists indications that actin in particular might be a key protein which plays a role in AD pathologies and may be a potential drug target.

As already discussed thoroughly, there are connections between cellular-scale cytoskeletal modulation and network-level activity by which local mechanical cues can potentially modulate network dynamics through regulation of action potential kinetics. Further, these modified kinetics would then modulate cytoskeletal activity to reinforce or weaken existing mechanical connections to both other cells and the cellular environment. This would provide an alternative mechanism for information transfer in electrically active cells on the time scale of cytoskeletal dynamics, which

for actin is typically on the order of seconds, similar to the timescale of working memory [20, 26]. These pieces of evidence, the existing and proposed mechanistic connections between actin dynamics and electrical activity and links between working-memory diseases and actin morphologies, both hint at a deeper, more impactful point. Actin dynamics may be one of the most vital components of working memory. Perhaps, as neurotransmitters deplete and synapses undergo transient strengthening and weakening, information is stored, or at least modulated, by transiently modified actin waves and oscillations in the synapse.

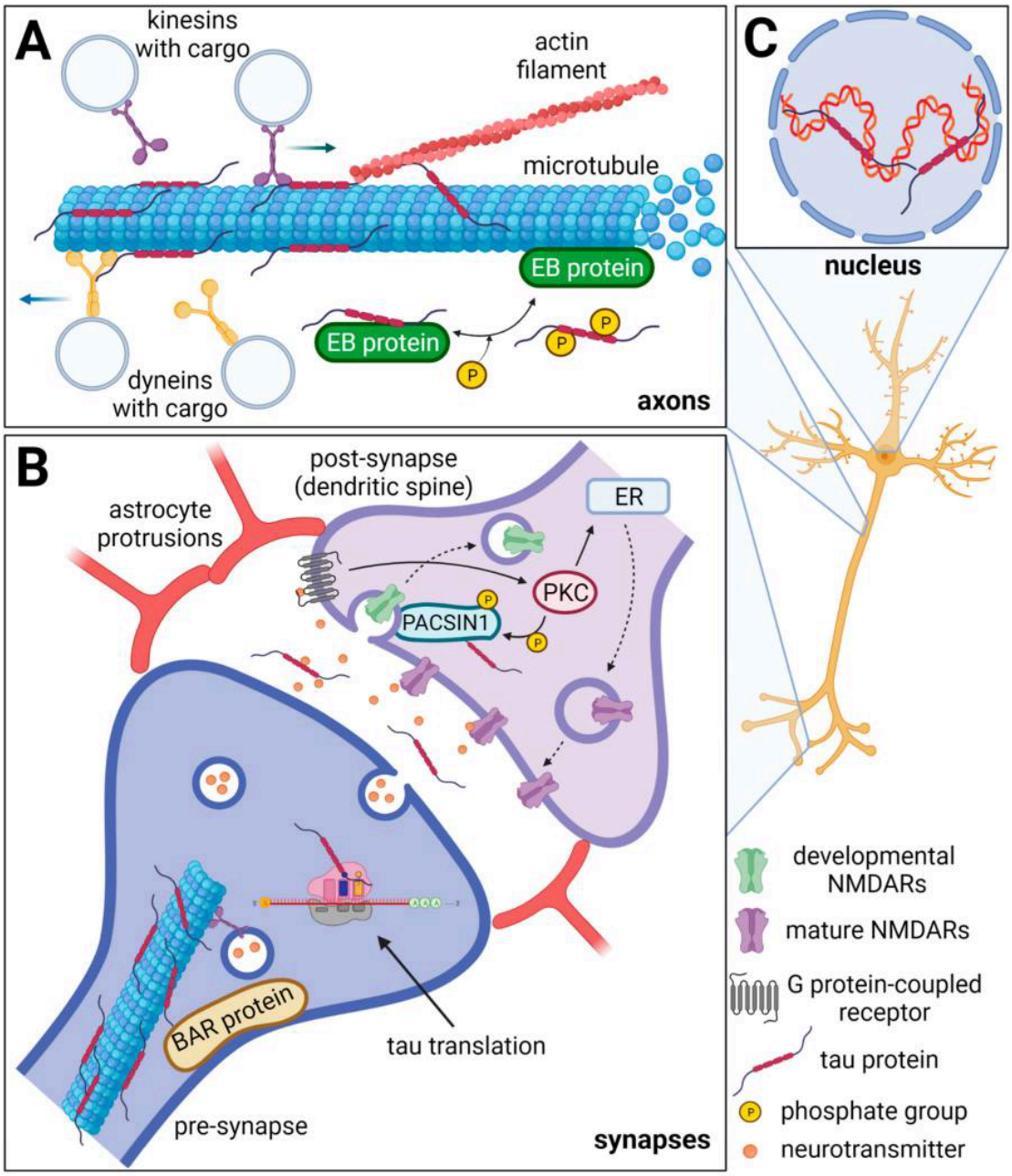

Figure 18: The physiological functions of tau protein in neurons are represented schematically. A: Axonal tau can stabilize microtubules (MTs) and facilitate cytoskeleton networking by binding actin filaments. Moreover, tau inhibits end-binding protein (EB), which regulates MT nucleation, binding to MTs, and this inhibition is reversed by tau phosphorylation. Tau also has an impact on intraneuronal transport and cargo release by competitively inhibiting the interaction of dynein and kinesin with MTs. B: In synapses, tau protein can be synthesized and released into the synaptic cleft during neuronal activity. Through its actin binding, tau can influence synaptic plasticity and neurotransmitter channel dynamics such as glutamate receptors (NMDARs) and other protein reactions through binding to protein kinases (PACSIN1 and PKC). [Tau Protein Interaction Partners and Their Roles in Alzheimer's Disease and Other Tauopathies, Sinsky, et. al, 2021, reprinted by permission of Int. J. Mol. Sci.]

Uncovering such a mechanism would mean that information holding, manipulation, and recall in the context of working memory is not solely the realm of electrical interactions. Such a mechanism would be difficult to fully prove, however. Behavioral studies on rodents would be a likely starting point. Drugs which alter actin polymerization thresholds such as rapamycin or jasplakinolide could be micro-dosed to target regions of the brain to understand how transient changes in these polymerization thresholds affect the working memory of mice. In cell models, data collection might be more complicated, involving fluorescent labeling of neurotransmitters such as serotonin using new genetically encoded serotonin indicators and decoding of natural rhythms of these neurotransmitters. Such an experimental paradigm would allow for such natural rhythms to be observed and correlated to those of actin, and each could be perturbed pharmacologically to determine their mechanistic connections. Results from studies such as these could heavily imply a role for actin in information flow, but further studies would need to be done to truly validate this hypothesis.

Final Thoughts

Investigating electromechanical coupling is key to understanding information storage and transfer in electrically active biological systems. It can act as a driver of specific network spatial topologies and a modulator of electrical activity. It also occurs at timescales that implicate it as a possible component of the storage and transfer of working memory. However, because of the vast spatial and temporal scale differences in electrical and mechanical cellular response systems, understanding how

these two systems interact with one another is difficult. Our novel microscope configurations and initial studies have shown that bridging the gap between scales is possible through leveraging synergies in technology and experiment design. My hope is that the fruits of this work inspire new research which investigates these phenomena in more detail. Already, private industries have begun to tackle some of these problems, from Neuralink and Synchron studying optimal physical designs for electrodes in the development of brain-computer interfaces, to InVivo Therapeutics Corporation releasing patterned scaffolds for neural regeneration in spinal injury [239-241]. These private companies rely on established techniques such as multiphoton microscopy to test their products, and the platforms described in this dissertation could aid in their testing and design process.

My work introduces multiscale imaging tools with separate imaging paths and separate design constraints but merges them to image the same sample. Other imaging tools with merged optical paths are in development as well, such as a microscope with simultaneous imaging paths with real-time adjustable fields of view using electrically tunable lenses [242]. In recent years, new system designs which push the boundaries of existing design constraints have already been released. These systems, like three-photon microscopes, lattice light sheet microscopes, and Spatial Light Interference microscopes, expand the application envelopes of individual microscopy techniques and would be targets for integration into new platforms designed to measure finer, faster, and better across multiple scales [243-245]. The microscopes presented in this work belong in this new generation of multiscale-

capable instruments, all poised to make accessible the ability to investigate electrical and mechanical coupling on their native spatiotemporal scales.

Appendix

A1: List of Specific Works Adapted in this Dissertation

1. *Alvarez, P., et al., Scaffold Asymmetries Drive Neuronal Network Structural, but not Functional Asymmetries. In Preparation*

2. Lee, R.M., et al., Quantifying topography-guided actin dynamics across scales using optical flow. Mol Biol Cell, 2020. 31(16): p. 1753-1764.

3. Pathak, S., et. al, Interactions between CNS regulation and serotonergic modulation of crayfish hindgut motility. In Preparation

4. *Aghayee, S., et al., High Fidelity Spatial Light Modulator Configuration for Photo-Stimulation. Frontiers in Physics, 2021.* ***9****.*

A2: BEAMM Alignment

Owing to its decoupled dual-objective design, BEAMM requires a unique alignment procedure to keep coaxial objective alignment and SLM excitation beam quality among all light paths. These procedures are outlined below and should be checked biweekly.

Coaxial Objective Alignment:

Requirements:

1. Thin fluorescent coating on #1.5 35mm dish (with fluorophore in imaging range of both microscopes)
2. Water

Procedure:

1. With microscope, camera, and illumination devices on, immerse multiphoton objective in solution.
2. Open ScanImage, Micro-Manager 2.0.
3. Using two-photon imaging (ScanIMAGE), focus on fluorescent coating, aiming to image the coating just above the coverslip.
4. With epifluorescence imaging, using low magnification objective (at least half of 2P magnification), focus on emitted light from scanned area (will look like small fluorescent box). Focusing is easier with increased EM gain and lower exposure time.

5. Center scanned area in epifluorescence field of view using Sutter Micromanipulator Controls.

6. Repeat steps 4-5 with higher magnification objective.

7. Record Sutter Micromanipulator positions. During imaging, return to these positions as “home”.

SLM Alignment:

Requirements:

Same as previous procedure.

Procedure:

1. Achieve imaged coaxial alignment.

2. Project optical vortex of mode 1 with virtual lens power of 600mm on SLM.

3. Using final lens before tube lens in SLM path, translate lens until vortex is in sharp focus.

4. Adjust SLM center using software to compensate for beam centering on SLM. Translate X-Y position digitally until sharp vortex is achieved.

5. Adjust optical axis center by adjusting 2nd to last mirror before scan lens before microscope until vortex is centered within 2P and epifluorescence FoV.

A3: MSM Alignment

Should the Multiscale Microscope require alignment, the alignment procedure is simple. It is detailed below and should be checked and repeated quarterly.

Requirements: Thorlabs Frosted Glass Alignment Disk (Part Number: DG10-1500-H1-MD)

Procedure:

1. Turn on epifluorescence path.
2. Thread alignment disk into objective port.
3. Using iris lever, shrink beam until size is only slightly larger than center hole of disk.
4. Adjust beam centering using adjustment screws on dichroic cube at 90-degree elbow of epifluorescence path, until beam evenly surrounds the hole.
5. Turn on rescan confocal path.
6. Scan small area, 256x256, with fast scanning enabled.
7. Using dichroic cube under objective, adjust square scanned area until hole at center of alignment disk is evenly surrounded by light.

Funding

Work was supported by BRAIN initiative grants U01NS090569 and U19NS107464, NSF award DGE-1632976, AFOSR MURI FA9550-16-1-0052, and AFOSR DURIP FA9550-16-1-0225

Bibliography

1. Cecchini, R. and G. Pelosi, *Alessandro Volta and his battery.* IEEE Antennas and Propagation Magazine, 1992. **34**: p. 30-37.
2. Piccolino, M., *Animal electricity and the birth of electrophysiology: the legacy of Luigi Galvani.* Brain Res Bull, 1998. **46**(5): p. 381-407.
3. Schuetze, S.M., *The discovery of the action potential.* Trends in Neurosciences, 1983. **6**: p. 164-168.
4. Cole, K.S. and H.J. Curtis, *ELECTRIC IMPEDANCE OF THE SQUID GIANT AXON DURING ACTIVITY.* J Gen Physiol, 1939. **22**(5): p. 649-70.
5. Hodgkin, A.L., *Chance and design in electrophysiology: an informal account of certain experiments on nerve carried out between 1934 and 1952.* J Physiol, 1976. **263**(1): p. 1-21.
6. Hodgkin, A.L. and A.F. Huxley, *A quantitative description of membrane current and its application to conduction and excitation in nerve.* J Physiol, 1952. **117**(4): p. 500-44.
7. Kress, G.J. and S. Mennerick, *Action potential initiation and propagation: upstream influences on neurotransmission.* Neuroscience, 2009. **158**(1): p. 211-22.
8. Kole, M.H., et al., *Action potential generation requires a high sodium channel density in the axon initial segment.* Nat Neurosci, 2008. **11**(2): p. 178-86.
9. Llorente-Folch, I., et al., *The regulation of neuronal mitochondrial metabolism by calcium.* J Physiol, 2015. **593**(16): p. 3447-62.
10. Baker, P.F., A.L. Hodgkin, and E.B. Ridgway, *Depolarization and calcium entry in squid giant axons.* J Physiol, 1971. **218**(3): p. 709-55.
11. Wen, H., et al., *Synchronous and asynchronous modes of synaptic transmission utilize different calcium sources.* eLife, 2013. **2**: p. e01206.
12. Ye, H. and A. Steiger, *Neuron matters: electric activation of neuronal tissue is dependent on the interaction between the neuron and the electric field.* Journal of NeuroEngineering and Rehabilitation, 2015. **12**(1): p. 65.
13. Fearnley, C.J., H.L. Roderick, and M.D. Bootman, *Calcium signaling in cardiac myocytes.* Cold Spring Harb Perspect Biol, 2011. **3**(11): p. a004242.
14. Guerra-Gomes, S., et al., *Functional Roles of Astrocyte Calcium Elevations: From Synapses to Behavior.* Frontiers in Cellular Neuroscience, 2018. **11**.
15. O'Neill, K.M., et al., *Decoding natural astrocyte rhythms: dynamic actin waves result from environmental sensing by primary rodent astrocytes.* bioRxiv, 2022: p. 2021.09.13.460152.
16. Evans, W.H. and P.E. Martin, *Gap junctions: structure and function (Review).* Mol Membr Biol, 2002. **19**(2): p. 121-36.

17. Zihni, C., et al., *Tight junctions: from simple barriers to multifunctional molecular gates.* Nature Reviews Molecular Cell Biology, 2016. **17**(9): p. 564-580.
18. DeFelipe, J., et al., *Estimation of the Number of Synapses in the Cerebral Cortex: Methodological Considerations.* Cerebral Cortex, 1999. **9**(7): p. 722-732.
19. Hawkins, J. and S. Ahmad, *Why Neurons Have Thousands of Synapses, a Theory of Sequence Memory in Neocortex.* Frontiers in Neural Circuits, 2016. **10**.
20. Mongillo, G., O. Barak, and M. Tsodyks, *Synaptic theory of working memory.* Science, 2008. **319**(5869): p. 1543-6.
21. Brown, T.H., Y. Zhao, and V. Leung, *Hebbian Plasticity*, in *Encyclopedia of Neuroscience*, L.R. Squire, Editor. 2009, Academic Press: Oxford. p. 1049-1056.
22. Markram, H., W. Gerstner, and P.J. Sjöström, *Spike-timing-dependent plasticity: a comprehensive overview.* Front Synaptic Neurosci, 2012. **4**: p. 2.
23. Guven, K., P. Gunning, and T. Fath, *TPM3 and TPM4 gene products segregate to the postsynaptic region of central nervous system synapses.* Bioarchitecture, 2011. **1**(6): p. 284-289.
24. Bi, G.-q. and M.-m. Poo, *Synaptic Modifications in Cultured Hippocampal Neurons: Dependence on Spike Timing, Synaptic Strength, and Postsynaptic Cell Type.* The Journal of Neuroscience, 1998. **18**(24): p. 10464-10472.
25. Mortimer, D., et al., *Growth cone chemotaxis.* Trends Neurosci, 2008. **31**(2): p. 90-8.
26. Irlbacher, K., et al., *Mechanisms and neuronal networks involved in reactive and proactive cognitive control of interference in working memory.* Neuroscience & Biobehavioral Reviews, 2014. **46**: p. 58-70.
27. Fukai, T., *A model of cortical memory processing based on columnar organization.* Biol Cybern, 1994. **70**(5): p. 427-34.
28. Panzeri, S., et al., *Neural population coding: combining insights from microscopic and mass signals.* Trends Cogn Sci, 2015. **19**(3): p. 162-72.
29. Hiratani, N. and T. Fukai, *Hebbian Wiring Plasticity Generates Efficient Network Structures for Robust Inference with Synaptic Weight Plasticity.* Frontiers in Neural Circuits, 2016. **10**(41).
30. Hill, C.L. and G.J. Stephens, *An Introduction to Patch Clamp Recording.* Methods Mol Biol, 2021. **2188**: p. 1-19.
31. Seibertz, F., et al., *A modern automated patch-clamp approach for high throughput electrophysiology recordings in native cardiomyocytes.* Communications Biology, 2022. **5**(1): p. 969.
32. Massobrio, P., et al., *In vitro studies of neuronal networks and synaptic plasticity in invertebrates and in mammals using multielectrode arrays.* Neural Plast, 2015. **2015**: p. 196195.
33. Zhou, Y., et al., *Optical Electrophysiology: Toward the Goal of Label-Free Voltage Imaging.* J Am Chem Soc, 2021. **143**(28): p. 10482-10499.
34. Thorn, K., *A quick guide to light microscopy in cell biology.* Mol Biol Cell, 2016. **27**(2): p. 219-22.

35. Combs, C.A., *Fluorescence microscopy: a concise guide to current imaging methods.* Curr Protoc Neurosci, 2010. **Chapter 2**: p. Unit2.1.
36. Grynkiewicz, G., M. Poenie, and R.Y. Tsien, *A new generation of Ca2+ indicators with greatly improved fluorescence properties.* J Biol Chem, 1985. **260**(6): p. 3440-50.
37. Paredes, R.M., et al., *Chemical calcium indicators.* Methods, 2008. **46**(3): p. 143-51.
38. Huang, Y.L., A.S. Walker, and E.W. Miller, *A Photostable Silicon Rhodamine Platform for Optical Voltage Sensing.* J Am Chem Soc, 2015. **137**(33): p. 10767-76.
39. Platisa, J., et al., *Voltage imaging in the olfactory bulb using transgenic mouse lines expressing the genetically encoded voltage indicator ArcLight.* Sci Rep, 2022. **12**(1): p. 1875.
40. Wang, J.W., et al., *Two-photon calcium imaging reveals an odor-evoked map of activity in the fly brain.* Cell, 2003. **112**(2): p. 271-282.
41. Helmchen, F. and W. Denk, *Deep tissue two-photon microscopy.* Nat Methods, 2005. **2**(12): p. 932-40.
42. Liu, X., et al., *Identification of the direction of the neural network activation with a cellular resolution by fast two-photon imaging.* Journal of Biomedical Optics, 2011. **16**(8): p. 080506.
43. Chen, I.W., E. Papagiakoumou, and V. Emiliani, *Towards circuit optogenetics.* Curr. Opin. Neurobiol., 2018. **50**: p. 179-189.
44. Diaz, M.M.S., et al., *Similar local neuronal dynamics may lead to different collective behavior.* Physical Review E, 2021. **104**(6): p. 064309.
45. Trejo, E.J.A., et al., *Finite-size correlation behavior near a critical point: A simple metric for monitoring the state of a neural network.* Physical Review E, 2022. **106**(5): p. 054313.
46. Chwalek, K., et al., *In vitro bioengineered model of cortical brain tissue.* Nat Protoc, 2015. **10**(9): p. 1362-73.
47. Celio, M.R. and I. Blumcke, *Perineuronal nets — a specialized form of extracellular matrix in the adult nervous system.* Brain Research Reviews, 1994. **19**(1): p. 128-145.
48. Ma, C.-w., *Study of perineuronal nets in plasticity of central circuitry*, in *University of Hong Kong*. 2010.
49. Fawcett, J.W., T. Oohashi, and T. Pizzorusso, *The roles of perineuronal nets and the perinodal extracellular matrix in neuronal function.* Nature Reviews Neuroscience, 2019. **20**(8): p. 451-465.
50. Leterrier, C., P. Dubey, and S. Roy, *The nano-architecture of the axonal cytoskeleton.* Nat Rev Neurosci, 2017. **18**(12): p. 713-726.
51. Hohmann, T. and F. Dehghani, *The Cytoskeleton-A Complex Interacting Meshwork.* Cells, 2019. **8**(4).
52. Bretschneider, T., et al., *Dynamic organization of the actin system in the motile cells of Dictyostelium.* J Muscle Res Cell Motil, 2002. **23**(7-8): p. 639-49.

53. Ruthel, G. and G. Banker, *Actin-dependent anterograde movement of growth-cone-like structures along growing hippocampal axons: a novel form of axonal transport?* Cell Motil Cytoskeleton, 1998. **40**(2): p. 160-73.
54. Chifflet, S. and J.A. Hernandez, *The plasma membrane potential and the organization of the actin cytoskeleton of epithelial cells.* Int J Cell Biol, 2012. **2012**: p. 121424.
55. Zhang, Y. and P. Habibovic, *Delivering Mechanical Stimulation to Cells: State of the Art in Materials and Devices Design.* Advanced Materials, 2022. **34**(32): p. 2110267.
56. Driscoll, M.K., et al., *Cellular contact guidance through dynamic sensing of nanotopography.* ACS Nano, 2014. **8**(4): p. 3546-55.
57. Sun, X., et al., *Asymmetric nanotopography biases cytoskeletal dynamics and promotes unidirectional cell guidance.* Proc Natl Acad Sci U S A, 2015. **112**(41): p. 12557-62.
58. Chen, S., et al., *Actin Cytoskeleton and Focal Adhesions Regulate the Biased Migration of Breast Cancer Cells on Nanoscale Asymmetric Sawteeth.* ACS Nano, 2019. **13**(2): p. 1454-1468.
59. Devreotes, P.N., et al., *Excitable Signal Transduction Networks in Directed Cell Migration.* Annu Rev Cell Dev Biol, 2017. **33**: p. 103-125.
60. Lee, R.M., et al., *Quantifying topography-guided actin dynamics across scales using optical flow.* Mol Biol Cell, 2020. **31**(16): p. 1753-1764.
61. Bull, A.L., et al., *Actin Dynamics as a Multiscale Integrator of Cellular Guidance Cues.* Front Cell Dev Biol, 2022. **10**: p. 873567.
62. Yang, Q., et al., *Cortical waves mediate the cellular response to electric fields.* eLife, 2022. **11**: p. e73198.
63. Miao, Y., et al., *Wave patterns organize cellular protrusions and control cortical dynamics.* Molecular Systems Biology, 2019. **15**(3): p. e8585.
64. Antunes, M., et al., *Coordinated waves of actomyosin flow and apical cell constriction immediately after wounding.* J Cell Biol, 2013. **202**(2): p. 365-79.
65. Stemmer, A., *Individual Actin Filaments Visualized by DIC (Nomarski) Microscopy.* Biol Bull, 1992. **183**(2): p. 360-361.
66. Jung, M., D. Kim, and J.Y. Mun, *Direct Visualization of Actin Filaments and Actin-Binding Proteins in Neuronal Cells.* Front Cell Dev Biol, 2020. **8**: p. 588556.
67. Melak, M., M. Plessner, and R. Grosse, *Actin visualization at a glance.* Journal of Cell Science, 2017. **130**(3): p. 525-530.
68. Ritter, A.T., et al., *Actin depletion initiates events leading to granule secretion at the immunological synapse.* Immunity, 2015. **42**(5): p. 864-76.
69. Ni, Q., et al., *A tug of war between filament treadmilling and myosin induced contractility generates actin rings.* eLife, 2022. **11**: p. e82658.
70. Koskinen, M. and P. Hotulainen, *Measuring F-actin properties in dendritic spines.* Front Neuroanat, 2014. **8**: p. 74.
71. Vig, Dhruv K., Alex E. Hamby, and Charles W. Wolgemuth, *On the Quantification of Cellular Velocity Fields.* Biophysical Journal, 2016. **110**(7): p. 1469-1475.

72. Fulga, T.A., et al., *Abnormal bundling and accumulation of F-actin mediates tau-induced neuronal degeneration in vivo.* Nat Cell Biol, 2007. **9**(2): p. 139-48.
73. Weiner, O.D., et al., *An actin-based wave generator organizes cell motility.* PLoS Biol, 2007. **5**: p. 221.
74. Sunnerberg, J.P., et al., *Axonal growth on surfaces with periodic geometrical patterns.* PLoS One, 2021. **16**(9): p. e0257659.
75. Cantiello, H.F., *Actin filaments stimulate the Na(+)-K(+)-ATPase.* Am J Physiol, 1995. **269**(5 Pt 2): p. F637-43.
76. Tuszyński, J.A., et al., *Ionic Wave Propagation along Actin Filaments.* Biophysical Journal, 2004. **86**(4): p. 1890-1903.
77. Lange, K. and J. Gartzke, *F-actin-based Ca signaling-a critical comparison with the current concept of Ca signaling.* J Cell Physiol, 2006. **209**(2): p. 270-87.
78. Lanner, J.T., et al., *Ryanodine receptors: structure, expression, molecular details, and function in calcium release.* Cold Spring Harb Perspect Biol, 2010. **2**(11): p. a003996.
79. Uehara, K., et al., *Localization of ryanodine receptor 3 in the sinus endothelial cells of the rat spleen.* Cell Tissue Res, 2004. **317**(2): p. 137-45.
80. Gunning, P., G. O'neill, and E. Hardeman, *Tropomyosin-Based Regulation of the Actin Cytoskeleton in Time and Space.* Physiological Reviews, 2008. **88**(1): p. 1-35.
81. Navarro, A.I. and B. Rico, *Focal adhesion kinase function in neuronal development.* Current Opinion in Neurobiology, 2014. **27**: p. 89-95.
82. Valiente, M., et al., *Focal Adhesion Kinase Modulates Radial Glia-Dependent Neuronal Migration through Connexin-26.* The Journal of Neuroscience, 2011. **31**(32): p. 11678.
83. Yang, Y.C., et al., *Focal Adhesion Kinase Is Required, But Not Sufficient, for the Induction of Long-Term Potentiation in Dentate Gyrus Neurons In Vivo.* The Journal of Neuroscience, 2003. **23**(10): p. 4072.
84. Wei, J.F., et al., *Formation of Kv2.1-FAK complex as a mechanism of FAK activation, cell polarization and enhanced motility.* J Cell Physiol, 2008. **217**(2): p. 544-57.
85. Chifflet, S., J.A. Hernandez, and S. Grasso, *A possible role for membrane depolarization in epithelial wound healing.* Am J Physiol Cell Physiol, 2005. **288**(6): p. C1420-30.
86. Zhao, M., *Electrical fields in wound healing-An overriding signal that directs cell migration.* Semin Cell Dev Biol, 2009. **20**(6): p. 674-82.
87. Song, B., et al., *Electric signals counterbalanced posterior vs anterior PTEN signaling in directed migration of Dictyostelium.* Cell & Bioscience, 2021. **11**(1): p. 111.
88. Tarnow, E., *Short term memory may be the depletion of the readily releasable pool of presynaptic neurotransmitter vesicles of a metastable long term memory trace pattern.* Cogn Neurodyn, 2009. **3**(3): p. 263-9.

89. McKayed, K.K. and J.C. Simpson, *Actin in action: imaging approaches to study cytoskeleton structure and function.* Cells, 2013. **2**(4): p. 715-31.
90. Piston, D.W., *Choosing objective lenses: the importance of numerical aperture and magnification in digital optical microscopy.* Biol Bull, 1998. **195**(1): p. 1-4.
91. Elliott, A.D., *Confocal Microscopy: Principles and Modern Practices.* Curr Protoc Cytom, 2020. **92**(1): p. e68.
92. Sofroniew, N.J., et al., *A large field of view two-photon mesoscope with subcellular resolution for in vivo imaging.* eLife, 2016. **5**: p. e14472.
93. Stelzer, E.H.K., et al., *Light sheet fluorescence microscopy.* Nature Reviews Methods Primers, 2021. **1**(1): p. 73.
94. Xia, F. and K. Youcef-Toumi, *Review: Advanced Atomic Force Microscopy Modes for Biomedical Research.* Biosensors, 2022. **12**(12): p. 1116.
95. Silva, N.A., et al., *From basics to clinical: a comprehensive review on spinal cord injury.* Prog Neurobiol, 2014. **114**: p. 25-57.
96. Tischbirek, C.H., et al., *In Vivo Functional Mapping of a Cortical Column at Single-Neuron Resolution.* Cell Reports, 2019. **27**(5): p. 1319-1326.e5.
97. Xue, W., et al., *Anisotropic scaffolds for peripheral nerve and spinal cord regeneration.* Bioactive Materials, 2021. **6**(11): p. 4141-4160.
98. Tarricone, G., I. Carmagnola, and V. Chiono, *Tissue-Engineered Models of the Human Brain: State-of-the-Art Analysis and Challenges.* Journal of Functional Biomaterials, 2022. **13**(3): p. 146.
99. Gladkov, A., et al., *Design of Cultured Neuron Networks in vitro with Predefined Connectivity Using Asymmetric Microfluidic Channels.* Scientific Reports, 2017. **7**(1): p. 15625.
100. Koroleva, A., et al., *In Vitro Development of Human iPSC-Derived Functional Neuronal Networks on Laser-Fabricated 3D Scaffolds.* ACS Applied Materials & Interfaces, 2021. **13**(7): p. 7839-7853.
101. Poli, D., V.P. Pastore, and P. Massobrio, *Functional connectivity in in vitro neuronal assemblies.* Frontiers in Neural Circuits, 2015. **9**.
102. Casanova, A., et al., *Self-Aligned Functionalization Approach to Order Neuronal Networks at the Single-Cell Level.* Langmuir, 2018. **34**(22): p. 6612-6620.
103. Seo, J., et al., *Neuro-taxis: Neuronal movement in gradients of chemical and physical environments.* Developmental Neurobiology, 2020. **80**(9-10): p. 361-377.
104. Solanki, A., et al., *Axonal alignment and enhanced neuronal differentiation of neural stem cells on graphene-nanoparticle hybrid structures.* Adv Mater, 2013. **25**(38): p. 5477-82.
105. Pardo-Figuerez, M., et al., *Controlled Arrangement of Neuronal Cells on Surfaces Functionalized with Micropatterned Polymer Brushes.* ACS Omega, 2018. **3**(10): p. 12383-12391.
106. Kim, Y., et al., *Nano-Architectural Approaches for Improved Intracortical Interface Technologies.* Front Neurosci, 2018. **12**: p. 456.

107. Hoffman-Kim, D., J.A. Mitchel, and R.V. Bellamkonda, *Topography, cell response, and nerve regeneration.* Annu Rev Biomed Eng, 2010. **12**: p. 203-31.
108. Marcus, M., et al., *Interactions of Neurons with Physical Environments.* Advanced Healthcare Materials, 2017. **6**(15): p. 1700267.
109. Sedaghati, T. and A.M. Seifalian, *Nanotechnology and bio-functionalisation for peripheral nerve regeneration.* Neural Regen Res, 2015. **10**(8): p. 1191-4.
110. Bérces, Z., et al., *Neurobiochemical changes in the vicinity of a nanostructured neural implant.* Scientific Reports, 2016. **6**(1): p. 35944.
111. Abend, A., et al., *Proliferation and Cluster Analysis of Neurons and Glial Cell Organization on Nanocolumnar TiN Sub-Strates.* Int J Mol Sci, 2020. **21**(17).
112. Duru, J., et al., *Engineered Biological Neural Networks on High Density CMOS Microelectrode Arrays.* Frontiers in Neuroscience, 2022. **16**.
113. Aebersold, M.J., et al., *"Brains on a chip": Towards engineered neural networks.* TrAC Trends in Analytical Chemistry, 2016. **78**: p. 60-69.
114. Abidian, M.R., et al. *In-vivo Evaluation of Chronically Implanted Neural Microelectrode Arrays Modified with Poly (3,4-ethylenedioxythiophene) Nanotubes*. in *2007 3rd International IEEE/EMBS Conference on Neural Engineering*. 2007.
115. Ereifej, E.S., et al., *The Neuroinflammatory Response to Nanopatterning Parallel Grooves into the Surface Structure of Intracortical Microelectrodes.* Advanced Functional Materials, 2018. **28**(12): p. 1704420.
116. Slavík, J., et al. *Hippocampal Neurons' Alignment on Quartz Grooves and Parylene Cues on Quartz Substrate*. Applied Sciences, 2021. **11**, DOI: 10.3390/app11010275.
117. Rajnicek, A., S. Britland, and C. McCaig, *Contact guidance of CNS neurites on grooved quartz: influence of groove dimensions, neuronal age and cell type.* Journal of Cell Science, 1997. **110**(23): p. 2905-2913.
118. Ferrari, A., et al., *Nanotopographic control of neuronal polarity.* Nano Lett, 2011. **11**(2): p. 505-11.
119. Johansson, F., et al., *Axonal outgrowth on nano-imprinted patterns.* Biomaterials, 2006. **27**(8): p. 1251-8.
120. Katoh, H., K. Yokota, and M.G. Fehlings, *Regeneration of Spinal Cord Connectivity Through Stem Cell Transplantation and Biomaterial Scaffolds.* Front Cell Neurosci, 2019. **13**: p. 248.
121. Stokols, S. and M.H. Tuszynski, *Freeze-dried agarose scaffolds with uniaxial channels stimulate and guide linear axonal growth following spinal cord injury.* Biomaterials, 2006. **27**(3): p. 443-451.
122. Kim, Y.-t., et al., *The role of aligned polymer fiber-based constructs in the bridging of long peripheral nerve gaps.* Biomaterials, 2008. **29**(21): p. 3117-3127.
123. Yang, X., et al., *Cytoskeletal actin microfilaments and the transient outward potassium current in hypertrophied rat ventriculocytes.* J Physiol, 2002. **541**(Pt 2): p. 411-21.

124. Prosser, B.L., C.W. Ward, and W.J. Lederer, *X-ROS signaling: rapid mechano-chemo transduction in heart.* Science, 2011. **333**(6048): p. 1440-5.
125. Terzic, A. and Y. Kurachi, *Actin microfilament disrupters enhance K(ATP) channel opening in patches from guinea-pig cardiomyocytes.* J Physiol, 1996. **492 (Pt 2)**: p. 395-404.
126. Gates, S.J., et al., *Coupled Biomechanical and Ionic Excitability in Developing Neural Cell Networks.* bioRxiv, 2023: p. 2023.02.15.528510.
127. Spreizer, S., A. Aertsen, and A. Kumar, *From space to time: Spatial inhomogeneities lead to the emergence of spatiotemporal sequences in spiking neuronal networks.* PLOS Computational Biology, 2019. **15**(10): p. e1007432.
128. Sahu, M.P., et al., *Culturing primary neurons from rat hippocampus and cortex.* Neuronal Signal, 2019. **3**(2): p. Ns20180207.
129. Wright, P.W., et al., *Functional connectivity structure of cortical calcium dynamics in anesthetized and awake mice.* PLoS One, 2017. **12**(10): p. e0185759.
130. Nietz, A.K., et al., *Wide-Field Calcium Imaging of Neuronal Network Dynamics In Vivo.* Biology, 2022. **11**(11): p. 1601.
131. Firestein, B.L., et al., *Cypin: A Cytosolic Regulator of PSD-95 Postsynaptic Targeting.* Neuron, 1999. **24**(3): p. 659-672.
132. Campanello, L., et al., *Signaling through polymerization and degradation: Analysis and simulations of T cell activation mediated by Bcl10.* PLOS Computational Biology, 2021. **17**(5): p. e1007986.
133. Sarker, M., et al., *Strategic Design and Fabrication of Nerve Guidance Conduits for Peripheral Nerve Regeneration.* Biotechnol J, 2018. **13**(7): p. e1700635.
134. Akcay, G. and R. Luttge, *Stiff-to-Soft Transition from Glass to 3D Hydrogel Substrates in Neuronal Cell Culture.* Micromachines (Basel), 2021. **12**(2).
135. Ghasemi-Mobarakeh, L., et al., *Bio-functionalized PCL nanofibrous scaffolds for nerve tissue engineering.* Materials Science and Engineering: C, 2010. **30**(8): p. 1129-1136.
136. Rosso, G., P. Young, and V. Shahin, *Mechanosensitivity of Embryonic Neurites Promotes Their Directional Extension and Schwann Cells Progenitors Migration.* Cellular Physiology and Biochemistry, 2017. **44**(4): p. 1263-1270.
137. Fujioka, T., et al., *β1 integrin signaling promotes neuronal migration along vascular scaffolds in the post-stroke brain.* EBioMedicine, 2017. **16**: p. 195-203.
138. Park, Y.K. and Y. Goda, *Integrins in synapse regulation.* Nat Rev Neurosci, 2016. **17**(12): p. 745-756.
139. Lilja, J. and J. Ivaska, *Integrin activity in neuronal connectivity.* J Cell Sci, 2018. **131**(12).
140. Yurchenko, I., et al., *Neuronal Growth and Formation of Neuron Networks on Directional Surfaces.* Biomimetics (Basel), 2021. **6**(2).
141. Doherty, P. and F.S. Walsh, *Signal transduction events underlying neurite outgrowth stimulated by cell adhesion molecules.* Current Opinion in Neurobiology, 1994. **4**(1): p. 49-55.

142. Kiryushko, D., V. Berezin, and E. Bock, *Regulators of neurite outgrowth: role of cell adhesion molecules.* Ann N Y Acad Sci, 2004. **1014**: p. 140-54.
143. Guo, W., et al., *Robustness of cortical topography across fields, laminae, anesthetic states, and neurophysiological signal types.* J Neurosci, 2012. **32**(27): p. 9159-72.
144. Maruthamuthu, V., Y. Aratyn-Schaus, and M.L. Gardel, *Conserved F-actin dynamics and force transmission at cell adhesions.* Curr Opin Cell Biol, 2010. **22**(5): p. 583-8.
145. Müller, J. and M. Sixt, *Cell Migration: Making the Waves.* Curr. Biol, 2017. **27**: p. 24-25.
146. Inagaki, N. and H. Katsuno, *Actin Waves: Origin of Cell Polarization and Migration?* Trends Cell Biol, 2017. **27**: p. 515-526.
147. Discher, D.E., P. Janmey, and Y. Wang, *Tissue Cells Feel and Respond to the Stiffness of Their Substrate.* Science, 2005. **310**: p. 1139-1143.
148. Doyle, A.D., et al., *One-dimensional topography underlies three-dimensional fibrillar cell migration.* J Cell Biol, 2009. **184**(4): p. 481-90.
149. Lu, P., V.M. Weaver, and Z. Werb, *The extracellular matrix: A dynamic niche in cancer progression.* J Cell Biol, 2012. **196**: p. 395-406.
150. Petrie, R.J. and K.M. Yamada, *Fibroblasts Lead the Way: A Unified View of 3D Cell Motility.* Trends Cell Biol, 2015. **25**(11): p. 666-674.
151. Ketchum, C.M., et al., *Subcellular topography modulates actin dynamics and signaling in B-cells.* Mol Biol Cell, 2018. **29**(13): p. 1732-1742.
152. Ventre, M., et al., *Topographic cell instructive patterns to control cell adhesion, polarization and migration.* J. R. Soc. Interface, 2014. **11**: p. 20140687.
153. Wolf, K. and P. Friedl, *Extracellular matrix determinants of proteolytic and non-proteolytic cell migration.* Trends Cell Biol, 2011. **21**: p. 736-744.
154. Charras, G. and E. Sahai, *Physical influences of the extracellular environment on cell migration.* Nat. Rev. Mol. Cell Biol, 2014. **15**: p. 813-824.
155. Horn, B.K.P. and B.G. Schunck, *Determining optical flow.* Artif. Intell, 1981. **17**: p. 185-203.
156. Lucas, B.D. and T. Kanade, *An iterative image registration technique with an application to stereo vision | Proceedings of the 7th international joint conference on Artificial intelligence - Volume 2.* Proceedings of the 7th International Joint Conference on Artificial Intelligence, 1981: p. pp 674-679.
157. Blair, D. and E. Dufresne, *Crocker-Grier Particle Tracking Algorithm. The Matlab Particle Tracking Code Repository*.
158. Meyer, W.H. and T.H. Howard, *Actin polymerization and its relationship to locomotion and chemokinetic response in maturing human promyelocytic leukemia cells.* Blood, 1987. **70**: p. 363-367.
159. Lee, R.M., et al., *Collective cell migration over long time scales reveals distinct phenotypes.* Converg. Sci. Phys. Oncol, 2016. **2**: p. 025001.
160. Azatov, M., et al., *Topography on a subcellular scale modulates cellular adhesions and actin stress fiber dynamics in tumor associated fibroblasts.* Phys. Biol, 2017. **14**: p. 065003.
161. Arendt, D., et al., *The evolution of nervous system centralization.* 2008.

162. Spencer, N.J. and H. Hu, *Enteric nervous system: sensory transduction, neural circuits and gastrointestinal motility.* Nature Reviews Gastroenterology & Hepatology, 2020. **17**(6): p. 338-351.
163. JB, F., et al., *The enteric nervous system and gastrointestinal innervation: integrated local and central control.* Advances in experimental medicine and biology, 2014. **817**.
164. Rao, M. and M.D. Gershon, *The bowel and beyond: the enteric nervous system in neurological disorders.* Nature Reviews Gastroenterology & Hepatology, 2016. **13**(9): p. 517-528.
165. Camilleri, M., *Gastrointestinal motility disorders in neurologic disease.* 2021.
166. Sperber, A.D., et al., *Worldwide Prevalence and Burden of Functional Gastrointestinal Disorders, Results of Rome Foundation Global Study.* Gastroenterology, 2022. **160**(1): p. 99-114.e3.
167. EA, M., et al., *Functional GI disorders: from animal models to drug development.* Gut, 2008. **57**(3).
168. M, S., G. UC, and B. G, *Managing the Inevitable Surge of Post-COVID-19 Functional Gastrointestinal Disorders.* The American journal of gastroenterology, 2021. **116**(1).
169. JB, F. and S. MJ, *The first brain: Species comparisons and evolutionary implications for the enteric and central nervous systems.* Neurogastroenterology and motility : the official journal of the European Gastrointestinal Motility Society, 2018. **30**(2).
170. Vannier, J., et al., *Sophisticated digestive systems in early arthropods.* Nature Communications, 2014. **5**(1): p. 1-9.
171. Copenhaver, P., *How to innervate a simple gut: familiar themes and unique aspects in the formation of the insect enteric nervous system.* Developmental Dynamics : an Official Publication of the American Association of Anatomists, 2022. **236**(7): p. 1841-1864.
172. Elekes, K., E. Florey, and M.A. Cahill, *Morphology and central synaptic connections of the efferent neurons innervating the crayfish hindgut.* Cell and Tissue Research, 1988. **254**(2): p. 369-379.
173. Winlow, W. and M.S. Laverack, *The control of hindgut motility in the lobster Homarus gammarus (L.).* http://dx.doi.org/10.1080/10236247209386892, 2009.
174. DH, E., H. WJ, and K. FB, *Fifty years of a command neuron: the neurobiology of escape behavior in the crayfish.* Trends in neurosciences, 1999. **22**(4).
175. Cooper, A.S., et al., *Physiological Experimentation with the Crayfish Hindgut: A Student Laboratory Exercise.* JoVE (Journal of Visualized Experiments), 2022(47).
176. Ebara, A., *Spontaneous Activity of Crayfish Intestine.* Japanese Zoological Bulletin, 1969. **42**(4).
177. Musolf, B.E., *Serotonergic Modulation of the Crayfish Hindgut: Effects on Hindgut Contractility and Regulation of Serotonin on Hindgut*. 2007, Georgia State University.

178. Mercier, A.J., I. Orchard, and A. Schmoeckel, *Catecholaminergic neurons supplying the hindgut of the crayfish Procambarus clarkii.* https://doi.org/10.1139/z91-391, 2011.
179. Wrong, A.D., et al., *Pharmacological properties of l-glutamate receptors associated with the crayfish hindgut.* Journal of Comparative Physiology A, 2003. **189**(5): p. 371-378.
180. Mercier, A. and J. Lee, *Differential effects of neuropeptides on circular and longitudinal muscles of the crayfish hindgut.* Peptides, 2002. **23**(10).
181. Dircksen, H., et al., *Two orcokinins and the novel octapeptide orcomyotropin in the hindgut of the crayfish Orconectes limosus: identified myostimulatory neuropeptides originating together in neurones of the terminal abdominal ganglion.* Journal of Experimental Biology, 2022. **203**(18): p. 2807-2818.
182. DJ, K. and S. NJ, *What is the role of endogenous gut serotonin in the control of gastrointestinal motility?* Pharmacological research, 2019. **140**.
183. PP, B. and B. RL, *Serotonin release and uptake in the gastrointestinal tract.* Autonomic neuroscience : basic & clinical, 2010. **153**(1-2).
184. O'Mahony, S., et al., *Serotonin, tryptophan metabolism and the brain-gut-microbiome axis.* Behavioural brain research, 2015. **277**.
185. Bellono, N.W., J.R. Bayre, and D.B. Leitch, *Enterochromaffin cells are gut chemosensors that couple to sensory neural pathways.* Cell, ISSN 0092-8674, Vol. 170, Nº. 1, 2017, págs. 185-198, 2017.
186. Gershon, M. and J. Tack, *The serotonin signaling system: from basic understanding to drug development for functional GI disorders.* Gastroenterology, 2007. **132**(1).
187. Dickson, E., D. Heredia, and T. Smith, *Critical role of 5-HT1A, 5-HT3, and 5-HT7 receptor subtypes in the initiation, generation, and propagation of the murine colonic migrating motor complex.* American journal of physiology. Gastrointestinal and liver physiology, 2010. **299**(1).
188. Keating, D. and N. Spencer, *What is the role of endogenous gut serotonin in the control of gastrointestinal motility?* Pharmacological research, 2019. **140**.
189. BE, M., et al., *Serotonergic modulation of crayfish hindgut.* The Biological bulletin, 2009. **217**(1).
190. AJ, M. and L. J, *Differential effects of neuropeptides on circular and longitudinal muscles of the crayfish hindgut.* Peptides, 2002. **23**(10).
191. T, T., et al., *Dual and opposing modulatory effects of serotonin on crayfish lateral giant escape command neurons.* The Journal of neuroscience : the official journal of the Society for Neuroscience, 2001. **21**(12).
192. J, G., et al., *Image velocimetry and spectral analysis enable quantitative characterization of larval zebrafish gut motility.* Neurogastroenterology and motility : the official journal of the European Gastrointestinal Motility Society, 2018. **30**(9).
193. Lee, R., et al., *Quantifying topography-guided actin dynamics across scales using optical flow.* Molecular biology of the cell, 2020. **31**(16).
194. Simoncelli, E.P. *Design of multi-dimensional derivative filters*. in *Proceedings of 1st International Conference on Image Processing*. 2022. IEEE Computer Society.

195. Ganz, J., *Gut feelings: Studying enteric nervous system development, function, and disease in the zebrafish model system.* Developmental dynamics : an official publication of the American Association of Anatomists, 2018. **247**(2).
196. de Abreu, M., et al., *Modeling gut-brain interactions in zebrafish.* Brain research bulletin, 2019. **148**.
197. Lee, J.-G., et al., *Genetic Approaches Using Zebrafish to Study the Microbiota–Gut–Brain Axis in Neurological Disorders.* Cells, 2021. **10**(3): p. 566.
198. Accarie, A. and T. Vanuytsel, *Frontiers | Animal Models for Functional Gastrointestinal Disorders.* 2022.
199. De Luca, G.M., et al., *Re-scan confocal microscopy: scanning twice for better resolution.* Biomed Opt Express, 2013. **4**(11): p. 2644-56.
200. Edelstein, A.D., et al., *Advanced methods of microscope control using muManager software.* J Biol Methods, 2014. **1**(2).
201. Forli, A., et al., *Two-Photon Bidirectional Control and Imaging of Neuronal Excitability with High Spatial Resolution In Vivo.* Cell Rep, 2018. **22**(11): p. 3087-3098.
202. Zhang, H., E. Reichert, and A.E. Cohen, *Optical electrophysiology for probing function and pharmacology of voltage-gated ion channels.* eLife, 2016. **5**: p. e15202.
203. Chen, W., et al., *The Roles of Optogenetics and Technology in Neurobiology: A Review.* Front Aging Neurosci, 2022. **14**: p. 867863.
204. Aghayee, S., et al., *High Fidelity Spatial Light Modulator Configuration for Photo-Stimulation.* Frontiers in Physics, 2021. **9**.
205. Chong, E., et al., *Manipulating synthetic optogenetic odors reveals the coding logic of olfactory perception.* Science, 2020. **368**(6497).
206. Wang, S., et al., *All Optical Interface for Parallel, Remote, and Spatiotemporal Control of Neuronal Activity.* Nano Letters, 2007. **7**(12): p. 3859-3863.
207. Baier, H. and E.K. Scott, *Genetic and optical targeting of neural circuits and behavior--zebrafish in the spotlight.* Curr Opin Neurobiol, 2009. **19**(5): p. 553-60.
208. Leifer, A.M., et al., *Optogenetic manipulation of neural activity in freely moving Caenorhabditis elegans.* Nat. Methods, 2011. **8**(2): p. 147-152.
209. Nikolenko, V., et al., *SLM Microscopy: Scanless Two-Photon Imaging and Photostimulation with Spatial Light Modulators.* Front. Neural Circuits, 2008. **2**: p. 5.
210. Packer, A.M., et al., *Simultaneous all-optical manipulation and recording of neural circuit activity with cellular resolution in vivo.* Nat. Methods, 2015. **12**(2): p. 140-146.
211. Marshel, J.H., et al., *Cortical layer-specific critical dynamics triggering perception.* Science, 2019. **365**(6453).
212. Carrillo-Reid, L., et al., *Controlling Visually Guided Behavior by Holographic Recalling of Cortical Ensembles.* Cell, 2019. **178**(2): p. 447-457 e5.
213. Dal Maschio, M., et al., *Three-dimensional in vivo scanning microscopy with inertia-free focus control.* Opt. Lett., 2011. **36**(17): p. 3503-3505.

214. Curtis, J.E., B.A. Koss, and D.G. Grier, *Dynamic holographic optical tweezers.* Opt. Commun., 2002. **207**(1): p. 169-175.
215. Zhang, Z., Z. You, and D. Chu, *Fundamentals of phase-only liquid crystal on silicon (LCOS) devices.* Light: Science &Amp; Applications, 2014. **3**: p. e213.
216. Toyoda, H., T. Inoue, and T. Hara. *Application of liquid crystal on silicon spatial light modulator (LCOS-SLM) for manipulation and sensing*. in *2015 14th Workshop on Information Optics (WIO)*. 2015. IEEE.
217. Banerjee, A.G., et al., *Survey on indirect optical manipulation of cells, nucleic acids, and motor proteins.* Journal of Biomedical Optics, 2011. **16**(5): p. 051302.
218. Lee, S.-H. and D.G. Grier, *Robustness of holographic optical traps against phase scaling errors.* Optics Express, 2005. **13**(19): p. 7458-7465.
219. Hesseling, C., et al., *Controlling ghost traps in holographic optical tweezers.* Optics letters, 2011. **36**(18): p. 3657-3659.
220. Polin, M., et al., *Optimized holographic optical traps.* 2005. **13**(15): p. 5831-5845.
221. Paluch-Siegler, S., et al., *All-optical bidirectional neural interfacing using hybrid multiphoton holographic optogenetic stimulation.* Neurophotonics, 2015. **2**(3): p. 031208.
222. Golan, L., et al., *Design and characteristics of holographic neural photo-stimulation systems.* J. Neural Eng., 2009. **6**(6): p. 066004.
223. Matar, S., et al., *Holographic photo-stimulation for dynamic control of neuronal population activity*, in *2009 4th International IEEE/EMBS Conference on Neural Engineering*. 2009. p. 84-87.
224. Farah, N., et al., *Holographically patterned activation using photo-absorber induced neural-thermal stimulation.* J. Neural Eng., 2013. **10**(5): p. 056004.
225. Jesacher, A., S. Bernet, and M. Ritsch-Marte, *Broadband suppression of the zero diffraction order of an SLM using its extended phase modulation range.* Opt Express, 2014. **22**(14): p. 17590-9.
226. Palima, D. and V.R. Daria, *Holographic projection of arbitrary light patterns with a suppressed zero-order beam.* Applied optics, 2007. **46**(20): p. 4197-4201.
227. Boyden, E.S., et al., *Millisecond-timescale, genetically targeted optical control of neural activity.* Nat. Neurosci., 2005. **8**(9): p. 1263-1268.
228. Jiang, J., et al., *C. elegans enteric motor neurons fire synchronized action potentials underlying the defecation motor program.* Nature Communications, 2022. **13**(1): p. 2783.
229. Maity, Barun K. and S. Maiti, *Label-free imaging of neurotransmitters in live brain tissue by multi-photon ultraviolet microscopy.* Neuronal Signaling, 2018. **2**(4).
230. K, M., et al., *Functional gastrointestinal disorders and gut-brain axis: What does the future hold?* World Journal of Gastroenterology, 2019. **25**(5): p. 552-566.
231. *Electric Field-Guided Neuron Migration:A Novel Approach in Neurogenesis.* Tissue Engineering Part B: Reviews, 2011. **17**(3): p. 143-153.

232. Li, S., et al., *Effects of extracellular electric fields on electrical activities of two-compartment autaptic-neurons.* Physica A: Statistical Mechanics and its Applications, 2019. **534**: p. 122331.
233. Sun, X., et al., *Replication of biocompatible, nanotopographic surfaces.* Sci Rep, 2018. **8**(1): p. 564.
234. Ucar, H., et al., *Mechanical actions of dendritic-spine enlargement on presynaptic exocytosis.* Nature, 2021. **600**(7890): p. 686-689.
235. Cowan, N., *What are the differences between long-term, short-term, and working memory?* Prog Brain Res, 2008. **169**: p. 323-38.
236. Francis, P.T., *The interplay of neurotransmitters in Alzheimer's disease.* CNS Spectr, 2005. **10**(11 Suppl 18): p. 6-9.
237. Schulkens, J.E., et al., *The effects of selective serotonin reuptake inhibitors on memory functioning in older adults: A systematic literature review.* Journal of Psychopharmacology, 2022. **36**(5): p. 578-593.
238. Loane, C., et al., *Hippocampal network abnormalities explain amnesia after VGKCC-Ab related autoimmune limbic encephalitis.* J Neurol Neurosurg Psychiatry, 2019. **90**(9): p. 965-974.
239. Musk, E. and Neuralink, *An Integrated Brain-Machine Interface Platform With Thousands of Channels.* J Med Internet Res, 2019. **21**(10): p. e16194.
240. Mitchell, P., et al., *Assessment of Safety of a Fully Implanted Endovascular Brain-Computer Interface for Severe Paralysis in 4 Patients: The Stentrode With Thought-Controlled Digital Switch (SWITCH) Study.* JAMA Neurology, 2023.
241. Kim, K.D., et al., *Acute Implantation of a Bioresorbable Polymer Scaffold in Patients With Complete Thoracic Spinal Cord Injury: 24-Month Follow-up From the INSPIRE Study.* Neurosurgery, 2022. **90**(6): p. 668-675.
242. Barak, N., V. Kumari, and G. Sheoran, *Design and Development of an Automated Dual-Mode Microscopic System Using Electrically Tunable Lenses.* Microscopy and Microanalysis, 2022. **28**(1): p. 173-184.
243. Min, E., et al., *Label-free, multi-scale imaging of ex-vivo mouse brain using spatial light interference microscopy.* Sci Rep, 2016. **6**: p. 39667.
244. Streich, L., et al., *High-resolution structural and functional deep brain imaging using adaptive optics three-photon microscopy.* Nature Methods, 2021. **18**(10): p. 1253-1258.
245. Chen, B.-C., et al., *Lattice light-sheet microscopy: Imaging molecules to embryos at high spatiotemporal resolution.* Science, 2014. **346**(6208): p. 1257998.